

# The Exploration of Local VolumE Satellites (ELVES) Survey: A Nearly Volume-Limited Sample of Nearby Dwarf Satellite Systems

SCOTT G. CARLSTEN,<sup>1</sup> JENNY E. GREENE,<sup>1</sup> RACHAEL L. BEATON,<sup>1,2,\*</sup> SHANY DANIELI,<sup>1,\*</sup> AND JOHNNY P. GRECO<sup>3</sup>

<sup>1</sup>*Department of Astrophysical Sciences, 4 Ivy Lane, Princeton University, Princeton, NJ 08544*

<sup>2</sup>*The Observatories of the Carnegie Institution for Science, 813 Santa Barbara St., Pasadena, CA 91101*

<sup>3</sup>*Center for Cosmology and AstroParticle Physics (CCAPP), The Ohio State University, Columbus, OH 43210, USA*

(Accepted March 2, 2022)

Submitted to ApJ

## ABSTRACT

We present the final results of the Exploration of Local VolumE Satellites (ELVES) Survey, a survey of the dwarf satellites of a nearly volume-limited sample of Milky Way (MW)-like hosts in the Local Volume. Hosts are selected simply via a cut in luminosity ( $M_{K_s} < -22.1$  mag) and distance ( $D < 12$  Mpc). We have cataloged the satellites of 25 of the 31 such hosts, with another five taken from the literature. All hosts are surveyed out to at least 150 projected kpc ( $\sim R_{\text{vir}}/2$ ) with the majority surveyed to 300 kpc ( $\sim R_{\text{vir}}$ ). Satellites are detected using a consistent semi-automated algorithm specialized for low surface brightness dwarfs. As shown through extensive tests with injected galaxies, the catalogs are complete to  $M_V \sim -9$  mag and  $\mu_{0,V} \sim 26.5$  mag arcsec<sup>-2</sup>. Candidates are confirmed to be real satellites through distance measurements including redshift, tip of the red giant branch, and surface brightness fluctuations. Across all 30 surveyed hosts, there are 338 confirmed satellites with a further 105 candidates awaiting distance measurement. For the vast majority of these, we provide consistent multi-band Sérsic photometry. We show that satellite abundance correlates with host mass, with the MW being quite typical amongst comparable systems, and that satellite quenched fraction rises steeply with decreasing satellite mass, mirroring the quenched fraction for the MW and M31. The ELVES survey represents a massive increase in the statistics of surveyed systems with known completeness, and the provided catalogs are a unique dataset to explore various aspects of small-scale structure and dwarf galaxy evolution.

*Keywords:* methods: observational – techniques: photometric – galaxies: distances and redshifts – galaxies: dwarf

## 1. INTRODUCTION

The Exploration of Local VolumE Satellites (ELVES) Survey is a survey to detect and characterize low-mass, dwarf satellite galaxies around nearby, massive hosts in the Local Volume (LV;  $D < 12$  Mpc). The explicit survey goal is to fully map the “classical”-mass satellites ( $M_V < -9$  mag,  $M_\star \gtrsim 5 \times 10^5 M_\odot$ ) of all 31 LV hosts with  $M_{K_s} < -22.1$  mag throughout most of their virial volumes. Initial results of the survey have been pre-

sented in Carlsten et al. (2020a, 2021c,b). This work represents the final results of the photometric part of the survey, and we present the satellite systems of nearly all (30 out of 31) hosts in this volume-limited sample.

Broadly, the motivation of the ELVES Survey is to push our understanding of dwarf satellite galaxies beyond just the satellite system of the Milky Way (MW). The satellites of the MW have been richly characterized over the years (e.g. see Mateo 1998; Koposov et al. 2008; Simon 2019; Drlica-Wagner et al. 2020, and references therein). For decades the MW dwarfs (and to a lesser extent the satellites of M31 and other dwarfs in the Local Group) have acted as the *de-facto* benchmark for models of small-scale structure formation and dwarf

Corresponding author: Scott G. Carlsten  
scottgc@princeton.edu

\* Hubble Fellow

galaxy evolution in the  $\Lambda$ CDM paradigm (e.g. Klypin et al. 1999; Moore et al. 1999; Mayer et al. 2006; Boylan-Kolchin et al. 2011, 2012; Brooks et al. 2013; Brooks & Zolotov 2014; Garrison-Kimmel et al. 2014; Sawala et al. 2016; Wetzel et al. 2016; Bullock & Boylan-Kolchin 2017; Pawlowski 2018; Nadler et al. 2020). Yet, there is no current consensus on whether the MW and its dwarf satellites are “typical”, making these comparisons with models difficult to interpret. On the theoretical front, multiple groups have now produced large samples of high-resolution simulated MW-mass systems (Simpson et al. 2018; Garrison-Kimmel et al. 2019a; Applebaum et al. 2020; Libeskind et al. 2020; Font et al. 2020, 2021a; Engler et al. 2021) or semi-analytic models (Jiang et al. 2020), which are ready to be compared to similarly large samples of observed systems. Thus it is critical to characterize a statistical sample of satellite systems around galaxies other than the MW.

Some of the significant open questions that can be addressed with such a sample of satellite systems include: the galaxy-(sub)halo connection in low-mass ( $M_* \lesssim 10^9 M_\odot$ ) galaxies (Kim et al. 2018; Nadler et al. 2019; Munshi et al. 2021), the role of the massive host on disrupting and/or quenching star formation in the satellites (Wetzel et al. 2015; Fillingham et al. 2015; Hausammann et al. 2019; Samuel et al. 2020; Akins et al. 2021; Font et al. 2021b), and the prevalence of coherent, kinematic structures within satellite systems (Pawlowski et al. 2012; Pawlowski & Kroupa 2020; Ibata et al. 2013; Müller et al. 2018b).

In recent years, numerous groups have started work on the formidable observational task of surveying the very low-mass satellites of nearby ( $D \lesssim 50$  Mpc) massive hosts. Many groups have used deep, wide-field imaging or spectroscopic surveys to catalog candidate satellites around various hosts in the LV, including MW-mass hosts (e.g. Irwin et al. 2009; Kim et al. 2011; Sales et al. 2013; Spencer et al. 2014; Merritt et al. 2014; Karachentsev et al. 2015b; Bennet et al. 2017, 2019, 2020; Tanaka et al. 2017; Danieli et al. 2017, 2020; Smercina et al. 2018; Kondapally et al. 2018; Park et al. 2017, 2019; Byun et al. 2020; Davis et al. 2021; Garling et al. 2021; Mutlu-Pakdil et al. 2021a) and hosts of somewhat lower mass (Carlin et al. 2016, 2021; Müller & Jerjen 2020; Drlica-Wagner et al. 2021) and higher mass (Stierwalt et al. 2009; Trentham & Tully 2009; Chiboucas et al. 2009, 2013; Crnojević et al. 2014, 2016, 2019; Müller et al. 2015, 2017a, 2018a, 2019b, 2021; Smercina et al. 2017; Cohen et al. 2018) mass. Pushing to larger distances, deep surveys are starting to map the dwarf content of various galaxy groups (e.g. Greco et al. 2018b; Zaritsky et al. 2019; Habas et al. 2020; Tanoglidis et al.

2021; Prole et al. 2021). At the highest host mass end, nearby galaxy clusters are also being surveyed for dwarf satellites (Ferrarese et al. 2012, 2016, 2020; Muñoz et al. 2015; Eigenthaler et al. 2018; Venhola et al. 2018, 2021; Su et al. 2021; La Marca et al. 2021).

The process of surveying nearby satellite systems generally consists of two primary steps. The first is to detect candidate satellites. While satellites of the MW and the nearest hosts ( $D \lesssim 4$  Mpc; i.e., M31, M81, CenA, and M94) can be found via resolved stars, satellites of more distant hosts in the LV can currently only be found via integrated light<sup>1</sup>. Due to the fact that dwarfs, on average, get lower in surface brightness at lower masses (Mateo 1998; Kormendy et al. 2009; Danieli et al. 2018; Carlsten et al. 2021b), detecting very low-mass satellites in integrated light requires deep imaging and specialized detection methods (e.g. Bennet et al. 2017; Greco et al. 2018b; Danieli & van Dokkum 2019; Carlsten et al. 2020a). An important part of this first step is also quantifying the completeness of the dwarf search.

The second step is to measure distances to the dwarfs to confirm their environment (in other words, their status as satellites). While contamination from background galaxies is not much of a concern for rich groups or clusters, contamination can account for a majority of candidate satellites ( $> 80\%$ ; Carlsten et al. 2019a; Bennet et al. 2019) in sparse, MW-mass groups. As discussed in Carlsten et al. (2021c), the number of satellite systems that have been surveyed (prior to ELVES and the SAGA Survey, Mao et al. 2021, see below) with quantified completeness and distance confirmation for the candidate satellites is actually quite small ( $\sim 5$ ). We note that it is possible to treat contamination statistically, without individual satellite distance measurements, by using a background subtraction technique (e.g. Wang & White 2012; Wang et al. 2021; Nierenberg et al. 2016; Tanaka et al. 2018; Xi et al. 2018; Roberts et al. 2021; Wu et al. 2021). However, such an approach does not allow for detailed follow-up of individual dwarfs (e.g., for gas or star cluster properties) and, thus, is not the approach that ELVES takes. With that said, the statistics afforded by these works make them valuable comparisons for ELVES.

Over the years, *HST* has been employed significantly to measure precise tip of the red giant branch (TRGB) distances to LV dwarfs (e.g. Karachentsev et al. 2006, 2007, 2013, 2020; Jacobs et al. 2009; Anand et al. 2021). However, for the scale ELVES aims to address, it would

<sup>1</sup> Space-based observatories with wide fields of view, like the *Roman Space Telescope* (Spergel et al. 2015) and *Euclid* (Laureijs et al. 2011), will change this.

be infeasible to procure a statistical sample of hundreds of satellites relying solely on *HST*. Many low-mass satellites are quenched (i.e., without nebular emission lines or HI reservoirs; Karunakaran et al. 2020a; Putman et al. 2021) and are of low surface brightness (LSB) which makes acquiring a redshift extremely difficult. In earlier papers, we have shown that surface brightness fluctuations (SBF; Tonry & Schneider 1988; Jerjen et al. 2001; Rekola et al. 2005; Cantiello et al. 2018) offer an efficient way to get distances to LSB dwarfs, often from the same deep ground-based imaging used to detect them in the first place (Carlsten et al. 2019b,a; Greco et al. 2020). A combination of novel image detection algorithms and use of SBF facilitates the ELVES Survey in rapidly establishing a large sample of satellite systems.

A particularly relevant contemporary project is the Satellites Around Galactic Analogs Survey (SAGA, Geha et al. 2017; Mao et al. 2021). The SAGA Survey is an ongoing spectroscopic survey of the bright classical satellites ( $M_r < -12.3$  mag) of 100 MW-analogs in the distance range  $20 < D < 40$  Mpc. SAGA is complementary to ELVES in several important ways. First, while SAGA is not sensitive to as faint of satellites as ELVES (ELVES goes  $\sim 3$  mag fainter), it will achieve much better statistics at the bright end of the satellite luminosity function due to the larger number of hosts. Second, while SAGA selects “MW-analogs” via multiple criteria, ELVES simply selects all hosts in the LV above a certain  $K$ -band luminosity (see Section 2). Thus, SAGA will better probe what a “typical” MW-like system is, while ELVES will be more sensitive to the effect that differing host properties have on satellite systems. Finally, SAGA, being a spectroscopic survey, catalogs and characterizes satellites in a substantially different way than ELVES meaning that the projects offer an important check on each other.

As mentioned above, this paper extends the surveys presented in Carlsten et al. (2020a,b, 2021c). Since those papers, we have been able to nearly triple the number of surveyed satellite systems, essentially completing the full volume-limited sample. These new dwarf findings have been used in Carlsten et al. (2021b) and Carlsten et al. (2021a) to explore different aspects of dwarf galaxy evolution but have not been fully described until the current paper. This paper is structured as follows: in Section 2 we describe the host selection process and final host list, in Section 3 we outline the different sources of data used, in Section 4 we describe the detection of candidate satellites, in Section 5 we detail how we confirm the distance of the satellites, in Section 6 we describe how we characterize the satellites, in Section 7 we give some overview of the properties of the satellite systems,

including satellite abundance, spatial distribution, and the fraction of star-forming satellites, and, finally, in Section 8 we give an overview of the key results of the ELVES Survey to this point.

## 2. HOST SELECTION

The primary goal of the ELVES Survey is to obtain a volume limited sample of well-surveyed satellite systems around massive, roughly MW-like host galaxies. In this section, we describe the selection of the host sample and give some details on the host properties.

To make the initial host list, we use both the group catalog of Kourkchi & Tully (2017) (hereafter KT17) and the Updated Nearby Galaxy Catalog (UNGC) of Karachentsev et al. (2004, 2013) (hereafter K13). The group catalog of KT17 is based on the Cosmic-Flows (Tully et al. 2016) distance database. For massive galaxies, the catalog relies heavily on the 2MASS Redshift Survey (Huchra et al. 2012), which is complete down to  $K_s = 11.75$  mag. At the edge of the LV (12 Mpc), this corresponds to a luminosity of  $M_{K_s} = -18.6$  mag and thus will include all potential massive host galaxies. The catalog of K13 includes many more up-to-date (e.g., very recent TRGB distances) than KT17 but is missing several massive hosts that are known to be within the LV. Using these two catalogs, almost all of the potential hosts have direct (i.e. not redshift-based) distance measurements with the majority being from TRGB observations.

The cuts that we make on the catalogs are as follows:

$$\begin{aligned} \text{Distance} &: D < 12 \text{ Mpc} \\ \text{Host Luminosity} &: M_{K_s} < -22.1 \text{ mag} \\ \text{Galactic Latitude} &: |b| > 17.4^\circ \end{aligned} \quad (1)$$

In making the host list, we merge the two catalogs but always use the  $K_s$  magnitude reported by KT17. To these catalogs, we add the host NGC 4565 which has a TRGB distance from Radburn-Smith et al. (2011) of within 12 Mpc but whose distance in KT17 is greater than 12 Mpc<sup>2</sup>.

The chosen  $K_s$  luminosity cut corresponds to a stellar mass of roughly  $M_\star \approx 10^{10} M_\odot$ , assuming  $M_\star/L_{K_s} = 0.6$  (McGaugh & Schombert 2014). For each host, we search NED and SIMBAD for more up-to-date distances

<sup>2</sup> With the larger distance, KT17 group NGC 4565 with NGC 4494, which has an SBF distance of 16.9 Mpc. With the TRGB distance of 11.9 Mpc we take for NGC 4565, it seems likely that these two galaxies are not physically associated. Therefore, for NGC 4565, we do not take the group properties calculated by KT17 because they will include NGC 4494. Instead, we calculate them ourselves using the members of NGC 4565’s group cataloged in ELVES.

(particularly looking for precise distances, like those from TRGB, SNe Ia, or Cepheid observations). Where appropriate, we update the  $K_s$  luminosity from [KT17](#) using the newer distance. The cut on Galactic latitude,  $b$ , is chosen to be as restrictive as possible to eliminate highly extinguished hosts while still including NGC 891 and Cen A, both major focuses of recent dwarf satellite research (e.g. [Trentham & Tully 2009](#); [Müller et al. 2019a](#); [Crnojević et al. 2019](#); [Müller et al. 2021](#)).

With these cuts, we often select multiple members within the same galaxy group. In these cases, we choose the member with the greatest  $K_s$  luminosity as the ‘host’ and remove the the fainter objects from consideration as a ‘host’. The specific galaxies that obey our other cuts but are likely affiliated with a more massive host are given in [Appendix A](#).

The host list is given in [Table 1](#). There are 31 primary, massive hosts that pass our selection criteria. 30 of these are surveyed for satellites in this work or by previous work in the literature, leaving only one host (NGC 3621) unanalyzed. We list names, distances, redshifts<sup>3</sup>, and various photometry for each of the hosts. The stellar masses generally come from multi-wavelength photometry (including IR band-passes) and have been corrected for the updated distances that we use. In [Table 1](#), the  $r_{\text{cover}}$  column lists the approximate radial coverage (in projected kpc from the host) of the survey imaging used to find candidate satellites.

The on-sky locations of these hosts are shown in [Figure 1](#). In [Figure 2](#), we show various properties of the host sample. The hosts are fairly evenly distributed between  $10^{10}$  and  $10^{11}M_{\odot}$  in stellar mass. The right panel shows the group  $K_s$  luminosity (the sum of the luminosity for all group members) reported in the group catalog of [Kourkchi & Tully \(2017\)](#) versus the luminosity of just the primary host. In most cases, these values are quite close, indicating the host completely dominates the luminosity of the group. For a few cases, the group luminosity is significantly larger than that of the primary host. These include the M81/M82 group, the Leo I group, and the Leo Triplet (labelled in the Figure), each of which has several massive galaxies. In previous papers on this survey, we have referred to these hosts as ‘small-groups’ to distinguish that they are notably higher mass than bona fide MW-analogs.

### 3. OBSERVATIONAL DATA

The full ELVES survey is an extension of our earlier survey presented in [Carlsten et al. \(2020a, 2021c\)](#).

That work presented a set of LV hosts surveyed with archival CFHT/MegaCam data<sup>4</sup>. The ELVES sample is considerably expanded by using the extremely wide-field DECaLS imaging data sets ([Dey et al. 2019](#); [Zou et al. 2017, 2018](#)).

As stated above, the process of cataloging nearby satellite systems is two-fold. First, candidate satellites need to be detected either visually or with an automated algorithm. Second, the candidate satellites need to have their distances measured to confirm that they are actually physically associated with a purported host. In [Carlsten et al. \(2020a, 2021c\)](#), the CFHT/MegaCam data was of high-enough quality to do both steps, with the second step being accomplished via measurements of surface brightness fluctuations (SBF). However, the DECaLS data is almost always too shallow and with too poor of seeing to do the distance measurements, and thus we generally only use it for the object detection. The distance measurements come from SBF using various follow-up data, including archival Hyper Suprime-Cam (HSC) and new Gemini and Magellan imaging.

[Table 1](#) lists the data sources used for each host, including for candidate detection and distance confirmation. The table also lists data sources for the satellite photometry used throughout the paper, which is almost always the same as the candidate detection data, except for where we use a literature reference for the satellite detection. Overall, we use literature sources for the satellite lists for 5 hosts (MW, M31, CenA, NGC 5236, and M81) and do our own object detection for 25 hosts. 17 of these use DECaLS imaging, 6 (NGC 1023, NGC 4258, NGC 4565, NGC 4631, NGC 5194, and M104) use the CFHT/MegaCam search of [Carlsten et al. \(2020a\)](#)<sup>5</sup>, one (NGC 891) uses separate CFHT/MegaCam data, and one (NGC 6744) uses (non-DECaLS) DECam data.

Regardless of the source for the imaging data, we always use two bands for candidate detection: either  $g/r$  or  $g/i$ . The one exception is NGC 891, where for about half of the surveyed area, only  $r$ -band data are available. Deeper follow-up data for distance confirmation are often only a single band (either  $r$  or  $i$ ) since those are the ideal SBF bands, and a color measurement already exists from the candidate detection data.

<sup>4</sup> Specifically 10 hosts were included, but only 8 made it into the ELVES host sample, 2 of which are redone here with DECaLS data due to the limited radial coverage of the CFHT/MegaCam data.

<sup>5</sup> Two of these (NGC 4631 and NGC 4258) additionally use DECaLS imaging to extend the radial coverage slightly, as explained more below.

<sup>3</sup> The velocity for NGC 3627 is actually the average of the three centrals in the Leo Triplet: NGC 3627, NGC 3623, and NGC 3628.

**Table 1.** ELVES Host List

Name	Dist	$v_{\text{rec}}$	$M_{K_s}$	$M_{K_s}^{\text{group}}$	$M_V$	$B - V$	$\log(M_*/M_\odot)$	$r_{\text{cover}}$	Data Source	References
	Mpc	km/s	mag	mag	mag	mag		kpc		
M31	0.78	-300	-24.81	-24.89	-21.19	0.87	11.01	300	M12	CF, RC3, Sick15
NGC253	3.56	259	-23.95	-23.96	-20.7	0.94	10.77	300	D- -D	CF, Cook14a, Cook14b
NGC628	9.77	656	-22.79	-22.81	-20.68	0.48	10.45	300	D-G-D	CF, Cook14a, Cook14b
NGC891	9.12	528	-23.83	-23.83	-20.05	0.82	10.84	200	C-C-C	CF, GALEX, $M_{K_s}$
NGC1023	10.4	638	-23.78	-23.98	-20.91	0.95	10.6	200	C-C-C	NED, GALEX, $M_{K_s}$
NGC1291	9.08	838	-23.94	-23.97	-21.01	1.0	10.78	300	D-D,M-D	CF, Cook14a, Ler19
NGC1808	9.29	1002	-23.12	-23.78	-19.98	0.79	10.01	300	D-D,G,H,M-D	CF, RC3, Ler19
NGC2683	9.4	409	-23.49	-23.5	-20.17	0.86	10.5	300	D-H-D	K15, Cook14a, Ler19
NGC2903	9.0	556	-23.68	-23.69	-20.78	0.65	10.67	300	D-G,C-D	K13&T19, Cook14a, Cook14b
M81	3.61	-42	-23.89	-25.27	-21.07	0.88	10.66	300	C13-C13-C13,D	CF, GALEX, Ler19
NGC3115	10.2	666	-24.12	-24.14	-21.27	0.93	10.76	300	D-G-D	Pea15, RC3, Ler19
NGC3344	9.82	585	-22.27	-22.27	-20.19	0.65	10.27	300	D-H-D	CF, Cook14a, Ler19
NGC3379	10.7	876	-23.8	-25.37	-20.46	0.78	10.63	370	D-H-D	M18, HT11, Ler19
NGC3521	11.2	798	-24.4	-24.41	-21.39	0.76	10.83	330	D-H-D	This Work, GALEX, Ler19
NGC3556	9.55	698	-22.76	-22.76	-19.96	0.69	9.94	300	D- -D	CF, RC3, Ler19
NGC3621	6.7	731	-22.37	-22.37	-19.79	0.55	9.9	0	- -	CF, RC3, Ler19
NGC3627	10.5	789	-24.17	-25.33	-21.28	0.7	10.66	300	D-C,H-D	Lee13, GALEX, Ler19
NGC4258	7.2	462	-23.7	-23.94	-20.92	0.71	10.62	150	C,D-C,H-C,D	H13, Cook14a, Ler19
NGC4517	8.34	1136	-22.13	-22.16	-19.27	0.67	9.93	300	D-H-D	K14, RC3, $M_{K_s}$
NGC4565	11.9	1261	-24.26	-24.27	-20.84	0.82	10.88	150	C-C-C	RS11, RC3, Ler19
M104	9.55	1092	-24.91	-25.01	-22.04	0.94	11.09	150	C-C-C	McQ16b, RC3, Ler19
NGC4631	7.4	606	-22.73	-22.9	-20.21	0.55	10.05	200	C,D-C,G-C,D	RS11, RC3, Ler19
NGC4736	4.2	287	-22.96	-23.1	-19.93	0.74	10.29	300	D-S18-D	RS11, RC3, Ler19
NGC4826	5.3	402	-23.24	-23.24	-20.21	0.8	10.36	300	D-H,C-D	CF, RC3, Ler19
NGC5055	8.87	503	-24.02	-24.04	-21.2	0.71	10.72	300	D-H-D	McQ17, RC3, Ler19
CENA	3.66	548	-23.87	-24.41	-21.29	0.89	10.92	200	M/C19-M/C19-Dc,M17	CF, RC3, Ler19
NGC5194	8.58	465	-24.08	-24.51	-21.4	0.56	10.73	150	C-C-C	McQ16a, GALEX, Ler19
NGC5236	4.7	520	-23.64	-23.67	-21.02	0.53	10.37	300	M15-M18,D-D	CF, Cook14a, Ler19
NGC5457	6.5	243	-23.12	-23.16	-21.22	0.44	10.33	300	D-B19,C,H-C,D	Beat19, RC3, Ler19
NGC6744	8.95	839	-23.58	-24.0	-21.64	0.86	10.64	200	Dc-Dc-Dc	CF, RC3/HyperLeda, Ler19
MW	0	0	-24.0	-24.13	-20.74	0.67	10.78	300	M12	Lic15, BG16

NOTE—Volume limited sample of massive hosts, selected with  $M_{K_s} < -22.1$  mag,  $|b| > 17.4^\circ$ , and  $D < 12$  Mpc.  $M_{K_s}^{\text{group}}$  denotes the total luminosity for the group, as determined by Kourkchi & Tully (2017).  $r_{\text{cover}}$  denotes the projected radial extent of the satellite survey. The data source column lists the data sets used for satellite detection, confirmation (i.e. measuring candidate satellite distances), and photometry. The letters stand for: D-DECaLS, Dc-DECam (but not from DECaLS), C-CFHT/MegaCam, H-Subaru/HSC, G-Gemini/GMOS, M-Magellan/IMACS. The literature references used in this column are: S18-Smercina et al. (2018), B19-Bennet et al. (2019), M12-McConnachie (2012), C13-Chiboucas et al. (2013), M15-Müller et al. (2015), M17-Müller et al. (2017a), M18-Müller et al. (2018c), M19-Müller et al. (2019b), C19-Crnojević et al. (2019). The reference column lists references for the host distance,  $BV$  photometry, and stellar mass, respectively. The sources are: Beat19-Beaton et al. (2019), CF-Kourkchi & Tully (2017) and Tully et al. (2016), RS11-Radburn-Smith et al. (2011), H13-Humphreys et al. (2013), K13-Karachentsev et al. (2013), K14-Karachentsev et al. (2014), K15-Karachentsev et al. (2015a), T19-Tully et al. (2019), Pea15-Peacock et al. (2015), McQ16a-McQuinn et al. (2016a), McQ16b-McQuinn et al. (2016b), McQ17-McQuinn et al. (2017), Lee13-Lee & Jang (2013), M18-Müller et al. (2018a), Ler19-Leroy et al. (2019), Cook14a-Cook et al. (2014a), Cook14b-Cook et al. (2014b), GALEX-Gil de Paz et al. (2007), RC3-de Vaucouleurs et al. (1991), HT11-Hernández-Toledo et al. (2011), Sick15-Sick et al. (2015), BG16-Bland-Hawthorn & Gerhard (2016), Lic15-Licquia et al. (2015). A stellar mass reference of  $M_{K_s}$  denotes that the stellar mass came from the  $K_s$  luminosity and a  $M_*/L_{K_s} = 0.6$ , assuming  $M_{K_s}^\odot = 3.27$  mag in the Vega system (Willmer 2018).

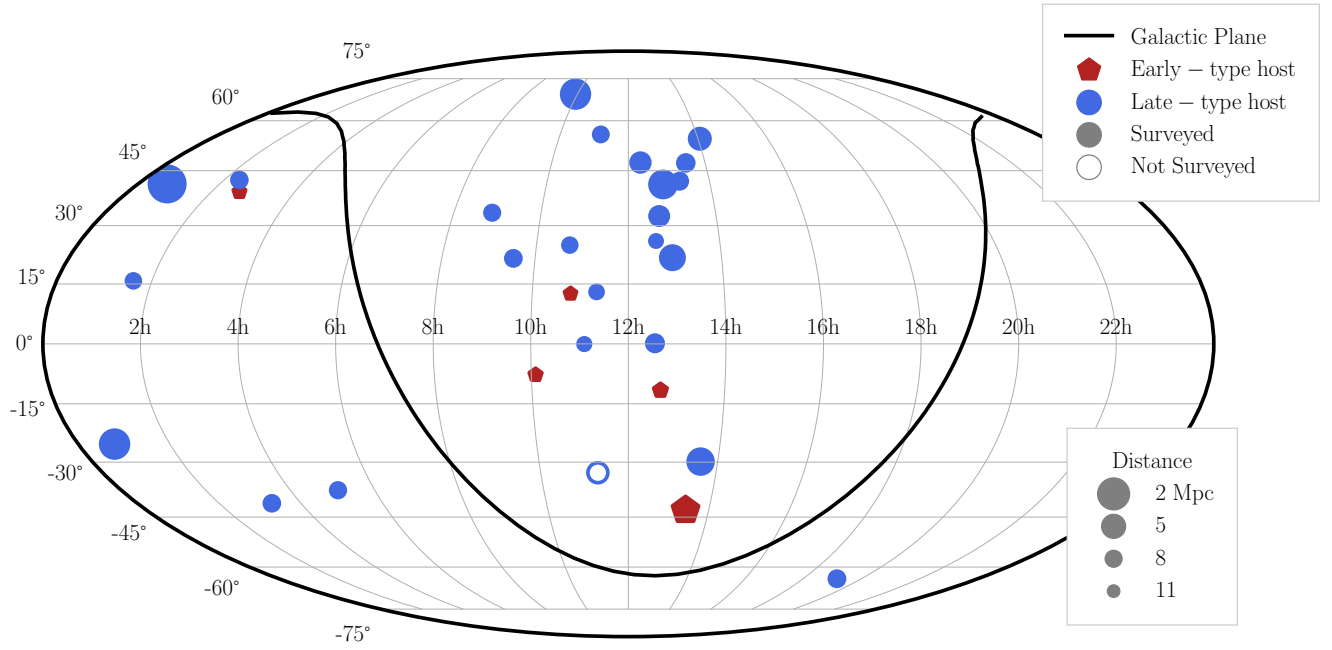


**Figure 1.** Position on the sky of the ELVES host sample. Hosts are colored by their morphology: late-type spirals vs. early-type ellipticals and lenticulars. Point size indicates the host distance. The unfilled point labelled ‘Not Surveyed’ indicates a host where we have no survey coverage (NGC 3621). All other hosts have candidate satellite lists.

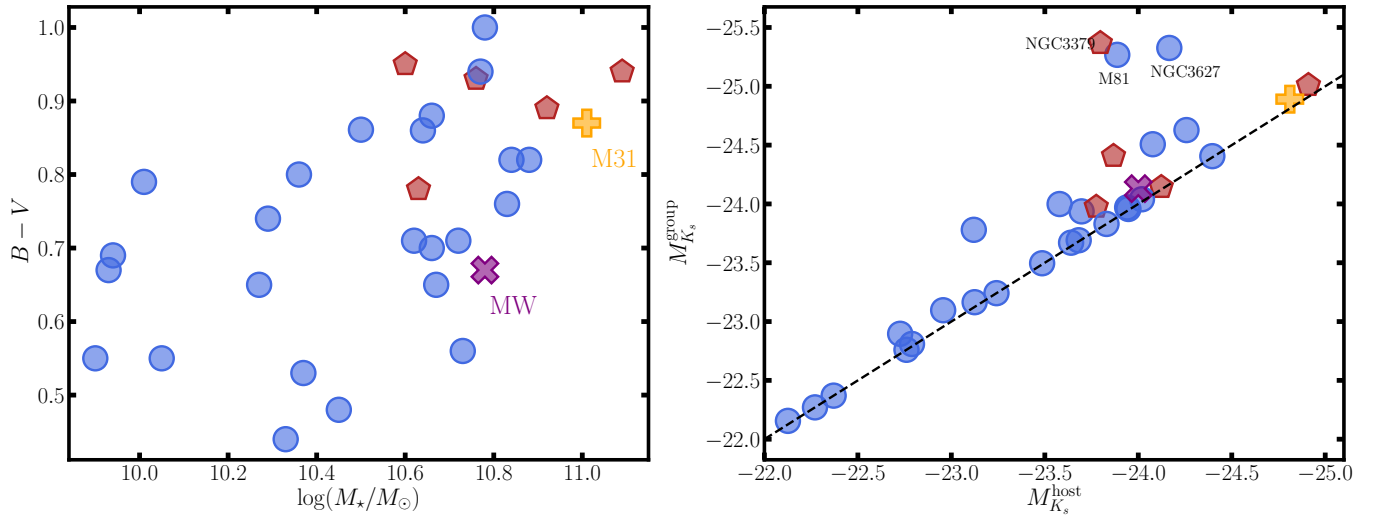


**Figure 2.** Properties of the full ELVES host sample. *Left:* The host color vs. stellar mass. Points are the same as in Figure 1. *Right:* Host  $K_s$  luminosity vs. group  $K_s$  luminosity. The three hosts with the largest difference between the two luminosities are labelled. NGC 3379 and NGC 3627 are the primaries of the Leo I and Leo Triplet groups, respectively.

The reduced DECaLS imaging data are taken directly from the web server<sup>6</sup> where  $g$  and  $r$  band data are available for download. We use DECaLS DR8 for the candidate detection but have redone the satellite photometry using DR9 as the DR9 reduction includes a more optimized sky-subtraction for LSB galaxies<sup>7</sup>. Overall, we find minimal difference between DR8 and DR9.

CFHT/MegaCam data are downloaded raw from the CFHT archive server<sup>8</sup> and are reduced in the fashion described in Carlsten et al. (2019b) and Carlsten et al. (2020a). DECam data that are not part of DECaLS (NGC 6744 is the only host that uses this) are downloaded raw from the NOIRLab archive<sup>9</sup> and reduced in a very similar way to the CFHT data. Generally, SDSS (Abolfathi et al. 2018) or Pan-STARRS (Chambers et al. 2016; Flewelling et al. 2016) are used for the photometric calibration. For the few southern hemisphere hosts outside those footprints, we use *Gaia* (Gaia Collaboration et al. 2018) or APASS (Henden & Munari 2014) for the photometric calibration.

Gemini/GMOS data are reduced using the DRAGONS software package<sup>10</sup>. Gemini/GMOS data from programs FT-2020A-060, US-2020B-037, and US-2021B-0018 (PI: S. Carlsten) are used. Magellan/IMACS data are reduced using a custom pipeline that does all the main steps in a similar way to the MegaCam and DECam pipelines. Finally, the HSC data are downloaded from the Subaru archive<sup>11</sup> and reduced using the pipeline written by the HSC team (Bosch et al. 2018). All HSC data are archival and include (but are not limited to) data from the HSC-SSP survey (Aihara et al. 2018, 2019).

All of these telescopes and camera systems use Sloan-like filters. However, there will be some slight differences between the different filter sets. Following Carlsten et al. (2021b), we do not make any attempt to bring them all onto the same filter system. That work (Figure 16 in that paper) showed that the differences between the filters is expected to be  $\lesssim 0.1$  mag based on synthetic photometry from stellar evolution models (Choi et al. 2016). One instance where systematic offsets of this magnitude might matter is integrated color. However, the effect of this systematic uncertainty in inferring stellar mass (the primary use of color) is generally less than the statisti-

cal uncertainty coming from photon noise and/or sky subtraction issues and thus we do not account for it.

The actual areal coverage of each host is shown in Appendix B. For the DECaLS hosts, we almost always are able to extend fully to 300 kpc, an approximate value for the virial radius of halos of the typical mass expected for most ELVES hosts ( $M_{\text{halo}} \sim 10^{12} M_{\odot}$ ). We note that the halo masses of the most massive hosts in the ELVES sample (e.g. M104, NGC 3627, and NGC 3379) are likely closer to  $\sim 10^{13}$  (Karachentsev & Kudrya 2014; Kourkchi & Tully 2017) and will have much larger virial radii. On the other hand, the least massive ELVES hosts (e.g. NGC 3344 and NGC 4517) will have smaller virial radii. The hosts from the non-DECaLS data sources (CFHT/MegaCam or DECam) all have less coverage. For a couple of these (NGC 4631 and NGC 4258), we extend the CFHT/MegaCam data with some DECaLS data and additional SBF follow-up, with the specific footprints shown in Appendix B. The approximate radial extent of the search footprints for each host are listed as  $r_{\text{cover}}$  in Table 1.

#### 4. CANDIDATE SATELLITE DETECTION

For the 25 hosts where we conduct our own candidate satellite detection, we apply the semi-automated detection algorithm optimized for LSB dwarf galaxies detailed in Carlsten et al. (2020a). This algorithm draws heavily on the LSB galaxy detection pipelines of Bennet et al. (2017) and Greco et al. (2018b).

We use a custom search algorithm as opposed to simply using common object detection algorithms (e.g. SExtractor, Bertin & Arnouts 1996), because those algorithms are not optimized for large, diffuse, LSB dwarf galaxies. Such sources are likely to get “shredded” (i.e. over-deblended). More advanced algorithms (e.g. Akhlaghi & Ichikawa 2015; Lang et al. 2016; Robotham et al. 2018; Melchior et al. 2018; Haigh et al. 2021) are being developed that demonstrate promise for LSB dwarf surveys (Venholo et al. 2021). While our search algorithm is more complicated than simply using SExtractor, it still does make use of SExtractor in multiple ‘hot-and-cold’ runs (i.e. runs with high and low thresholds, see below) intermixed with aggressive masking.

Like many other object detection algorithms, the one used here explicitly separates source detection from source extraction. In this section, we detail the first step which is simply to find the dwarf galaxies. A later section (§6) describes how we measure the photometric properties of the candidate satellites.

##### 4.1. Overview of Detection Algorithm

<sup>6</sup> <https://www.legacysurvey.org/>.

<sup>7</sup> See <https://www.legacysurvey.org/dr9/sky/>.

<sup>8</sup> <http://www.cadc-ccda.hia-ihp.nrc-cnrc.gc.ca/>

<sup>9</sup> <https://astroarchive.noirlab.edu/>

<sup>10</sup> <https://dragons.readthedocs.io/en/v3.0.0/>

<sup>11</sup> <https://smoka.nao.ac.jp/fssearch>

The search algorithm is detailed in Carlsten et al. (2020a) and is applied essentially unchanged to the DECaLS data, but we provide a brief overview of the important steps in this section. The main steps of the process are:

1. Create bright star masks from *Gaia* star catalogs for stars brighter than 20<sup>th</sup> magnitude. Custom shaped masks that cover the scattered light halos and saturation spikes of bright stars are applied to all of the survey fields.
2. Initial detection step with a large size and moderate significance threshold to find large, relatively high surface brightness candidate satellites. In particular, **SExtractor** is run with a  $5\sigma$  threshold and  $\sim 2000$  pixel minimum area (corresponding to a radius of  $\sim 7''$  for a circular source). To remove some massive background galaxies, an effective surface brightness cut of  $\langle\mu\rangle_{r_e} \gtrsim 22$  mag arcsec<sup>-2</sup> (calculated from **SExtractor** fluxes and sizes) is applied to the detections. Note that this is not the only stage where relatively massive satellites can be detected as their diffuse/LSB outskirts will also be detected in the LSB detection step below (and dwarfs universally have diffuse outskirts, see Kado-Fong et al. 2020).
3. Mask bright sources and their associated diffuse emission as in Greco et al. (2018b). Sources are detected with both a high,  $15\sigma$ , and low,  $\sim 1\sigma$ , detection threshold. The LSB detections are associated with a high surface brightness (HSB) detection if they overlap more than a certain fraction (5%) of their pixels with the HSB detection. The detected LSB pixels that do get associated with an HSB detection get masked. These represent, for example, the extended envelopes of background galaxies, intracluster light from galaxy clusters, and/or scattered light around stars not bright enough to be covered by the *Gaia* star mask. After this step, there is a another simple masking of all sources over  $\sim 4\sigma$  above the background.
4. Filter the image to emphasize diffuse, LSB emission. The masked image is convolved with a Gaussian with FWHM  $\sim 2\times$  the field's PSF size.
5. Second detection step with a low threshold to find faint candidate satellites. Sources in the masked and filtered image are detected with a significance threshold of  $\sim 2\sigma$  and size greater than  $\sim 800$  pixels (corresponding to a radius of  $\sim 4''$  for a circular source).
6. Visual inspection to remove artifacts and other false positives. The vast majority ( $> 95\%$ ) of the things removed in this step are clear artifacts such as saturation spikes or emission from bright stars or the outskirts of massive elliptical galaxies that leaked through the masks. Additionally, detected galaxies that are clear background contaminants are removed. For instance, small ( $r_e \lesssim 5''$ ) galaxies that have well-defined spiral arms or a bulge+disk morphology are clearly not in the Local Volume. Low-mass dwarfs will necessarily be fairly featureless and diffuse. Carlsten et al. (2020a) gives more details on this step and examples of visually rejected galaxies. Often during this step, particularly ambiguous detections are queried in Simbad and any galaxies with known redshifts more than 275<sup>12</sup> km/s greater than the host are background objects and not further considered.

The first five steps are done independently in the  $g$  and  $r$  (or  $i$ ) bands and then the two detection catalogs are merged before the visual inspection step. Objects need to be detected in both bands to pass to the visual inspection step.

Many of the algorithm's parameters needed to be slightly tweaked for each field to account for the differing depths of the different datasets and host distances. Each parameter preceded by a  $\sim$  in the description above was often tuned for each host. Hosts with shallower imaging, for instance, needed a larger smoothing kernel (i.e. more blurring), and more nearby hosts had larger size thresholds for detected objects. The parameters were tuned in an initial step where a subset of the survey coverage for each host was visually searched for candidate satellites against which the algorithm was tested. The specific parameters used for each host are not particularly important to the results as the search algorithm's completeness for each host is quantified using those same parameters. Thus, all affects they have on the search completeness are accounted for.

Figure 3 demonstrates the main steps through an example part of the field around NGC 3379, the main host of the rich Leo I group. The top panel shows the raw DECaLS image ( $g + r$  color composite). The middle panel shows the image with bright stars and background galaxies masked and filtering applied. The masking in Step 3 above is clearly quite aggressive, but we show in the next section on completeness that it is not overly aggressive because it does not completely mask candidates.

<sup>12</sup> We discuss this velocity criterion later in §5.

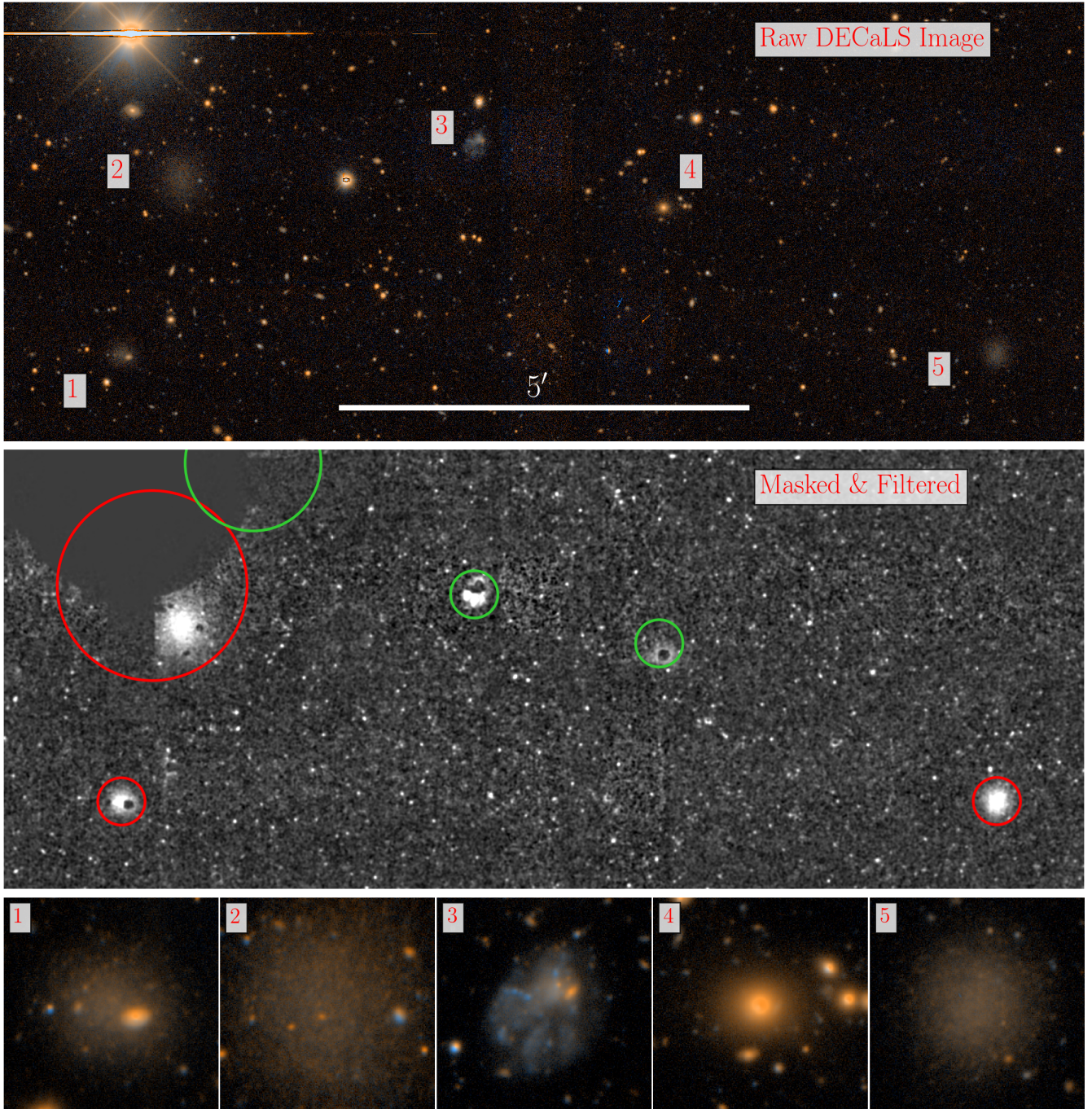


**Figure 3.** Demonstration of the detection algorithm on a surveyed area near NGC 3379. Top panel shows the raw DECaLS detection images ( $g+r$  color composite). The middle panel shows the detection image after it has been masked for bright stars and galaxies and has been filtered to bring out LSB emission. Detections from the pipeline are shown as circles. The detections that pass visual inspection are in red while those that do not are shown in green. The rejected detection in the top left is from scattered light from the bright star leaking through the mask while the other two detections are clear background galaxies (see text for more details). The five labeled detections are shown in the bottom row in deep HSC images. These images are not used in the detection process but are used to confirm the candidate satellites via SBF distance measurements. The images on the bottom row are  $40''$  (2 kpc at the distance of NGC 3379) to a side.

The detections from Step 5 are shown as the superimposed circles. Those that pass visual inspection are in red while those that are rejected are in green. The five detections that are labeled in the top image are shown in close-up in the bottom row using extremely deep ( $> 2$  hour integration) HSC images<sup>13</sup>. The sixth rejected detection is simply emission that leaked around the star mask and is not shown in close-up. Detections 1, 2, and 5 are high-quality candidate satellites. In fact, these candidates are all confirmed satellites via SBF distance measurements. The two rejected detections (3 and 4) are background galaxies. Object 3 has a complicated morphology and small size ( $r_e \sim 5''$ ), indicating it is not in the Local Volume. In this case, its HI redshift from ALFALFA (Haynes et al. 2018) of several thousand km/s greater than that of NGC 3379 confirms this, although not all visually rejected galaxies have redshifts. Object 4 is a massive background elliptical whose outskirts leaked through the masking. While this visual inspection step might appear to introduce ambiguity, visual selection of dwarfs in the Local Volume is a powerful tool due to their proximity (e.g. Karachentseva 1968; Karachentsev et al. 2007) and many contemporary searches are primarily visual (e.g. Byun et al. 2020; Habas et al. 2020).

The median false positive rate as determined by the visual inspection step is  $\sim 30$  rejected detections (e.g. artifacts, halos around bright stars, or background galaxies) for each candidate satellite<sup>14</sup>. As stated above, this is mostly a result of insufficient masking of bright stars or bright background galaxies that allows too much emission to pass through. This step did require a fairly significant amount of human involvement, meaning that this algorithm is not scalable for the extremely wide-field surveys of the Roman Space Telescope or Vera Rubin Observatory. For the relatively small areas surveyed in ELVES ( $\sim 400$  square degrees total), removing these contaminants by visual inspection was tractable.

#### 4.2. Completeness of Surveys

In order to facilitate comparison to other satellite dwarf searches and theoretical models, it is critical to quantify the completeness of the survey. We do this by injecting artificial galaxies into the survey images and

<sup>13</sup> The HSC images are just being shown for clarity, the visual inspection step is done just on the detection images (DECaLS in this case).

<sup>14</sup> Note that this ‘false positive rate’ describes the ratio of the number of total detections to those that pass as candidate satellites. There is another ‘false positive rate’ to describe the ratio of total number of candidate satellite to those that actually get confirmed as physical satellites via a distance measurement which will be discussed in §5.

quantifying the fraction of injected galaxies recovered as a function of input luminosity and size. The fact that our search process is semi-automated (as opposed to purely visual) greatly facilitates this process. We do not apply any visual inspection step to the artificial galaxies and assume that any injected galaxy detected by the search algorithm would pass the visual inspection. In this section, we describe the artificial galaxy injection and show the overall average completeness of the survey.

The process for injecting artificial galaxies is detailed in Carlsten et al. (2020a). The DECaLS and non-DECaLS hosts are treated a little differently, primarily in that the non-DECaLS hosts have their artificial galaxies injected at the chip level before sky subtraction and coaddition. On the other hand, the DECaLS hosts have their artificial galaxies injected directly in the coadds due to the significantly larger volume of imaging data, both in number of hosts and area covered per host. In either case, exponential profiles (i.e.  $n = 1$  Sérsic profiles) are injected at various  $r$  or  $i$  luminosities and central surface brightness levels, with colors in the range  $g - r \in [0.3, 0.6]$  or  $g - i \in [0.4, 0.8]$  depending on which filters are used. The data are then run through the detection pipeline, and the fraction of galaxies in each luminosity and surface brightness bin that are recovered is recorded. Simulated dwarfs that fall on top of areas lost to the star-masking are not treated differently, thus, we do not expect the recovery fraction to ever be 100%. The area lost to star-masking is generally around  $\sim 5\%$ .

As shown in Carlsten et al. (2021b), the input galaxy parameters roughly resemble the Sérsic indices and colors of the real satellites, both quenched and star-forming. However, true dwarf galaxies generally have slightly lower average Sérsic index of  $n \sim 0.7$ , a result also seen in other surveys (e.g. Eigenthaler et al. 2018; Ferrarese et al. 2020). At fixed luminosity and central surface brightness, a higher Sérsic index dwarf will be more difficult to find since more of the emission will be at a very low surface brightness level in its outskirts, and more likely to be buried in the sky noise. Thus, we expect these completeness estimates to be slightly conservative.

Figure 4 shows the results of the injection simulations. The left panel shows the average recovery fraction across all 25 hosts. In doing the average, the hosts are weighted by the number of confirmed and possible satellites (see §5 below). The center and right panels show the average recovery fraction of the DECaLS hosts separately from the other hosts (primarily CFHT/MegaCam hosts).

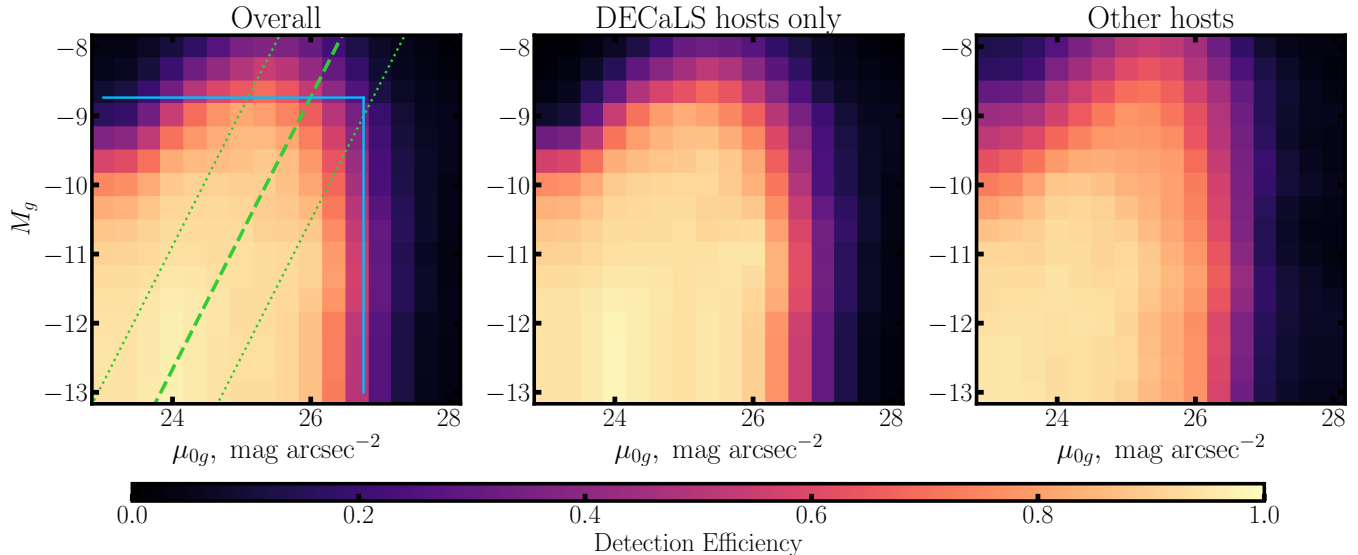


**Figure 4.** Average completeness of the dwarf searches as quantified by image simulations with injected artificial galaxies. Left panel shows the average of all hosts, while center and right panels split the hosts by the source of the imaging data. The blue region in the left panel demarcates the completeness quoted in prior ELVES papers ( $M_V < -9$  mag and  $\mu_{0,V} < 26.5$  mag arcsec $^{-2}$ ). The green dashed line shows the mass-size relation of Carlsten et al. (2021b) converted into this plane, and the green dotted lines show the  $1\sigma$  intrinsic scatter measured in the mass-size relation.

Results for individual hosts are shown in Appendix C. The recovery fractions are generally similar across the different hosts and data sources. We note that the BASS part of DECaLS (which 4 DECaLS hosts use) and the CFHT/Megacam data used for NGC 891 are significantly shallower than the rest of the hosts with the surface brightness completeness being  $\sim 0.5$  mag lower. However, this is a relatively small number of hosts, and we do not further distinguish these from the others.

The blue region in the left panel of Figure 4 shows the completeness limits quoted in previous ELVES papers:  $M_V < -9$  mag and  $\mu_{0,V} < 26.5$  mag arcsec $^{-2}$ , assuming  $g - V \approx 0.25$  mag. The green dashed line shows the mass-size relation of Carlsten et al. (2021b) converted into this plane assuming  $M_*/L_g = 1.24$  which comes from the color- $M/L$  relation of Into & Portinari (2013) and the average color of  $g - i = 0.74$ . An  $n = 1$  Sérsic profile is assumed in determining the central surface brightness from luminosity and effective radius.

Overall, the recovery fraction is  $\sim 90 - 95\%$  at bright magnitudes and surface brightness, reflecting the area lost from the search to star masks. There is a clear drop-off in completeness between  $\mu_{0,g} \sim 26 - 27$  mag arcsec $^{-2}$ . The  $\mu_{0,V} < 26.5$  mag arcsec $^{-2}$  we have quoted in the past is roughly the 50% completeness limit.

In addition to the artificial galaxy injection tests, our completeness is proven through comparison with previous satellite searches in the literature for several of the ELVES hosts. In Appendix D, we go through the hosts in more detail, and provide detailed comparison with

previous searches from the literature for hosts that have them. The comparisons are quite favorable for ELVES with no candidate satellites missed above the asserted completeness level across the 8 ELVES hosts that have been significantly surveyed in the past.

For the five hosts that we do not perform our own object detection (MW, M31, CenA, M81, M83), we assume they are complete down to the fiducial level of  $M_V < -9$  mag and  $\mu_{0,V} < 26.5$  mag arcsec $^{-2}$ . The actual completeness limits of these literature surveys are generally quite a bit deeper due to the closer proximity of these hosts relative to most ELVES hosts. Details can be found in the sources for those satellite lists (see Table 1).

While we do detect numerous candidate satellites fainter than  $M_V = -9$  mag, **all ELVES satellite lists and figures in this paper have a  $M_V < -9$  mag cut applied to them.**

## 5. CANDIDATE SATELLITE CONFIRMATION

In this section, we describe the process of confirming candidate satellites as actual physical satellites of a LV host. Many of the candidate satellites have prior distance information, either *HST*-based TRGB distances or redshift, but the majority do not. Thus, we rely heavily on efficient surface brightness fluctuation (SBF) measurements to provide a large number of distance constraints with modest ground-based data. We try to constrain the distance to as many candidate satellites as possible, but several remain with no distance

constraints. We keep careful track of these ‘unconfirmed/candidate’ satellites throughout this paper as they require special treatment in any analysis using ELVES satellite lists.

### 5.1. SBF Measurement

Details of the SBF measurement are given elsewhere (Carlsten et al. 2019b, 2021c), so we only provide a brief summary here. SBF entails measuring how ‘patchy’ a galaxy is in the semi-resolved regime. Distance smooths out Poisson fluctuations in the number of bright stars per resolution element such that a galaxy will look smoother further away. In measuring a galaxy’s SBF, this ‘patchiness’ is quantified as the ‘SBF magnitude’,  $\bar{M}$ .

To quantify this, we start with a smooth model of the galaxy’s surface brightness profile. The reddest band we have ( $r$  or  $i$ ) is modeled, as SBF is brighter and seeing is generally better for redder pass-bands (e.g Jensen et al. 2003; Carlsten et al. 2018). Due to the small sizes and low luminosities of most of the dwarfs, we always use a parametric Sérsic profile as a model for the smooth profile (see §6 for more information on the Sérsic profile photometry). This model is subtracted out from the raw image and the result is normalized by dividing it by the square root of this model. We then calculate the azimuthally averaged power spectrum of this result via a fast Fourier transform. The fluctuation power due to SBF is the component of the power spectrum on the scale of the PSF. For details on how we mask contaminants, we refer the reader to (Carlsten et al. 2019b, 2021c).

### 5.2. SBF Calibration

Due to the fact that the average brightness of stars in a galaxy will depend on the stellar population, the level of SBF also will depend on the stellar population present in a galaxy. Thus a calibration is used to relate the absolute SBF magnitude to galaxy color. For  $i$ -band measurements, we use the calibration provided in Carlsten et al. (2019b), while for  $r$ -band measurements, we use the calibration in Carlsten et al. (2021c).

These calibrations are specifically for CFHT/MegaCam. In this work we use five different telescope and instrument combinations (CFHT/MegaCam, Subaru/HSC, Blanco/DECam, Gemini/GMOS, and Magellan/IMACS) that all have Sloan-like  $r/i$  filters and that all will be slightly different. However, from experiments calculating theoretical SBF magnitudes using the MIST isochrones and synthetic photometry (Choi et al. 2016) for MegaCam, HSC, and DECam, we find that the SBF magnitudes are always the same within  $\sim 0.1$  mag,

which is small compared to the statistical error of the SBF measurement. With that said, we do incorporate a small  $-0.1$  mag adjustment to the CFHT-based calibration when using DECam filters. We do not perform any adjustments when using HSC, GMOS, or IMACS data, however. Kim & Lee (2021) show that their empirical SBF calibration in the HSC filter system is quite close to that of Carlsten et al. (2019b) with any difference more likely attributable to different masking strategies than filter differences.

### 5.3. SBF Distances

With the SBF measurements and calibration in hand, we can constrain the distance to each dwarf. Following Carlsten et al. (2021c), there are three outcomes to this measurement. First, if the SBF measurement is of high S/N ( $> 5$ ) with a distance that is consistent with that of the host within  $2\sigma$ , we consider the candidate satellite to be a ‘confirmed’ satellite. Second, if the  $2\sigma$  lower bound of the SBF distance constraint is beyond the distance of the host, we consider the candidate to be rejected as a background contaminant<sup>15</sup>. The actual distances of these objects are generally not known as the SBF measurement only sets a distance lower bound from the absence of measurable SBF. Third, if the SBF measurement is of too low S/N and the distance lower bound is within the distance of the host, the candidate is kept in the ‘unconfirmed/candidate’ satellite category. These objects may or may not be satellites and need deeper data or *HST* observations for their satellite status to be decided.

We use this cutoff of S/N  $> 5$  in the SBF measurement as a safeguard against false positive satellite confirmation. In our experience, this S/N level is roughly where SBF becomes clearly distinguishable from other sources of fluctuation power, such as scattered star-forming clumps in the galaxy or background galaxies. Carlsten et al. (2019a) used SBF to confirm two satellites around NGC 5457 (M101). These satellites had SBF S/N  $\gtrsim 7$ , above the threshold used here. Both of these have since been confirmed by *HST* TRGB distances in Bennet et al. (2019). Carlsten et al. (2019a) also discussed 2 other candidates as promising follow-up targets that had moderate signal with S/N  $\sim 2 - 3$ . The *HST* imaging of Bennet et al. (2019) showed that the galaxies were background contaminants. The small fluctuation signal appeared to be coming from unmasked background galaxies, not SBF. Using the threshold adopted

<sup>15</sup> Alternatively, the  $2\sigma$  upper bound to the distance could be nearer than the distance of the host (i.e. the candidate is foreground). However, this only happens once.

here, these two candidates would be conservatively included in the ‘unconfirmed/candidate’ satellite category.

In [Carlsten et al. \(2019b\)](#), we showed that the ground-based SBF distances agreed with *HST* TRGB distances with an RMS of 15%. While this is lower precision than the  $\sim 5 - 10\%$  precision that *HST* TRGB distances can attain ([Beaton et al. 2018](#)), it is still quite useful in confirming or rejecting candidate satellites as actual, physical satellites of a certain host. Thus, by including satellites with SBF distances within  $2\sigma$  of the host, we do expect that some near-field dwarfs (e.g. dwarfs analogous to the Local Group field dwarfs nearby to the MW) will be included as ‘satellites’. Experimenting with halos from the IllustrisTNG simulations ([Nelson et al. 2019](#); [Pillepich et al. 2018](#)), in [Carlsten et al. \(2021c\)](#), we found that this distance constraint led to a contamination of field interlopers of around 15 – 20%. Until more precise distances are possible, nothing can be done regarding this contamination, and it must be kept in mind when analyzing ELVES satellite lists. We note that this is a similar contamination fraction to what occurs when selecting satellites with a recessional velocity cut, as in the SAGA Survey ([Mao et al. 2021](#)).

#### 5.4. Other Distance Information

In addition to SBF measurements, we make use of TRGB distances and redshift information, when available. We search the Updated Nearby Galaxy Catalog of [Karachentsev et al. \(2004, 2013\)](#) for TRGB distances for all of the candidate satellites. Similarly, we query SIMBAD for any redshift information. Dwarfs with TRGB distances within  $1\sigma$  (or 1 Mpc, if no distance uncertainty is available) of the distance to their host are considered ‘confirmed’ with those outside of this range rejected as contaminants. For dwarfs with redshifts, those with velocities within 275 km/s of their host are confirmed satellites (e.g. [Mao et al. 2021](#)) while those outside this range are rejected. We note that the search for redshift information often occurs very early on in the candidate detection pipeline (in particular, in the visual inspection step) with background contaminants being removed at this point, even before the candidate satellite stage. Thus, many otherwise passable candidate satellites are not in the final candidate satellite lists since they had redshift information indicating they are background.

#### 5.5. Distance Results

The distance results for all the satellites for which we found or measured a distance are provided in Appendix E. There are three tables: one for dwarfs which get confirmed as satellites, one for dwarfs that get rejected as contaminants, and one for dwarfs that remain as possible/candidate satellites. We do not provide any distance

constraints for these latter dwarfs since any distance constraints for them are, by definition, not informative. However, we do list what data source was used, if any, in attempting an SBF distance.

Table 2 gives an overview of the distance results, including number of confirmed and rejected objects and number of lingering unconfirmed/possible candidates that did not have conclusive distance results. All together, including the five previously surveyed satellite systems (MW, M31, M81, CenA, NGC 5236), there are 338 confirmed satellites and 105 remaining candidates. 136 of these confirmed satellites are confirmed via SBF measurements. Only 31 (23%) of these SBF-based confirmations came from our previous work in [Carlsten et al. \(2021c\)](#). In total, there are 182 confirmed satellites with SBF distances, with 53 also having other distance confirmation (either TRGB or redshift)<sup>16</sup>. In all but four cases (7.5%), the SBF result agrees with the TRGB or redshift result. In these few exceptions, there is some issue (e.g. nearby bright star halo or irregular morphology) that clearly biases the SBF measurement, causing it to be inaccurate. These are discussed more in Appendix E.

#### 5.6. Candidate Satellite Contamination Estimate

In this section, we provide a simple estimate for the probability that each of the remaining unconfirmed/possible candidates is a real satellite of its host. To do this, we consider the fraction of similar candidate satellites that did have conclusive distance results (either from SBF or otherwise) that ended up being confirmed as a satellite.

We do this as a function of luminosity and surface brightness as the likelihood a candidate is an actual satellite will depend on these. This is similar in principle to the  $\mathcal{R}_{\text{sat}}$  estimate in the SAGA Survey (see §5.3 of [Mao et al. 2021](#)) that accounts for photometric candidates in that work that did not have robust spectroscopic measurements.

Figure 5 shows the surface brightness versus luminosity relation for candidates that had conclusive distance constraints (either confirmed as a satellite or rejected). The luminosity of a background contaminant is calculated as if it was at the distance of the host. In most cases, the actual distance of these contaminants are not known; the SBF results only show that they must be beyond the distance of the host. The confirmed satel-

<sup>16</sup> There are seven confirmed satellites with SBF distances and another distance measurement which we count as being confirmed by the SBF. This is because either the SBF distance was published before the other distance or the other distance measurement is quite ambiguous.

**Table 2.** Overview of Distance Constraints.

Name	$M_{K_s}^{\text{group}}$ (mag)	# candidates	# SBF conf.	# other conf.	# SBF rejected	# other rejected	# unconfirmed
NGC253	-23.96	8	0	5	0	2	1
NGC628	-22.81	17	7	6	3	0	1
NGC891	-23.83	8	1	2	1	0	4
NGC1023	-23.98	22	9	5	5	0	3
NGC1291	-23.97	21	12	2	1	2	4
NGC1808	-23.78	18	7	3	4	0	4
NGC2683	-23.50	12	3	3	2	0	4
NGC2903	-23.69	16	4	3	9	0	0
NGC3115	-24.14	27	13	4	8	0	2
NGC3344	-22.27	9	3	0	2	0	4
NGC3379	-25.37	85	16	28	17	2	22
NGC3521	-24.41	18	9	2	6	0	1
NGC3556	-22.76	17	0	1	2	1	13
NGC3627	-25.33	33	6	14	1	0	12
NGC4258	-23.94	21	3	4	12	1	1
NGC4517	-22.16	56	7	2	39	8	0
NGC4565	-24.27	11	2	2	2	0	5
M104	-25.01	18	11	0	3	0	4
NGC4631	-22.90	23	7	5	8	2	1
NGC4736	-23.10	17	0	7	0	3	7
NGC4826	-23.24	12	3	4	2	1	2
NGC5055	-24.04	13	5	4	0	0	4
NGC5194	-24.51	13	2	1	8	2	0
NGC5457	-23.16	42	2	7	33	0	0
NGC6744	-24.00	15	4	1	4	0	6
M31	-24.89	–	–	20	–	–	–
M81	-25.27	–	–	24	–	–	–
CENA	-24.41	–	–	22	–	–	–
NGC5236	-23.67	–	–	11	–	–	–
MW	-24.13	–	–	10	–	–	–
Total	–	552	136	202	172	24	105

NOTE—Overview of the distance confirmation results. For each host the total number of candidates, number of confirmed satellites, number of rejected background contaminants, and number of remaining unconfirmed/possible satellites are given. The numbers of confirmed and rejected dwarfs are split by whether the constraint is from SBF or otherwise (TRGB and/or velocity). Many of the satellites confirmed via redshift or TRGB also have an SBF distance with overall close agreement between the methods. The five previously surveyed hosts are given at the bottom with the bottom-most row listing the totals in each category.

lites show a clear relation between surface brightness and luminosity (this is explored in more detail in [Carlsten et al. 2021b](#)) whereas the rejected contaminants are generally higher surface brightness with smaller sizes. This is suggestive that most of the background contaminants are dwarf galaxies that are  $\sim 2 - 3\times$  further in distance than the LV hosts. The confirmed and rejected dwarfs are clearly segregated in the  $M_V - \mu_{0,V}$  plane such that the location of an unconfirmed/possible candidate in this plane contains information on how likely it is to be a real satellite.

To quantify the likelihood of each unconfirmed/possible candidate being real, we simply consider the 20 nearest candidates that had conclusive distance results in the  $M_V - \mu_{0,V}$  plane and calculate the fraction of those that were real satellites. We find very similar results if we had instead used anywhere between the 10 to 50 nearest candidates. The right panel of Figure 5 shows the value of the confirmed fraction at different locations in the  $M_V - \mu_{0,V}$  plane.

There are several simplifying assumptions being made in constructing this likelihood estimate. The first is that this estimate will certainly not take into account the host-to-host scatter in the contamination fraction due to prominent background groups along the line of sight. For instance, NGC 5457 and NGC 4517 have significant contamination due to rich background groups at  $D \sim 15 - 30$  Mpc.

Second, it implicitly assumes that the threshold in data quality required to confirm a satellite via SBF at a given luminosity and surface brightness is the same as that required to reject a background contaminant at that luminosity and surface brightness. It is easy to understand why this assumption is important if we consider an alternate scenario where, for instance, rejecting a background contaminant is possible with much worse data than that required to confirm a satellite (for instance if we required a  $S/N > 100$  measurement of the SBF to ‘confirm’ a dwarf). In this case, the rejected contaminants would be over-represented in the set of candidates with conclusive distance results, and Figure 5 would underestimate the likelihood that an unconfirmed candidate is a real satellite. We test this assumption in Appendix F where we show the results of applying the SBF confirmation and rejection criteria (see §5.3) to simulated dwarf galaxies across a range in luminosity and surface brightness. Taking two different hosts (NGC 4258 and NGC 3379) with high-resolution, deep data as examples, we simulate both dwarfs with SBF at the level appropriate for the distance of the host and dwarfs without SBF, representing background contaminants. Given a level of data quality, it is possible to

reject candidates that are fainter by about a magnitude (in luminosity or surface brightness) than the faintest candidates that can be confirmed with that data. This discrepancy would be decreased if we did not require a  $S/N > 5$  measurement of the SBF to consider a dwarf ‘confirmed’, but we explained the rationale behind that criterion in §5.3. This  $\sim 1$  mag difference is smaller than the dynamic range of the remaining candidates, and we expect this estimate of the confirmed fraction is fairly accurate. With that said, we recommend any analysis that uses ELVES satellite lists to test their results considering the cases where all or none of the remaining candidates are real satellites.

In total, summing these satellite probability estimates for all 105 remaining unconfirmed objects yields 49.8 real satellites, meaning that, most likely, there are an additional  $\sim 50$  actual satellites amongst the unconfirmed candidates. The SAGA Survey (§5.3 of [Mao et al. 2021](#)) estimates a total of 24 actual satellites amongst the candidates that did not have successful spectroscopic follow-up. As a fraction of the total number of confirmed satellites in each survey, this is a similar rate of failure in distance follow-up between the two surveys.

## 6. PROPERTIES OF THE SATELLITES

In this section, we turn to how we measure various properties of the satellites, including optical and UV photometry.

All satellite photometry is in the AB system and corrected for MW dust extinction using the  $E(B - V)$  maps of [Schlegel et al. \(1998\)](#) recalibrated by [Schlafly & Finkbeiner \(2011\)](#). We take the solar  $g$ -band magnitude to be  $M_g^\odot = 5.03$  mag ([Willmer 2018](#)).

### 6.1. Optical Sérsic Photometry

The primary photometric results come from fitting the optical images with Sérsic profiles. We refer the reader to [Carlsten et al. \(2021b\)](#) for an in depth description of how the Sérsic profiles are fit to the galaxies. In brief, the  $g$ -band images are fit first since they are generally deeper, and then the  $r$ - or  $i$ -band image is fit using the shape parameters fixed, varying only the intensity<sup>17</sup>. The masking threshold and image cutout size are adjusted in an iterative fashion to minimize the dependence that the final photometry results have on those choices.

As detailed in Table 1, the photometry always uses DECaLS/DECam or CFHT data. Even though we have

<sup>17</sup> For the few dwarf candidates in the NGC 891 field with only  $r$ -band coverage, we assume  $g - r = 0.4$ . Note that no SBF measurements (which require color) are attempted for these dwarfs.

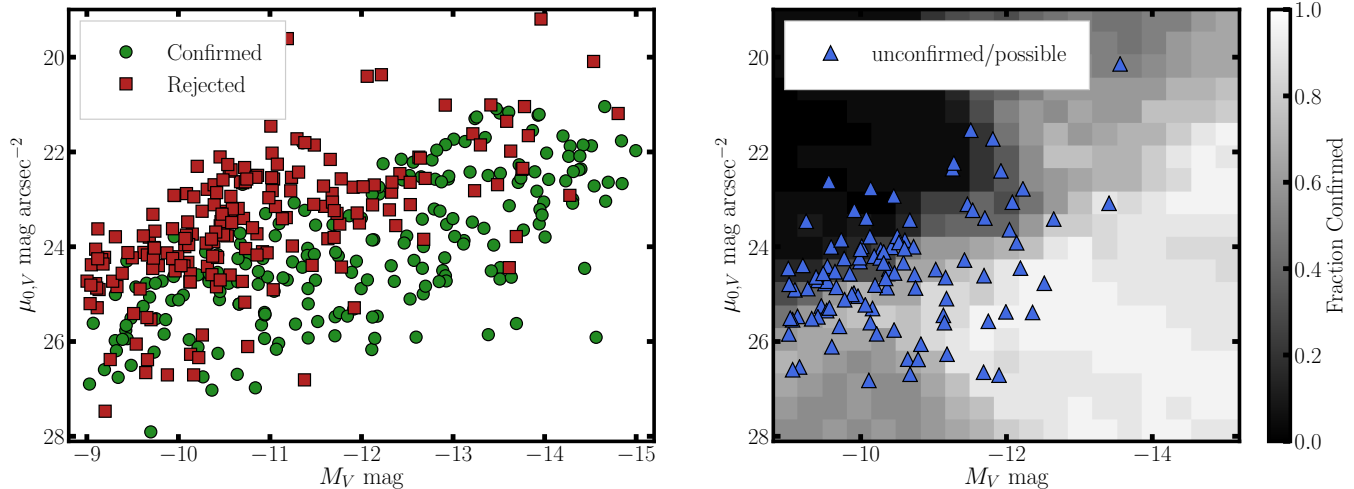


**Figure 5.** A simple estimate for the probability that the remaining unconfirmed/possible candidates are actual physical satellites. The left panel shows the luminosity and surface brightness of both the confirmed satellites and the rejected contaminants (if the latter were to be at the distance of their purported host) that had conclusive distance constraints. The confirmed satellites show a pronounced luminosity-surface brightness relation while background contaminants tend to be smaller with higher surface brightness. The right panel shows an estimate for the likelihood that a candidate will turn out to be a real satellite as a function of luminosity and surface brightness. This likelihood is estimated from the fraction of confirmed satellites out of the closest 20 confirmed or rejected candidates for each point on the  $M_V$ - $\mu_{0,V}$  plane. The locations of the actual remaining candidates are over-plotted.

deeper Gemini, Magellan, and Subaru data for many dwarfs for SBF, we do not present the photometry from that data in an attempt to limit the number of filter systems used. For three of the five previously surveyed systems (M81, CenA, and NGC 5236), we are able to provide photometry using our consistent methodology for almost all of the satellites. There were a few M81 satellites out of the DECaLS footprint and a few CenA satellites not covered in DECam archival data.

Following Carlsten et al. (2021b), we estimate uncertainties in the photometric parameters from image simulations where we inject Sérsic profile galaxies into CFHT or DECaLS data and quantify how well the input values are recovered. Carlsten et al. (2021b) also gives the equations we use to convert between  $g-r$  and  $g-i$  and convert  $g$ -band photometry into  $V$ -band.

For each dwarf, we use the color and  $g$ -band luminosity to estimate its stellar mass using the color-mass-to-light ratio relations in Into & Portinari (2013). For several of the brightest ( $M_V \lesssim -18$  mag) satellites, we did not attempt Sérsic photometry due to the clear inadequacy of a single profile in fitting these large, complicated galaxies. Instead, for these we simply provide stellar mass estimates calculated from 2MASS (Skrutskie et al. 2006)  $M_{K_s}$  values from Kourkchi & Tully (2017). For the MW and M31 satellites, we do not have colors but use average color-luminosity trends from the dwarfs that do to separately define luminosity-mass to

light ratio relations for early- and late-type dwarfs (see Equation 4 of Carlsten et al. 2021b).

Appendix G presents the main table for the photometry of the satellites. The confirmed and possible satellites are all given in one table, along with a flag to indicate which satellites have robust distance confirmation.

## 6.2. Galaxy Morphology

In addition to the optical photometric measurements, we visually classify each dwarf to have either late- or early-type morphology. We use all available optical imaging, including the deep data often available for SBF measurements, to make this distinction. Dwarfs with smooth, regular, and generally low surface brightness morphology are classed as early-types. On the other hand, dwarfs with clear star-forming regions, blue clumps, dust-lanes, or any other complications in their surface brightness profile are classed as late-type. Given the data available, we believe this is the most robust way to split the dwarfs. More details of this separation and color images of example dwarfs classified as early- and late-type can be found in Carlsten et al. (2021b).

## 6.3. GALEX Data

To complement the optical photometry, particularly to provide more information on recent star formation, we use archival GALEX (Martin et al. 2005) data to measure the UV photometry of the dwarfs, where available. We largely follow the methods of Greco et al.

(2018a) and Karunakaran et al. (2021). For each confirmed dwarf, we search the MAST archive for GALEX coverage. We find at least some coverage in NUV and FUV for a majority of the confirmed dwarfs, 271 in total. About a third of these are only covered by the shallow GALEX All-sky Imaging Survey with the remainder having deeper data, often from the Nearby Galaxy Survey (Gil de Paz et al. 2007) or the 11 Mpc H $\alpha$  and Ultraviolet Galaxy Survey (11HUGS; Kennicutt et al. 2008; Lee et al. 2011) both of which targeted many LV galaxies.

From the MAST archive, we download two files for each GALEX frame and filter: the intensity maps (`-int.fits` files;  $I$ ) and the high resolution relative response maps (`-rrhr.fits` files;  $R$ ). We use these frames to construct the variance image as:  $V = I/R$ .

Due to the fact that many of the dwarfs are not actually detected in the UV, we do not do Sérsic photometry like with the optical data. Instead, we perform aperture photometry using elliptical apertures with radii of twice the effective radii found from the optical Sérsic fits. Contaminating point sources are masked before performing the photometry with an initial `sExtractor` (Bertin & Arnouts 1996) run. The sky contribution to the flux is estimated from the median of 50 apertures placed in the vicinity of the galaxy.

The measured flux and uncertainty for the apertures are:

$$F = \sum_i I_i, \quad (2)$$

$$\sigma_F^2 = \sum_i V_i + \sigma_{\text{sky}}^2/N,$$

with  $i$  ranging over the pixels covered by the aperture and  $\sigma_{\text{sky}}$  being the standard deviation of sky values measured in the  $N$  sky apertures. We use the zeropoints given in Morrissey et al. (2007) to convert the measured fluxes to AB magnitudes and correct for galactic extinction using  $R_{\text{NUV}} = 8.2$  and  $R_{\text{FUV}} = 8.24$  (Wyder et al. 2007).

We do not attempt to correct for emission outside of the  $2r_e$  aperture. Even without this, we find good agreement when applying this methodology to the SAGA satellites (Mao et al. 2021) compared to the GALEX measurements of Karunakaran et al. (2021) who performed a curve-of-growth analysis. The aperture NUV magnitudes are biased high by  $\lesssim 0.1$  mag. We also find good agreement with the FUV fluxes in the UNGC (Karachentsev et al. 2013) for ELVES satellites that are in that catalog.

Appendix G presents a table with the UV photometry for the confirmed satellites that have it. For dwarfs that

had a  $S/N < 2$  result, we report  $2\sigma$  upper limits to the UV flux.

## 7. PROPERTIES OF THE SATELLITE SYSTEMS

In this section, we briefly explore features and trends amongst the satellite systems, including the luminosity functions and abundance, spatial distribution, and star formation properties. In-depth comparisons with galaxy formation models are out of the scope of this survey overview paper but will be pursued in future papers.

### 7.1. Satellite Abundance

The question of satellite abundance around MW-like galaxies has been a central component of the debate around ‘small-scale problems in  $\Lambda$ CDM’ for decades (e.g. Moore et al. 1999; Klypin et al. 1999; Bullock & Boylan-Kolchin 2017). The abundance and luminosity function of satellites are sensitive probes to the underlying stellar-to-halo-mass relation (SHMR; e.g. Garrison-Kimmel et al. 2017; Nadler et al. 2020). Satellite abundance is also an important probe of recent accretion events experienced by a host (Smercina et al. 2021). Using early results from ELVES, in Carlsten et al. (2021c), we showed that the MW’s abundance of satellites was quite typical compared to LV systems of similar mass. We also showed that this abundance and the host-to-host scatter in satellite abundance were well-reproduced by recent galaxy formation models. In this section, we briefly highlight some abundance-related results and provide a comparison with recent SAGA Survey results (Mao et al. 2021).

Figure 6 shows the relation between satellite abundance and host mass, as proxied by the group  $K$ -band luminosity. The group  $K$ -band luminosity is used instead of just the host’s in order to account for the groups with multiple massive primaries, like M81, NGC3627, and NGC3379. The top panels show all satellites down to the ELVES limit of  $M_V < -9$  mag while the bottom panels show just the bright satellites,  $M_V < -12$  mag. The left panels show the inner satellite systems,  $r_{\text{proj}} < 150$  kpc, while the right panels show abundances out to 300 kpc for the systems that are surveyed out that far. Running averages are shown in the blue bands. The unconfirmed satellites are included in the satellite counts using their satellite probability from §5.6 (Figure 5). The solid errorbars show the  $1\sigma$  spread in abundance when stochastically including, or not, the unconfirmed candidates over many trials. The dotted errorbars show the upper and lower limits of abundance in the cases where all, or none, of the unconfirmed candidates turn out to be physical satellites. The lower panels show few errorbars because there are few unconfirmed candidates more luminous than  $M_V = -12$  mag.

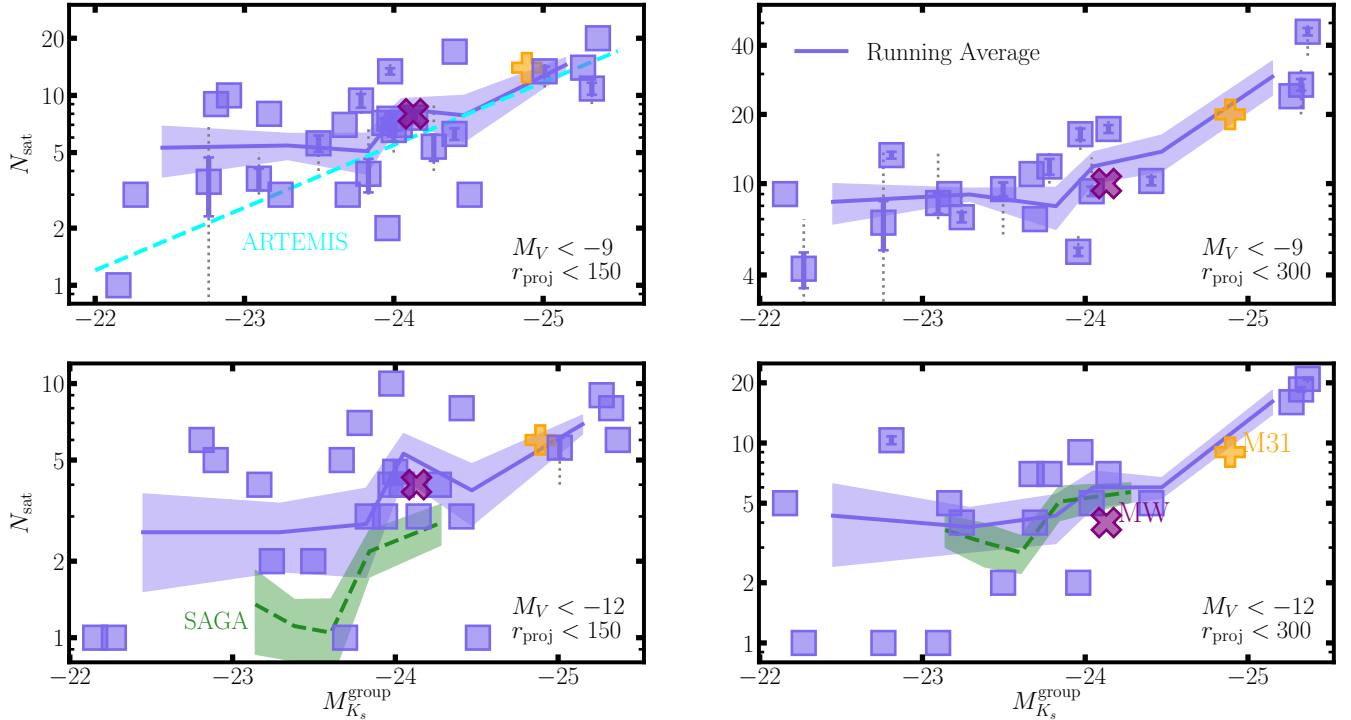


**Figure 6.** The satellite abundance versus the  $K$ -band luminosity of the host. Top row shows all satellites  $M_V < -9$  mag, while the bottom row is restricted to the bright,  $M_V < -12$  mag, satellites. The left panels show all hosts, but are restricted to satellites within  $r_{\text{proj}} < 150$  kpc. Right panels show the subsample of hosts that are complete out to 300 kpc. Solid errorbars show the uncertainty in satellite abundance due to the unconfirmed satellites, using the satellite probabilities from §5.6. Dotted errorbars show the upper and lower limits of abundance if all, or none, of the unconfirmed candidates are actual satellites. The MW and M31 are plotted individually in the crosses. The solid lines show running averages. The abundance- $M_K$  relation from the ARTEMIS simulations (Font et al. 2021a) is shown in the upper left. The average trends from the SAGA Survey (Mao et al. 2021) are shown in the bottom panels.

In all panels, a strong trend is seen between satellite abundance and host mass, as expected. Both the MW and M31 seem quite typical in terms of satellite abundance amongst similar mass systems. We found this result in Carlsten et al. (2021c) and show it here with a much larger statistical sample of hosts and satellites. This result is one of the primary results, if not the main result, from the ELVES survey.

In the top left panel, we show the scaling relation fit from the ARTEMIS simulation suite in Font et al. (2021a). This particular fit was using the ‘LV-selection’ which was chosen to mimic roughly the ELVES luminosity and surface brightness sensitivity (and restricted to the inner  $r_{\text{proj}} < 150$  kpc regions). The fit reproduces the average abundance well, particularly at high host mass, but seems to underpredict the satellite abundance somewhat at the lowest masses. In fact, in all panels, the observed satellite abundance seems to flatten out at the lowest masses. Note that several of these low-mass hosts have complete, or nearly complete, distance confirmation for all candidates so this is not simply a floor caused by background contaminants. Including satellite

abundances for even lower-mass, LMC-like, hosts will be an important extension of this work (see Carlin et al. 2016, 2021; Müller & Jerjen 2020, for initial work in this direction).

In the bottom panels we show a comparison to the average trends from the SAGA Survey (Mao et al. 2021). The  $M_V < -12$  mag cut used closely matches the luminosity limit of SAGA. The redshift follow-up incompleteness in SAGA is accounted for using the satellite probability model calculated in §5.3 of Mao et al. (2021). This is treated in an analogous way to the unconfirmed/candidate satellite correction used in ELVES. SAGA also shows a relation with higher  $K$ -luminosity hosts having higher satellite abundance. ELVES satellite abundance is slightly higher than SAGA, with the difference being quite noticeable for the inner,  $r_{\text{proj}} < 150$  kpc, satellites.

Figure 7 shows a more detailed look at the ELVES satellite luminosity function (LF). The average differential luminosity function is shown for both  $r_{\text{proj}} < 150$  and  $r_{\text{proj}} < 300$  kpc. The unconfirmed candidate satellites are included using their satellite probability values

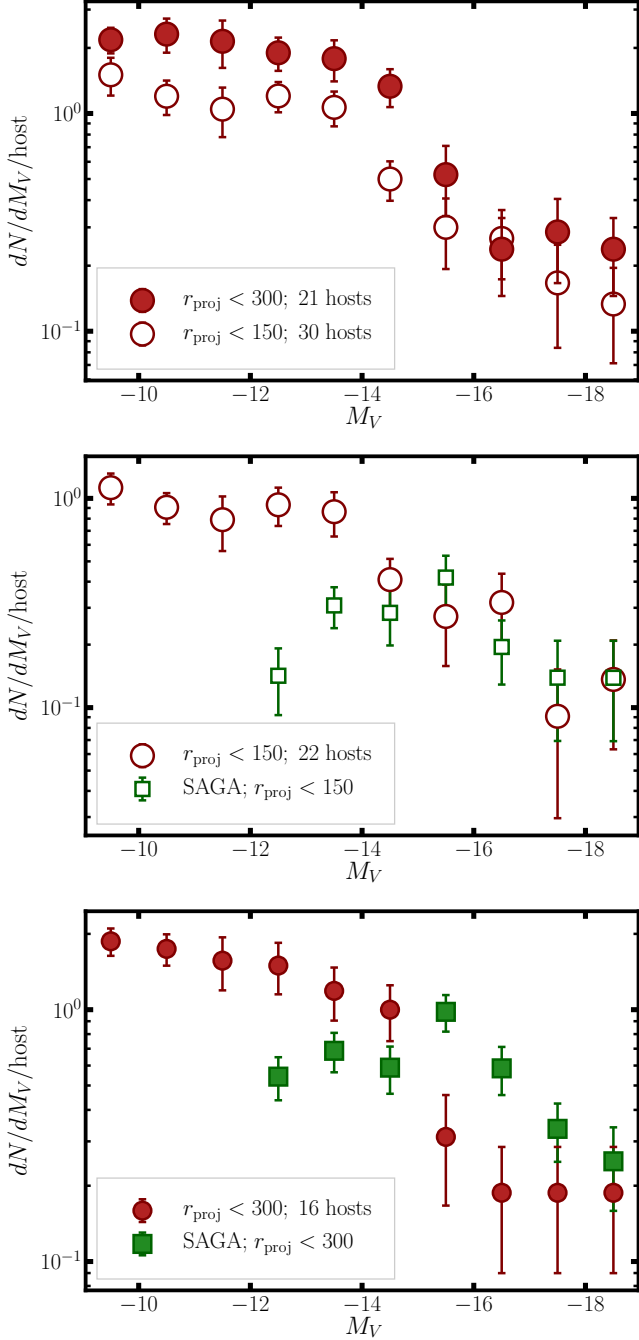


**Figure 7.** The average satellite abundance per host in 1 mag wide luminosity bins within both  $r_{\text{proj}} < 150$  and 300 kpc. The legends indicate the number of hosts contributing to each stacked LF. The middle and bottom panels show a comparison to the SAGA Survey (Mao et al. 2021). Only ELVES hosts that would satisfy the SAGA selection criteria are included. The SAGA Survey LF shows a noticeable drop below  $M_V > -15$  mag compared to ELVES, even when including a correction for incompleteness in redshift follow-up in that survey.

from §5.6. The errorbars show the error in the mean number of satellites per host within each 1 magnitude wide bin. This is calculated as the standard deviation of satellite abundance across the hosts divided by  $\sqrt{N_{\text{host}}}$ . Thus, these errorbars account for uncertainty coming from the intrinsic host-to-host scatter in satellite abundance. The errorbars are essentially the same as would be calculated from bootstrapping the host sample. Within the errorbars, the average LFs appear to be simple power laws. The  $r_{\text{proj}} < 300$  kpc LF flattens somewhat at the lowest luminosities, likely due to ELVES starting to lose the lowest surface brightness satellites (cf. Figure 4). The satellite abundance within 150 kpc is generally  $\sim 2\times$  lower than that out to 300 kpc.

The middle and bottom panels of Figure 7 show a comparison with the SAGA results. In this comparison, we remove the massive ELVES hosts that would not satisfy the SAGA host  $M_{K_s}$ , isolation, and/or halo mass criteria. The SAGA host  $M_{K_s}$  requirement ( $M_{K_s} > -24.6$  mag) removes M104 and M31, the isolation criteria (no satellite with  $M_{K_s}$  within 1.6 mag of the host) removes NGC 1808, NGC 5194, NGC 3379, and M81, and the halo mass cut ( $M_h < 10^{13} M_{\odot}$ ) removes CenA and NGC 3627. In applying the halo mass cut, we remove any host that has either of the two halo mass estimates provided in the group catalog of Kourkchi & Tully (2017) above  $10^{13} M_{\odot}$ <sup>18</sup>. One halo mass estimate comes from group kinematics while the second comes from total  $K$ -band luminosity. If the two estimates differ by more than 0.5 dex, we consider the luminosity-based estimate as the more robust. Note that we still include the six ELVES hosts that are actually *below* SAGA’s host  $M_{K_s}$  range (NGC 628, NGC 3344, NGC 3556, NGC 4517, NGC 4631, and NGC 4736). There is no change to the conclusions if these are cut as well, albeit the ELVES statistics become poorer. In comparing with SAGA, we additionally only include satellites more than 15 kpc projected from their hosts as this is the estimated inner radial limit of the SAGA satellite lists (Y.-Y. Mao, private communication). The SAGA results make use of our own Sérsic photometry for the SAGA satellites, which we describe below (§7.3).

In order to account for possible differences in the host  $M_{K_s}$  distribution even with the SAGA selection criteria applied, we have tried scaling the host abundances to a standard value of  $M_{K_s} = -23.5$  mag. We use the abundance- $M_{K_s}$  relation of Font et al. (2021a) to reduce

<sup>18</sup> We believe that the halo mass estimates from the group catalog of Kourkchi & Tully (2017) are more likely accurate for LV hosts than the group catalog (Lim et al. 2017) that the SAGA Survey uses.

the weight of more massive hosts and increase the weight of less massive hosts in the average LF stack. We find that this re-scaling has only a minor effect on the average LFs and is thus not shown.

Table 3 lists the average satellite abundance per host in different radial and luminosity ranges. The bright ( $-19 < M_V < -15$  mag) ELVES satellites appear quite centrally concentrated with a similar abundance per host regardless of radial range. As stated in the table, the host sample is slightly different between the  $r_{\text{proj}} < 150$  and  $< 300$  kpc cases, as the former includes 6 more hosts complete to only 150 or 200 kpc. In the case where we restrict the  $r_{\text{proj}} < 150$  kpc sample to be the same as in the  $r_{\text{proj}} < 300$  kpc case, there are fewer bright satellites in the inner radial range (these values are given in parentheses).

Interestingly the average SAGA LF is higher than that of ELVES at bright ( $M_V < -15$  mag) luminosities for the 300 kpc case. It is unclear what is causing this higher abundance. Dwarfs at these luminosities in the Local Volume are hard to miss and most, if not all, will have been cataloged years ago. The Updated Nearby Galaxy Catalog (UNGC) of Karachentsev et al. (2013) will be essentially complete for these dwarfs, and we show in Appendix D that ELVES is complete to UNGC entries within our coverage footprints. Future work will be needed to understand this difference, including a detailed analysis of the different host samples and expected interloper fractions (i.e. false positives amongst distance confirmed satellites).

On the other hand, the SAGA abundance is lower at magnitudes fainter than  $M_V \sim -15$  mag in both considered radial ranges. This has the result of the SAGA average LF being much shallower than the average ELVES LF. Note we are including the correction for incompleteness in the spectroscopic follow-up of SAGA (see §5.3 of Mao et al. 2021), which helps close the gap at faint luminosities but does not close it fully. There appears to be  $\sim 1.5 - 2$  more satellites in the  $-15 < M_V < -12$  mag range per ELVES host than in SAGA with most ( $\sim 1.5$ ) of the difference being in the inner 150 kpc regions.

The dearth of faint satellites in SAGA and the dropping average LF are suggestive of incompleteness beyond what is accounted for in the model for incomplete redshift follow-up. In particular, these results point to incompleteness in the DECaLS (Lang et al. 2016; Dey et al. 2019) object detection and targeting catalogs used in SAGA. We have experimented with applying various surface brightness cuts to the ELVES satellite lists to see if a simple cut in surface brightness can explain the discrepancy. When applying such a cut, the ELVES LF does indeed flatten and even drop, but it does not reach

the SAGA points unless a fairly bright surface brightness cut ( $\langle \mu_V \rangle_e \sim 24.5$  mag arcsec $^{-2}$ ) is applied. This is unrealistically high as there are a number of SAGA satellites fainter than this. We therefore suspect that while surface brightness incompleteness in the DECaLS catalogs is part of the problem, there are likely other issues as well. For instance, shredding can cause objects that otherwise would be brighter than SAGA's  $M_r = -12.3$  mag limit to drop below. We emphasize that this is not due to an inherent limitation of Legacy Survey or Dark Energy Survey data but instead due to the specific objection detection algorithms used in making the SAGA targeting catalogs. After all, in ELVES we use this data to detect dwarfs as faint as  $\mu_{0,V} \sim 27$  mag arcsec $^{-2}$ .

In addition to observational incompleteness, it is conceivable that host-to-host scatter and/or physical differences in the hosts are playing a role in the discrepancy. For instance, it is possible that, due to some circumstance of the LV's cosmic environment, LV hosts are more satellite abundant than average hosts of their mass. Neuzil et al. (2020) argue that the LV is an outlier in terms of overall dwarf (satellite and field) abundance compared to  $\Lambda$ CDM simulations. This will be something that might be explored with the final, 100-host SAGA sample. We note that there is no 16-host (to match the number of SAGA-selected ELVES hosts that are complete to 300 kpc) sub-sample of the current 36-host SAGA sample that is able to come close to the steepness and abundance of the average ELVES LF, but the complete SAGA sample might change this. In the end, multiple effects (incompleteness, host-to-host scatter, and/or differences in the host samples) are likely playing a role.

## 7.2. Satellite Spatial Distribution

The radial distribution of satellites is an important observable to test the disruptive effect of the host's central disk and the level of physical versus numerical (due to low-resolution) disruption in simulations (e.g. van den Bosch et al. 2018; Samuel et al. 2020). In Carlsten et al. (2020b), we found that the ELVES satellite systems surveyed up to that point (that paper used 6 hosts surveyed with CFHT/MegaCam data and 6 surveyed in the literature) showed significantly more concentrated radial distributions of satellites than predicted by galaxy formation simulations. We did not have a complete explanation, but discussed both artificial disruption in the simulations or a bias in the observed sample relative to the general population of massive hosts. The 36 hosts presented in the SAGA Survey (Mao et al. 2021) did not show similarly concentrated profiles, suggesting the latter explanation. In this section, we explore the satel-

**Table 3.** Bright vs. faint satellite abundances per host

Radial coverage	Survey	$N_{\text{hosts}}$	$\langle N_{\text{sat}} \rangle$ with $-15 < M_V < -12$ mag	$\langle N_{\text{sat}} \rangle$ with $-19 < M_V < -15$ mag
$r_{\text{proj}} < 150$ kpc	SAGA	36	$0.73 \pm 0.12$	$0.89 \pm 0.16$
	ELVES	22	$2.2 \pm 0.31$	$0.82 \pm 0.2$
		(16)	( $1.94 \pm 0.37$ )	( $0.56 \pm 0.22$ )
$r_{\text{proj}} < 300$ kpc	SAGA	36	$1.82 \pm 0.2$	$2.15 \pm 0.25$
	ELVES	16	$3.68 \pm 0.61$	$0.88 \pm 0.23$

NOTE—Average number of satellites per host for different radial and luminosity ranges. Note that the ELVES host sample is slightly different between the  $r_{\text{proj}} < 150$  and  $< 300$  kpc cases. The values in parentheses give the  $r_{\text{proj}} < 150$  kpc abundances for the same host sample as in the  $r_{\text{proj}} < 300$  kpc case. Many of the hosts complete to only 150 kpc are among the richest ELVES hosts.

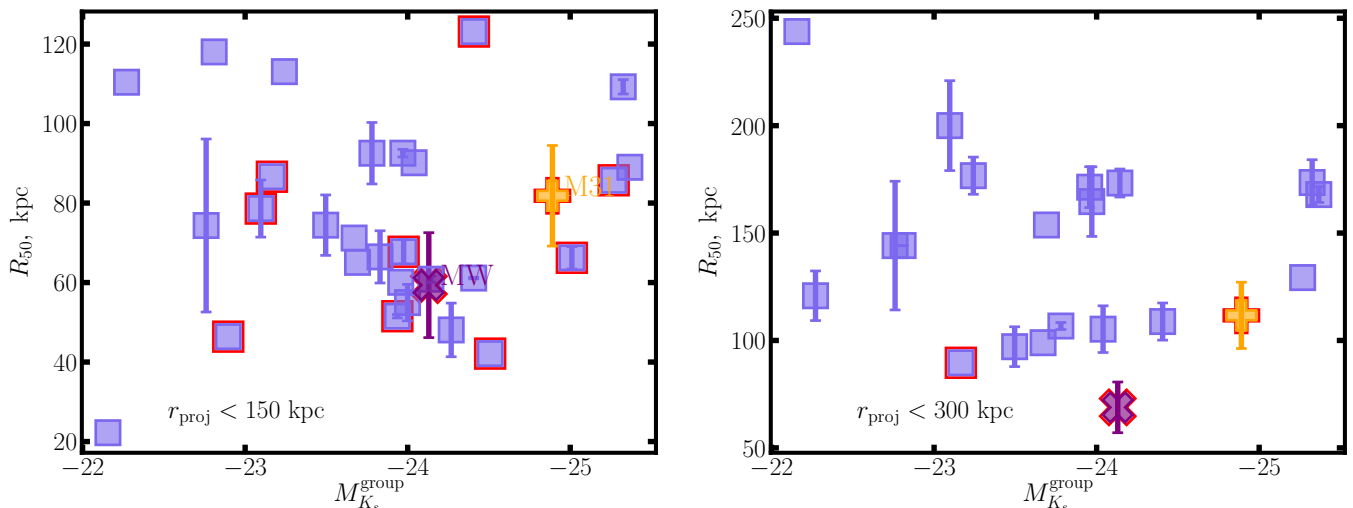


**Figure 8.**  $R_{50}$ , the radius containing half of satellites for a given host, versus host  $K_s$ -band luminosity. The left panel shows the results restricted to  $r_{\text{proj}} < 150$  kpc, and the right panel shows the results out to 300 kpc, for the hosts that are surveyed out that far. The MW and M31 points show the average projected  $R_{50}$  if the satellite systems were re-observed at a distance of 7 Mpc, with errorbars indicating the spread due to different viewing angles. For the other points, the errorbars indicate the uncertainty due to unconfirmed candidate satellites without distance information. Points outlined in red were in the previous study of Carlsten et al. (2020b).

lite radial profiles using the full, nearly volume-limited, ELVES sample of hosts.

Figure 8 shows  $R_{50}$ , the projected radius encompassing half the satellites of a given host, versus host  $K_s$ -band luminosity both within  $r_{\text{proj}} < 150$  kpc and 300 kpc. Since this is a projected radius for the LV hosts, we ‘re-observe’ the MW and M31 systems at a distance of 7 Mpc using the known 3D structure of these systems and considering many different sight-lines. The points show the average projected  $R_{50}$  along with the  $1\sigma$  spread due to sight-line differences. The errorbars on the other hosts show the  $1\sigma$  spread when stochastically including, or not, the unconfirmed candidate satellites according to their satellite probabilities from §5.6. The points outlined in red were included in the Carlsten et al. (2020b)

sample. We note that the  $R_{50}$  values for some of these hosts, particularly CenA and M31, are somewhat different from those in Carlsten et al. (2020b). This is due to slightly different satellite lists being used for these hosts. For CenA, here we use largely our own photometry to select which satellites have  $M_V < -9$  (and hence be included in ELVES), while Carlsten et al. (2020b) used literature photometry, leading to slightly different inclusion. For M31, here we simply use the photometry of McConnachie (2012) while Carlsten et al. (2020b) used various other literature sources, again leading to a slightly different list of satellites.

The hosts included in Carlsten et al. (2020b) tend to be on the more concentrated side, with several of the most concentrated in all of ELVES falling in that group.

This is especially the case for the  $r_{\text{proj}} < 300$  kpc sample where Carlsten et al. (2020b) only had three hosts surveyed out that far and two of them (MW and NGC 5457) are the two most concentrated hosts in all of ELVES. This would suggest that the discrepancy found in that paper was at least partly due to an unlucky and small sample of hosts. With that said, Carlsten et al. (2020b) found that simulations generally had  $R_{50} \sim 90$  kpc and  $\sim 150$  kpc for the  $r_{\text{proj}} < 150$  and  $r_{\text{proj}} < 300$  kpc cases, respectively. Comparing with the complete ELVES sample in Figure 8, the observed systems still appear systematically more concentrated, but an in-depth comparison with simulations is needed for a firm conclusion.

Figure 9 shows a histogram of the projected satellite-host separations, comparing with the SAGA Survey results. To be more comparable to SAGA, we again remove the massive ELVES hosts that would not satisfy the SAGA selection criteria as described in §7.1. In the left panel, we show both the complete ELVES satellite sample ( $M_V < -9$  mag) and just the brighter,  $M_V < -12$  mag, satellites to compare with SAGA. Unconfirmed candidate satellites are again included weighted by their satellite probabilities from §5.6. To include all the hosts, we just plot satellites out to 150 kpc projected. The errorbars show the standard error in the mean number of satellites per host in each radial bin.

Overall, the ELVES systems show higher satellite abundances with  $\sim 1.5$  more satellites per host than in SAGA, similar to Table 3. Interestingly, most of the difference between ELVES and SAGA is at quite small projected radii,  $r_{\text{proj}} \lesssim 75$  kpc. Assessing the level of significance of the discrepancy with a 2-sample Kolmogorov–Smirnov test is not straightforward as the unconfirmed satellites are included statistically. Specific realizations of the unconfirmed satellites yield  $p$ -values  $\lesssim 5 \times 10^{-3}$  in all cases, however, indicating the discrepancy is significant. The right panel shows just the satellites in the  $-15 < M_V < -12$  mag range singled out in Table 3, again showing the difference in abundance is due to satellites very near the host.

The difference in radial concentration between ELVES and SAGA is again suggestive of incompleteness in SAGA. If the incompleteness in the DECaLS targeting catalogs used by SAGA is due, at least in part, to lack of low surface brightness sensitivity, this radial trend would make sense. Inner satellites in ELVES are lower in surface brightness by  $\sim 0.5$  mag arcsec $^{-2}$ , likely due to earlier quenching or enhanced tidal effects, but we leave an exploration of this to future work.

We note that the radial disagreement mostly goes away (but the abundance disagreement remains the same as in Table 3) if we do not include the ELVES hosts

only surveyed out to 150 or 200 kpc. There are six of these<sup>19</sup>: NGC 891, NGC 1023, NGC 4258, NGC 4565, NGC 4631, and NGC 6744, which include the most centrally concentrated hosts from Carlsten et al. (2020b). All of these hosts are complete to at least  $r_{\text{proj}} = 150$  kpc, the outer limit shown in Figure 9, and we argue extensively in Carlsten et al. (2020b) that their central concentration is not due to any observational systematic. Thus, there is no justification for their exclusion from Figure 9, but this highlights the host-to-host scatter in satellite radial profiles and how a few extreme systems can affect the average.

### 7.3. Satellite Star-forming Properties

Dwarf satellites experience profound effects as the result of their association with a massive host galaxy. The hot gas halo of the host galaxy can remove the gas reservoirs of the dwarfs quickly via ram pressure stripping (Gunn & Gott 1972; Grebel et al. 2003; Boselli et al. 2008) or at least cut off the supply of fresh gas to the dwarfs. This is often invoked to explain why dwarfs in the LG are primarily gas-poor and quenched (Grcevich & Putman 2009; Spekkens et al. 2014; Putman et al. 2021). Furthermore, it is thought that the tidal field of the host induces a morphological transformation of an initially gas-rich dwarf irregular to a dwarf spheroidal (e.g. Mayer et al. 2006; Kazantzidis et al. 2011, 2013).

However, there is growing uncertainty as to whether these results based on the LG can generalize to the overall satellite galaxy population. There is some evidence from simulations that a double-primary configuration like in the LG can, indeed, boost satellite quenching efficiency (Garrison-Kimmel et al. 2019b). Additionally, the SAGA Survey has reported much lower quenched fractions amongst their MW-analog targets (Geha et al. 2017; Mao et al. 2021), due to the ubiquitous presence of H $\alpha$  emission. In this section, we use the ELVES satellite systems to address the question of whether the LG is atypical or not in this regard. We also show various comparisons between the ELVES satellite sample and that of the SAGA Survey.

Due to the fact that ELVES is a photometric survey, determining the quenched fraction of satellites is not straight-forward. Without spectroscopic follow-up data, dwarf color and morphology are the best indicators of star-forming activity available. As described in §6.2, we visually split the dwarfs into early- and late-type based on the presence of clear indicators of active star-formation, such as blue clumps, dust lanes, and ir-

<sup>19</sup> For reference there are 16 hosts included in this figure complete to 300 kpc.

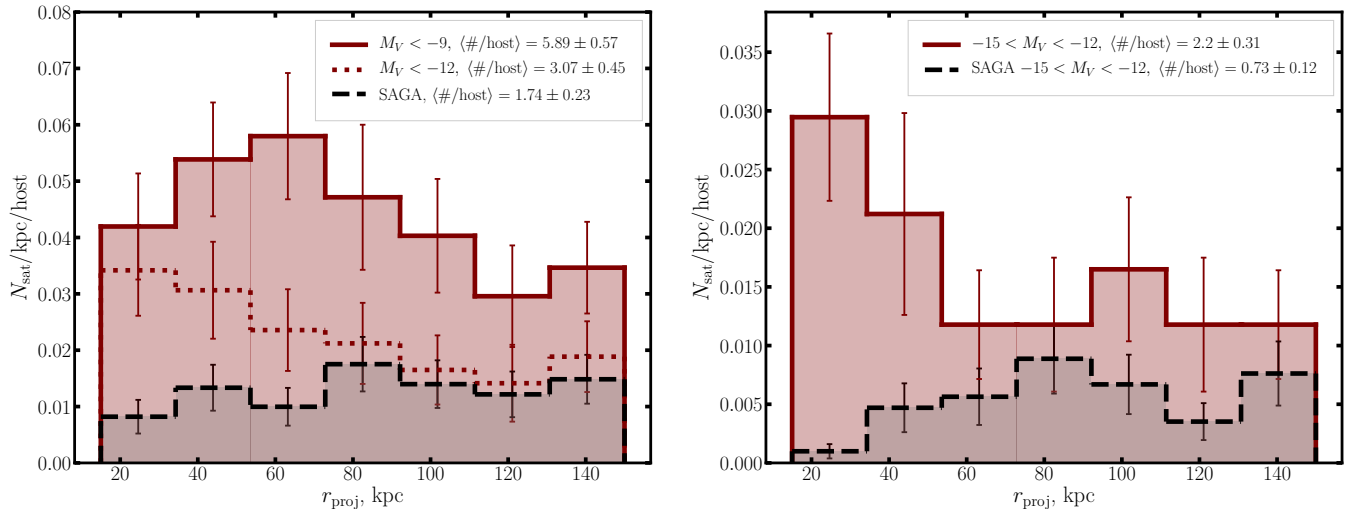


**Figure 9.** Histogram of the projected separations of satellites from their hosts. The massive hosts that would not meet the SAGA selection criteria are not included. Left panel shows all ELVES satellites along with just the brighter satellites ( $M_V < -12$  mag). Right panel shows just satellites in the intermediate luminosity range  $-15 < M_V < -12$  mag. The satellites from the SAGA Survey (Mao et al. 2021) are also shown, which exhibit fewer satellites per host and less central concentration.

regular morphology. Based on a limited sub-sample that have  $H\alpha$  and/or HI measurements, we find that these measurements closely corroborate the visual classification. Early-type dwarfs are almost always characterized by small or non-existent HI reservoirs and/or no  $H\alpha$  emission, indicating quenched star formation. However, instead of just trusting that this correlation holds true for the whole satellite sample, we also perform more ‘apples-to-apples’ comparisons with the SAGA satellites using color.

The first comparison we show is that of UV-optical color versus dwarf luminosity in Figure 10. The ELVES satellites are colored according to their morphology while the SAGA satellites are colored according to the  $H\alpha$  emission criterion used in Mao et al. (2021) (whether the equivalent width is more or less than  $2\text{\AA}$ ). The photometry (optical and UV) for the SAGA satellites come from our own measurements using the same methods as for ELVES, although we find largely the same results if we use SAGA UV photometry from Karunakaran et al. (2021) and optical photometry from Mao et al. (2021). We incorporate the redshift incompleteness model of SAGA by also including SAGA candidate satellites that Mao et al. (2021) infer to have satellite likelihoods  $> 0.1^{20}$ . These candidates have Sérsic optical and

GALEX photometry measured in the same way as the confirmed SAGA satellites and are shown in the faint open symbols. Since, by definition, they have no spectral information, these points are not colored to indicate  $H\alpha$  presence.

The early- and late-type ELVES satellites clearly separate in this plane with early-type dwarfs having redder UV-optical color. Since optical color is part of the visual classification (in addition to morphology), this is largely just a reflection of UV-optical color being correlated with optical color. The SAGA satellites without  $H\alpha$  generally have red UV-optical color, as well. This is unsurprising as both  $H\alpha$  and UV emission are well-established tracers of recent star formation in dwarfs (Lee et al. 2009; Karachentsev & Kaisina 2013) and generally show good consistency. The few UV-optically blue SAGA satellites without  $H\alpha$  are quite blue and irregular in optical DECaLS imaging, and it seems likely they do emit in  $H\alpha$  but the emission was possibly missed by the SAGA fiber placement. Other than these exceptions, the SAGA quenched satellites appear similar to the ELVES early-type dwarfs, providing further support that the early-type morphology classification is a robust indicator of quenched star formation.

There appears to be significantly more ELVES early-type dwarfs than quenched SAGA dwarfs. This is shown in the histogram in the right panel which includes dwarfs of an intermediate luminosity ( $-15 < M_g < -12$  mag). Candidate SAGA satellites without distance confirmation are included weighted by their satellite probability inferred by Mao et al. (2021). No correction is made for ELVES candidate satellites without distance measure-

<sup>20</sup> As described in §5.3 of Mao et al. (2021), the candidate satellites in SAGA without redshift split into two groups: several thousand candidates with individually very low likelihood of being satellites ( $\sim 0.1\%$ ) and  $\sim 70$  candidates with much higher probabilities of being a satellite ( $\sim 25\%$ ). In making this cut, we are only considering the latter group.

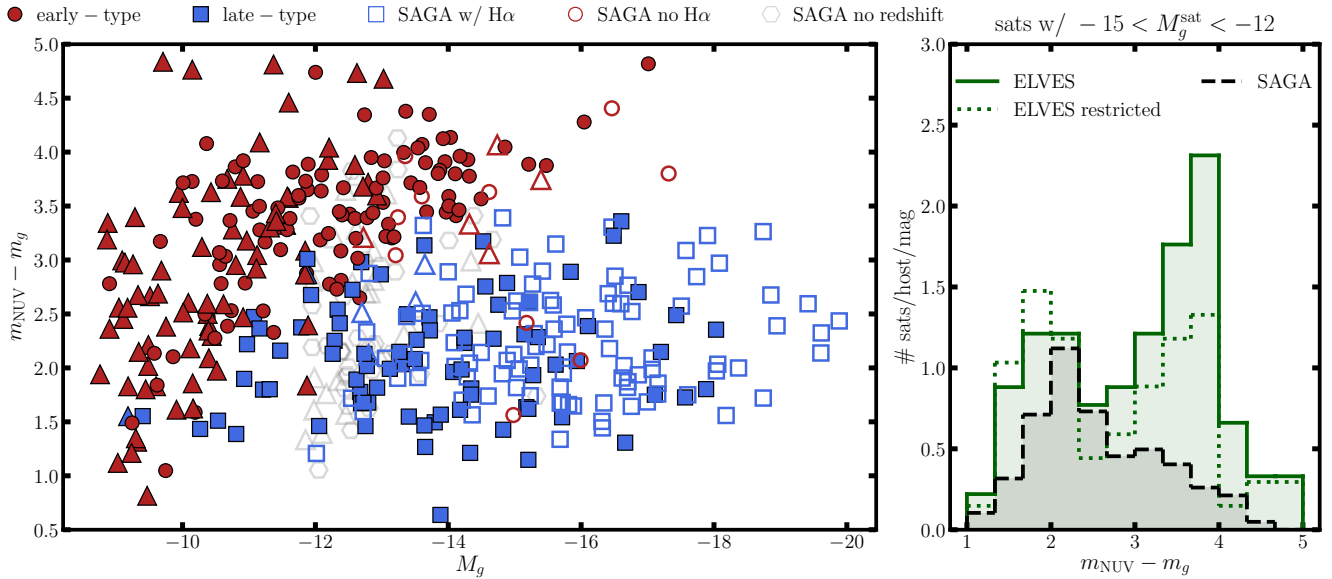


**Figure 10.** The NUV- $g$  color versus luminosity for the ELVES satellites. The points are colored based on their morphology class (early- or late-type). The two morphological classes clearly separate in this plane. Shown in the open symbols are the SAGA satellites from Mao et al. (2021), colored by whether or not they have H $\alpha$  emission. Dwarfs not detected in GALEX with  $S/N > 2$  are shown as triangles indicating  $2\sigma$  upper limits to their NUV flux. In general, the quenched SAGA satellites do have similar red UV-optical color to the ELVES early-types, however, there are far more ELVES early-type satellites. This is shown in the histograms in the right panel. Both SAGA and ELVES show a bimodality in UV-optical color corresponding to quenched and star-forming satellites. However, the ELVES quenched population is significantly larger. The dotted histogram shows the ELVES sample without the hosts more massive than the SAGA selection criteria. Note that the SAGA completeness limit is  $M_g \lesssim -12$  mag and that for ELVES is  $M_g \lesssim -9$  mag.

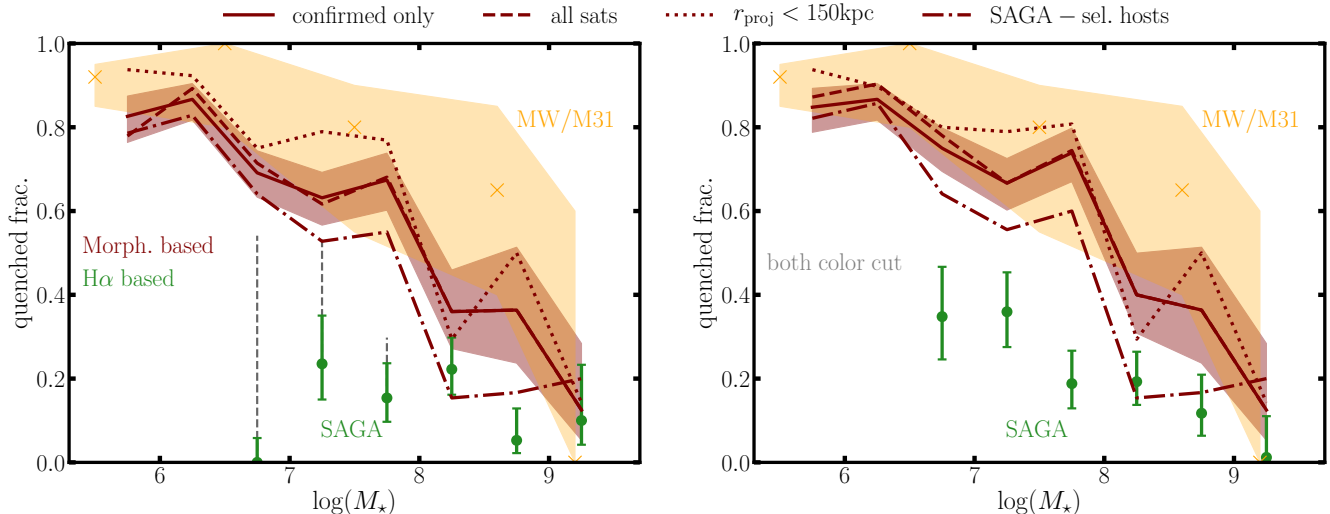
ments since there are essentially none in this luminosity range. Satellites with only GALEX NUV upper limits are included in this histogram at the location of their upper limit. Since only a few of the ELVES or confirmed SAGA satellites in this luminosity range have only GALEX upper limits there is no worry that the histograms are biased to blue NUV- $g$  colors because of weak NUV flux upper limits. However, many of the SAGA candidate satellites without redshifts have only GALEX upper limits. To ensure the SAGA histogram is not unfairly biased blue, we give the candidates that have similar red optical colors to the ELVES early-types (see the end of this section for the specific cut in color-magnitude space) an NUV- $g$  color of  $\sim 3.7$  mag, similar to the ELVES early-types.

Both ELVES and SAGA show bimodality in UV-optical color, corresponding to quenched and star-forming populations. The dotted green histogram shows the ELVES results without the hosts that are too massive to fit the SAGA host criteria, as described in §7.1. The overall normalization of the ELVES histogram is larger (i.e. more satellites per host) than that of SAGA, similar to the findings of Figure 7, and this is especially the case with the red, quenched population. The SAGA-selected ELVES hosts have, on average,  $1.38 \pm 0.26$  satellites per host in this luminosity range with NUV- $g > 3$

while SAGA hosts only have  $0.47 \pm 0.11$ . The ELVES hosts have, on average,  $1.62 \pm 0.28$  satellites per host in this luminosity range with NUV- $g < 3$  while the SAGA hosts have  $1.15 \pm 0.18$ . Combining these, the ELVES hosts have  $\sim 1.5$  more satellites per host in this luminosity range with most of these satellites being UV-optically red. This difference is about the same as seen in Table 3. We do not expect the numbers to be exactly the same since no correction has been made for the fact that not all satellites have GALEX coverage. Note that also no correction has been made for the fact that some ELVES hosts are only surveyed out to a projected 150 kpc nor for any unconfirmed ELVES satellites in this magnitude range, although there are not many (cf. Figure 5).

The fact that the blue population for ELVES is not smaller than that of SAGA indicates that the visual classification is not simply erroneously classifying dwarfs as early-type that actually do have significant H $\alpha$  emission.

This discrepancy reinforces the possibility that SAGA is missing some number of quenched, LSB satellites, although, as before, it is conceivable that some of this can be explained by subtle differences in the host sample (e.g. large-scale environment). This might be explored with the full, 100-host sample from SAGA.



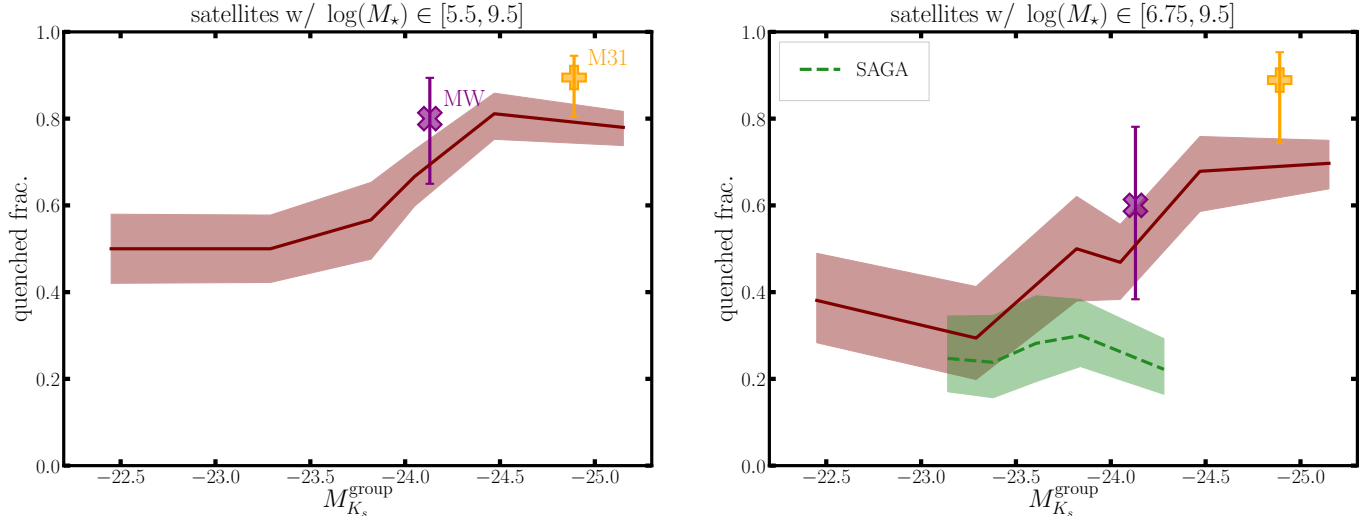
**Figure 11.** The quenched fraction as a function of satellite stellar mass. The maroon lines show the ELVES results under various restrictions. The left panel uses the morphology to classify ELVES satellites as star-forming or quenched and the presence of  $H\alpha$  emission for the SAGA satellites. The right panel uses a cut in color-magnitude space to classify satellites as star-forming or quenched for both ELVES and SAGA. For ELVES, the quenched fraction rises to roughly 80 – 90% for  $M_\star \lesssim 10^6 M_\odot$ , quite similar to the results for the Local Group (MW & M31) from [Wetzel et al. \(2015\)](#), while the SAGA quenched fractions are much lower. The errorbars and shaded regions show Bayesian confidence regions for the binomial proportion parameter. In the left panel, the thin dotted extensions to the SAGA points show the correction for incompleteness in the spectroscopic follow-up, assuming all candidates are quenched. This incompleteness is also accounted for in the right panel, with the color being used to classify candidates as star-forming or quenched.

Figure 11 shows the quenched fraction as a function of satellite stellar mass. In the left panel, morphology is used to classify ELVES satellites as quenched or star-forming, and the presence of  $H\alpha$  is used for the SAGA satellites ([Mao et al. 2021](#)). In the right panel, a cut in color-magnitude space is used to classify both ELVES and SAGA satellites. The line we use to divide quenched/early-type from star-forming/late-type is  $g-i = -0.067 \times M_V - 0.23$ . In [Carlsten et al. \(2021b\)](#), we found this line to cleanly separate early- from late-type dwarfs. Encouragingly, [Font et al. \(2021b\)](#) also found that this line did a good job of separating star-forming from quenched satellites in the ARTEMIS simulations. The photometry we use for the SAGA satellites is again from our own Sérsic fits using DECaLS data, which is therefore quite comparable to ELVES photometry since  $\sim 3/4$  of ELVES hosts use DECaLS for photometry (see Table 1). Additionally, we have argued above that the CFHT photometry (which the other  $\sim 1/4$  uses) is quite comparable to DECaLS without the need for a filter conversion.

Whether using morphology or a cut in color-magnitude space, the quenched fraction for ELVES satellites rises to  $\sim 85\%$  for  $M_\star < 10^6 M_\odot$  and is consistent with the results for LG satellites from [Wetzel et al. \(2015\)](#). This is the case regardless of whether only confirmed satellites are included, confirmed and possible satellites,

only satellites within  $r_{\text{proj}} < 150$  kpc, or only satellites of lower mass hosts that would satisfy the SAGA selection criteria (see §7.1 above). The inner satellites do show slightly higher quenched fractions, while the satellites of the less massive hosts show slightly lower fractions, but the differences are not great. In all cases, the ELVES quenched fraction is significantly higher than that of SAGA. In both panels, we include the uncertainty in the SAGA results due to incomplete spectroscopic follow-up. In the left panel, the thin dashed lines show the upper limit if *all* unconfirmed satellites are quenched (but still taking into account their probability of being a satellite as calculated by SAGA). The upper limit of this uncertainty does reach the ELVES results. Thus it is possible that this difference would be resolved with complete spectroscopic follow-up in SAGA, but it would require *every* new confirmed satellite to be quenched. In the right panel, the candidate satellites without spectra are classed as quenched or star-forming using their colors like all other dwarfs in that panel. The fact that the points do not reach the ELVES trend means that it is unreasonable to expect each of these candidates to be quenched as many are quite blue.

While we have shown that the difference between SAGA and ELVES satellites remains if we remove the ELVES hosts more massive than those selected in SAGA, it is possible that different distributions



**Figure 12.** The quenched fraction as a function of host mass. The satellite morphology is used to classify satellites as quenched or star-forming for the ELVES satellites. The two panels differ on the range of satellite stellar mass included. Individual results for the MW and M31 are shown. The right panel also shows the results for the SAGA Survey from (Mao et al. 2021).

of host masses skew the comparison. Thus, in Figure 12, we show the quenched fractions directly as a function of host mass (as proxied by  $K$ -band luminosity). The panels differ in the range of satellite stellar mass included in the quenched fraction calculation. The right panel includes satellites more massive than  $\log(M_*/M_\odot) > 6.75$ , corresponding to the SAGA luminosity limit of  $M_r = -12.3$  mag assuming  $M_*/L_r \approx 1$  which is appropriate for a  $g - r \sim 0.45$  dwarf (Into & Portinari 2013) which is about the average color in ELVES. In both cases, there is a noticeable trend of higher quenched fractions for more massive hosts, a result that makes intuitive sense and has been observed for higher mass satellites in SDSS (Wetzel et al. 2013; Wang et al. 2014).

The SAGA results include the incompleteness correction from Mao et al. (2021). For the satellites with redshifts, the star-forming status is determined by the presence of  $H\alpha$  while the color is used for candidates without redshifts. The SAGA results do not show a strong trend of increasing quenched fraction with higher mass host<sup>21</sup> and are always lower than the ELVES trend, particularly for the higher mass hosts, similar to the results of Figure 11.

Interestingly, even the lowest mass ELVES hosts ( $M_{K_s} > -23$  mag,  $M_* \lesssim 10^{10} M_\odot$ ) appear to be quenching their satellites quite efficiently. The current picture of ram pressure stripping is that it is due to the presence of an accretion shock-heated hot gas halo (e.g. Birn-

boim & Dekel 2003; Kereš et al. 2009; Gatto et al. 2013) around the host. Lower mass hosts ( $M_{\text{halo}} \lesssim 10^{11} M_\odot$ ) are not expected to form hot gas halos (Correa et al. 2018), so it is not completely clear what the quenching mechanism may be or whether ram pressure stripping is enough to explain the  $\sim 50\%$  quenched fractions. Along this vein, recent observations have indicated that satellites of even Large Magellanic Cloud (LMC)-mass centrals can be quenched (Carlin et al. 2019; Garling et al. 2020).

In summary, in this section, we investigated the star formation properties of the ELVES satellite systems, particularly looking at how many of the satellites are actively forming stars versus how many are quenched. Since ELVES is only a photometric survey, we can only gauge whether a satellite is quenched from its morphology and color. However, we show that this morphology-based quenching classification is closely corroborated by UV-optical color (Figure 10). Assuming this quenched classification is physical, we show that the quenched fraction of satellites in ELVES systems closely matches that of the LG with a majority of low-mass satellites being quenched (Figure 11). In Figure 12, we show that the quenched fraction increases with higher mass hosts, again with the MW and M31 being characteristic for hosts of their masses. We also compare with the results of the SAGA Survey (Geha et al. 2017; Mao et al. 2021). We show that, in general, the SAGA satellites without  $H\alpha$  emission have similar UV-optical colors to the early-type ELVES satellites, but there are significantly more early-type satellites in ELVES. This causes the inferred quenched fractions for SAGA to be much lower than in the LG or ELVES. The dearth of red, early-type satel-

<sup>21</sup> We note that a weak trend is seen if the incompleteness correction is not applied.

lites in SAGA even though ELVES hosts of the same mass (Figure 12) have plenty is suggestive of incompleteness in SAGA. We have shown that this discrepancy remains even when the SAGA results are corrected for incomplete spectroscopic follow-up, likely indicating incompleteness at the catalog level. This also explains the results in the previous two sections which showed lower average satellite abundance in SAGA, particularly in the inner regions of the satellite systems where satellites will likely be lower surface brightness, on average, and more easily missed.

## 8. CONCLUSIONS

This paper presents the Exploration of Local Volume Satellites (ELVES) Survey. The main scientific goal of ELVES is to provide a robust and statistical sample of well-surveyed satellite systems that can illuminate many aspects of small-scale structure formation and galaxy evolution. In particular, ELVES surveyed the satellites of a nearly *volume-limited* sample of massive, MW-like galaxies in the Local Volume. Hosts are selected via simply a cut in distance and  $K_s$  luminosity (cf. §2), facilitating easy, and direct, comparison with simulations. While most hosts are roughly MW-like in mass (cf. Figure 2), ELVES includes hosts both more and less massive than the MW, allowing insight into how host properties can affect satellite dwarf evolution.

The ELVES results include a satellite census for 30 of the 31 hosts in the volume-limited sample. Five of the satellite catalogs come from searches done by other groups in the literature while 25 systems are surveyed here in a consistent manner (cf. Table 1). This work subsumes and extends our previous surveys presented in Carlsten et al. (2020a, 2021c). For all hosts that we survey, we use the specialized low surface brightness dwarf detection algorithm presented in Carlsten et al. (2020a) to detect candidate dwarf satellites via integrated light. Through extensive tests with injected artificial galaxies, we have verified that the ELVES satellite catalogs are complete to  $M_V \sim -9$  mag and  $\mu_{0,V} \sim 26.5$  mag arcsec $^{-2}$  (cf. Figure 4). ELVES more than quadruples the number of satellite systems that have been surveyed to such low luminosity and surface brightness, opening the door to many different analyses on dwarf satellites (e.g. Carlsten et al. 2021b,a). While some hosts are only surveyed out to 150 projected kpc ( $\sim R_{\text{vir}}/2$  for MW-mass hosts), the majority are surveyed out to 300 kpc ( $\sim R_{\text{vir}}$ ).

Confirming that candidate satellites found in deep wide-field imaging surveys are actual satellites of a host is difficult as it requires a distance measurement to the candidate and is arguably the main complication ham-

pering previous satellite survey work. To deal with this, ELVES makes heavy use of surface brightness fluctuation (SBF) measurements as an efficient way to determine distances to LV dwarfs with ground based data (e.g. Carlsten et al. 2019b; Greco et al. 2020). The  $\sim 15\%$  distance accuracy achievable with SBF can, in most cases, determine whether a satellite candidate is a real satellite or a background contaminant. However, our previous work has found that  $\sim 15 - 20\%$  of satellites confirmed via SBF are ‘near-field’ dwarfs that are within  $\sim 1$  Mpc of the host but outside of the virial radius (Carlsten et al. 2021c). This should be kept in mind when analyzing ELVES satellites lists.

In total, we report 552 satellite candidates across the 25 surveyed hosts. Our surveys compare very favorably to previous surveys of the same hosts with ELVES almost always uncovering new, faint candidates. 251 of these candidates are confirmed via distance measurement with 136 of these being SBF distances. 196 are rejected via a distance measurement indicating they are in the background with almost all of these being SBF-based. This leaves 105 ‘unconfirmed/possible’ satellites that do not yet have a conclusive distance constraint. Based on the luminosities and surface brightness of these candidates, we estimate the probability that each is a satellite so they can be easily accounted for in future analyses. Combining with the 5 previously surveyed systems from the literature, there is a total of 338 confirmed dwarf satellites with well-understood completeness. For all ELVES-detected satellites and many of the literature satellites, we provide consistent Sérsic photometry, representing an important reference sample for studies of dwarf structure and evolution (e.g. Carlsten et al. 2021b).

Below, we list science highlights from the ELVES survey thus far, both in this paper and in the previous ones in this series:

- Carlsten et al. (2021c) performed in-depth comparisons between the observed satellite luminosity functions (LFs) of LV hosts and simulated LFs from modern cosmological simulations. That work found that popular stellar-to-halo-mass relations (SHMR) (e.g. Garrison-Kimmel et al. 2017) combined with the simulations could naturally reproduce the observed satellite abundances and host-to-host scatter. That work also highlighted the potential for the full ELVES sample to actually *fit* for the SHMR and thus constrain galaxy formation simulations.
- Carlsten et al. (2020b) similarly compared observed satellite systems with simulated systems fo-

cusing on the radial distribution of satellites. They found the systems observed by that point (only 12 of the full ELVES sample) were significantly more concentrated than the simulations. In §7.2, we briefly revisited this with the full ELVES sample and found that many of the Carlsten et al. (2020b) host sample were among the most centrally concentrated of all of ELVES. This suggests the results of Carlsten et al. (2020b) could indeed be due to its limited sample size, but an in-depth comparison with simulations with the full ELVES sample is warranted.

- Carlsten et al. (2021b) used most of the final ELVES sample to study the detailed structure of LV dwarf galaxies. That work found that early-type and late-type dwarfs had very similar sizes at fixed mass, indicating that the quenching and transformation process of a late-type into an early-type involves only mild, if any, structural change and likely is as simple as removing the gas from the dwarf. With that said, there were mild differences in the intrinsic (i.e. 3D) structure between early- and late-type dwarfs. That work provided a robust quantification of the mass-size relation in this low-mass regime, an important benchmark for simulations to try to recover and also useful in predicting dwarf search yields from future observational projects.
- Carlsten et al. (2021a) investigated the nuclear star clusters and globular clusters (GCs) of ELVES dwarfs and compared with those of dwarfs in the Virgo Cluster. They found that dwarfs in the less dense LV environments were less likely to be nucleated, had lower mass nuclei, and had fewer GCs at fixed dwarf mass than dwarfs in Virgo. This correspondence in environmental dependence of both nuclei and GCs strengthens the case that nuclei form from coalescing GCs in this mass range (e.g. Neumayer et al. 2020) and shows that GC formation and/or survival is strongly dependent on the large-scale environment that the host galaxy forms in (Peng et al. 2008).
- In §7.3 of this work, we explore the star formation properties of ELVES satellites. Since ELVES is only a photometric survey, we use galaxy morphology (early- vs. late-type) as the primary indicator of whether a satellite is star-forming or quenched. We show that this distinction is strongly corroborated by UV-optical color (Figure 10) with early-type satellites having quite red UV-optical colors, similar to those of satellites in the SAGA Survey

(Mao et al. 2021) that show no H $\alpha$  emission. We show that ELVES satellites are strongly quenched ( $\sim 90\%$ ) at low masses ( $M_\star \lesssim 10^6 M_\odot$ ), similar to the known situation in the Local Group (Figure 11). In this way, the required rapid quenching timescales needed to reproduce the Local Group results hold up for other hosts in the LV. In Figure 12, we show that the quenched fractions are higher for higher mass ELVES hosts but do not appear to get lower than  $\sim 50\%$  for even the lowest mass ( $M_\star \lesssim 10^{10} M_\odot$ ) hosts.

- Throughout this paper, we perform many comparisons with the SAGA Survey (Geha et al. 2017; Mao et al. 2021), a complementary spectroscopic survey of many nearby satellite systems. SAGA is sensitive to only the bright ( $M_V \lesssim -12$  mag) satellites but will eventually survey more hosts (100) than is possible in the LV. Overall, we show that the ELVES results indicate higher satellite abundance than SAGA for hosts of the same mass and a much steeper average LF. This is particularly the case for lower luminosity ( $M_V \gtrsim -15$  mag) satellites (Figure 7) and the inner regions of satellite systems (Figure 9). ELVES hosts have on average  $\sim 1.5$  satellites per host more than SAGA hosts. Similarly, ELVES hosts exhibit a significant population of red, early-type satellites that are much rarer in the SAGA results (Figure 10), causing SAGA to infer lower quenched fractions than are found in ELVES (Figure 11). At least some part of this difference is likely caused by incompleteness in the SAGA satellite lists, particularly in the DECaLS targeting catalogs used. Incompleteness in only the spectroscopic follow-up, which is modelled within SAGA, is not enough to explain this discrepancy. However, it is also possible that host-to-host scatter is contributing some of the discrepancy. The full 100-host SAGA sample will be important in quantifying this and exploring whether this might be caused by some physical differences in the hosts (e.g. different large scale environments, Neuzil et al. 2020).

The field of dwarf satellite research has a bright future with the next-generation observational facilities coming online in the upcoming decade. Vera Rubin Observatory’s Legacy Survey of Space and Time and the Roman Space Telescope will allow for searches and, even more importantly, distance measurements of classical-mass (e.g.  $M_\star > 10^5 M_\odot$ ) satellites out to 20-30 Mpc (Greco et al. 2020), pushing beyond the statistics of ELVES and what is possible in the LV. Additionally

both facilities will allow for dwarf searches in the LV to extend into the ultra-faint regime (Mutlu-Pakdil et al. 2021b), opening up a window into another, very interesting regime of dwarf galaxy evolution. These facilities will also allow for a complete census of low-mass dwarfs in the field (i.e. non-satellite dwarfs) in the LV which, even with SBF, is infeasible to obtain with current facilities. This will, in turn, allow for much more in-depth studies on dwarf galaxy evolution and the effects that massive hosts have on their dwarf satellite retinue.

#### ACKNOWLEDGEMENTS

We thank Yao-Yuan Mao and Marla Geha for helpful discussions regarding the SAGA Survey results. Support for this work was provided by NASA through Hubble Fellowship grant #51386.01 awarded to R.L.B. by the Space Telescope Science Institute, which is operated by the Association of Universities for Research in Astronomy, Inc., for NASA, under contract NAS 5-26555. J.P.G. is supported by an NSF Astronomy and Astrophysics Postdoctoral Fellowship under award AST-1801921. J.E.G. is partially supported by the National Science Foundation grant AST-1713828. S.G.C. acknowledges support by the National Science Foundation Graduate Research Fellowship Program under Grant No. #DGE-1656466. S.D. is supported by NASA through Hubble Fellowship grant HST-HF2-51454.001-A awarded by the Space Telescope Science Institute, which is operated by the Association of Universities for Research in Astronomy, Incorporated, under NASA contract NAS5-26555.

Based on observations obtained with MegaPrime/MegaCam, a joint project of CFHT and CEA/IRFU, at the Canada-France-Hawaii Telescope (CFHT) which is operated by the National Research Council (NRC) of Canada, the Institut National des Science de l'Univers of the Centre National de la Recherche Scientifique (CNRS) of France, and the University of Hawaii. This research was made possible through the use of the AAVSO Photometric All-Sky Survey (APASS) (Henden & Munari 2014), funded by the Robert Martin Ayers Sciences Fund and NSF AST-1412587

This research has made use of the NASA/IPAC Extragalactic Database (NED), which is operated by the Jet Propulsion Laboratory, California Institute of Technology, under contract with the National Aeronautics and Space Administration.

This research has made use of the SIMBAD database, operated at CDS, Strasbourg, France (Wenger et al. 2000).

The Legacy Surveys consist of three individual and complementary projects: the Dark Energy Camera

Legacy Survey (DECaLS; Proposal ID #2014B-0404; PIs: David Schlegel and Arjun Dey), the Beijing-Arizona Sky Survey (BASS; NOAO Prop. ID #2015A-0801; PIs: Zhou Xu and Xiaohui Fan), and the Mayall z-band Legacy Survey (MzLS; Prop. ID #2016A-0453; PI: Arjun Dey). DECaLS, BASS and MzLS together include data obtained, respectively, at the Blanco telescope, Cerro Tololo Inter-American Observatory, NSF's NOIRLab; the Bok telescope, Steward Observatory, University of Arizona; and the Mayall telescope, Kitt Peak National Observatory, NOIRLab. The Legacy Surveys project is honored to be permitted to conduct astronomical research on Iolkam Du'ag (Kitt Peak), a mountain with particular significance to the Tohono O'odham Nation.

NOIRLab is operated by the Association of Universities for Research in Astronomy (AURA) under a cooperative agreement with the National Science Foundation.

This project used data obtained with the Dark Energy Camera (DECam), which was constructed by the Dark Energy Survey (DES) collaboration. Funding for the DES Projects has been provided by the U.S. Department of Energy, the U.S. National Science Foundation, the Ministry of Science and Education of Spain, the Science and Technology Facilities Council of the United Kingdom, the Higher Education Funding Council for England, the National Center for Supercomputing Applications at the University of Illinois at Urbana-Champaign, the Kavli Institute of Cosmological Physics at the University of Chicago, Center for Cosmology and Astro-Particle Physics at the Ohio State University, the Mitchell Institute for Fundamental Physics and Astronomy at Texas A&M University, Financiadora de Estudos e Projetos, Fundacao Carlos Chagas Filho de Amparo, Financiadora de Estudos e Projetos, Fundacao Carlos Chagas Filho de Amparo a Pesquisa do Estado do Rio de Janeiro, Conselho Nacional de Desenvolvimento Cientifico e Tecnologico and the Ministerio da Ciencia, Tecnologia e Inovacao, the Deutsche Forschungsgemeinschaft and the Collaborating Institutions in the Dark Energy Survey. The Collaborating Institutions are Argonne National Laboratory, the University of California at Santa Cruz, the University of Cambridge, Centro de Investigaciones Energeticas, Medioambientales y Tecnologicas-Madrid, the University of Chicago, University College London, the DES-Brazil Consortium, the University of Edinburgh, the Eidgenossische Technische Hochschule (ETH) Zurich, Fermi National Accelerator Laboratory, the University of Illinois at Urbana-Champaign, the Institut de Ciencies de l'Espai (IEEC/CSIC), the Institut de Fisica d'Altes Energies, Lawrence Berkeley National Labora-

tory, the Ludwig Maximilians Universitat Munchen and the associated Excellence Cluster Universe, the University of Michigan, NSF’s NOIRLab, the University of Nottingham, the Ohio State University, the University of Pennsylvania, the University of Portsmouth, SLAC National Accelerator Laboratory, Stanford University, the University of Sussex, and Texas A&M University.

BASS is a key project of the Telescope Access Program (TAP), which has been funded by the National Astronomical Observatories of China, the Chinese Academy of Sciences (the Strategic Priority Research Program “The Emergence of Cosmological Structures” Grant # XDB09000000), and the Special Fund for Astronomy from the Ministry of Finance. The BASS is also supported by the External Cooperation Program of Chinese Academy of Sciences (Grant # 114A11KYSB20160057), and Chinese National Natural Science Foundation (Grant # 11433005).

The Legacy Survey team makes use of data products from the Near-Earth Object Wide-field Infrared Survey Explorer (NEOWISE), which is a project of the Jet Propulsion Laboratory/California Institute of Technology. NEOWISE is funded by the National Aeronautics and Space Administration.

The Legacy Surveys imaging of the DESI footprint is supported by the Director, Office of Science, Office of High Energy Physics of the U.S. Department of Energy under Contract No. DE-AC02-05CH1123, by the National Energy Research Scientific Computing Center, a DOE Office of Science User Facility under the same contract; and by the U.S. National Science Foundation, Division of Astronomical Sciences under Contract No. AST-0950945 to NOAO.

The Hyper Suprime-Cam (HSC) collaboration includes the astronomical communities of Japan and Taiwan, and Princeton University. The HSC instrumentation and software were developed by the National Astronomical Observatory of Japan (NAOJ), the Kavli Institute for the Physics and Mathematics of the Universe (Kavli IPMU), the University of Tokyo, the High Energy Accelerator Research Organization (KEK), the Academia Sinica Institute for Astronomy and Astrophysics in Taiwan (ASIAA), and Princeton University. Funding was contributed by the FIRST program from the Japanese Cabinet Office, the Ministry of Education, Culture, Sports, Science and Technology (MEXT), the Japan Society for the Promotion of Science (JSPS), Japan Science and Technology Agency (JST), the Toray Science Foundation, NAOJ, Kavli IPMU, KEK, ASIAA, and Princeton University.

This paper makes use of software developed for Vera C. Rubin Observatory. We thank the Rubin Observatory for making their code available as free software at <http://pipelines.lsst.io/>.

This paper is based on data collected at the Subaru Telescope and retrieved from the HSC data archive system, which is operated by the Subaru Telescope and Astronomy Data Center (ADC) at NAOJ. Data analysis was in part carried out with the cooperation of Center for Computational Astrophysics (CfCA), NAOJ. We are honored and grateful for the opportunity of observing the Universe from Maunakea, which has the cultural, historical and natural significance in Hawaii.

*Software:* `astropy` (Astropy Collaboration et al. 2018; Bradley et al. 2020), `sep` (Barbary 2016), `imfit` (Erwin 2015), `SWarp` (Bertin 2010), `Scamp` (Bertin 2006), `SExtractor` (Bertin & Arnouts 1996), `astrometry.net` (Lang et al. 2010)

## REFERENCES

- Abolfathi, B., Aguado, D. S., Aguilar, G., et al. 2018, *ApJS*, 235, 42
- Aihara, H., Arimoto, N., Armstrong, R., et al. 2018, *PASJ*, 70, S4
- Aihara, H., AlSayyad, Y., Ando, M., et al. 2019, *PASJ*, 71, 114
- Akhlaghi, M., & Ichikawa, T. 2015, *ApJS*, 220, 1
- Akins, H. B., Christensen, C. R., Brooks, A. M., et al. 2021, *ApJ*, 909, 139
- Anand, G. S., Rizzi, L., Tully, R. B., et al. 2021, arXiv e-prints, arXiv:2104.02649
- Applebaum, E., Brooks, A. M., Christensen, C. R., et al. 2020, arXiv e-prints, arXiv:2008.11207
- Astropy Collaboration, Price-Whelan, A. M., Sipőcz, B. M., et al. 2018, *AJ*, 156, 123
- Barbary, K. 2016, *JOSS*, 1, 58
- Beaton, R. L., Bono, G., Braga, V. F., et al. 2018, *SSRv*, 214, 113
- Beaton, R. L., Seibert, M., Hatt, D., et al. 2019, *ApJ*, 885, 141
- Bennet, P., Sand, D. J., Crnojević, D., et al. 2019, arXiv e-prints, arXiv:1906.03230
- . 2020, *ApJL*, 893, L9
- . 2017, *ApJ*, 850, 109

- Bertin, E. 2006, in *Astronomical Society of the Pacific Conference Series*, Vol. 351, *Astronomical Data Analysis Software and Systems XV*, ed. C. Gabriel, C. Arviset, D. Ponz, & S. Enrique, 112
- Bertin, E. 2010, *SWarp: Resampling and Co-adding FITS Images Together*, *Astrophysics Source Code Library*, , ascl:1010.068
- Bertin, E., & Arnouts, S. 1996, *A&AS*, 117, 393
- Birnboim, Y., & Dekel, A. 2003, *MNRAS*, 345, 349
- Bland-Hawthorn, J., & Gerhard, O. 2016, *ARA&A*, 54, 529
- Blanton, M. R., Kazin, E., Muna, D., Weaver, B. A., & Price-Whelan, A. 2011, *AJ*, 142, 31
- Bosch, J., Armstrong, R., Bickerton, S., et al. 2018, *PASJ*, 70, S5
- Boselli, A., Boissier, S., Cortese, L., & Gavazzi, G. 2008, *ApJ*, 674, 742
- Boylan-Kolchin, M., Bullock, J. S., & Kaplinghat, M. 2011, *MNRAS*, 415, L40
- . 2012, *MNRAS*, 422, 1203
- Bradley, L., Sipőcz, B., Robitaille, T., et al. 2020, *astropy/photutils: 1.0.0, v1.0.0*, Zenodo, doi:10.5281/zenodo.4044744
- Brooks, A. M., Kuhlen, M., Zolotov, A., & Hooper, D. 2013, *ApJ*, 765, 22
- Brooks, A. M., & Zolotov, A. 2014, *ApJ*, 786, 87
- Bullock, J. S., & Boylan-Kolchin, M. 2017, *ARA&A*, 55, 343
- Byun, W., Sheen, Y.-K., Park, H. S., et al. 2020, *ApJ*, 891, 18
- Cantiello, M., Blakeslee, J. P., Ferrarese, L., et al. 2018, *ApJ*, 856, 126
- Carlin, J. L., Sand, D. J., Price, P., et al. 2016, *ApJL*, 828, L5
- Carlin, J. L., Garling, C. T., Peter, A. H. G., et al. 2019, *arXiv e-prints*, arXiv:1906.08260
- Carlin, J. L., Mutlu-Pakdil, B., Crnojević, D., et al. 2021, *ApJ*, 909, 211
- Carlsten, S. G., Beaton, R. L., Greco, J. P., & Greene, J. E. 2019a, *ApJL*, 878, L16
- . 2019b, *ApJ*, 879, 13
- Carlsten, S. G., Greco, J. P., Beaton, R. L., & Greene, J. E. 2020a, *ApJ*, 891, 144
- Carlsten, S. G., Greene, J. E., Beaton, R. L., & Greco, J. P. 2021a, *arXiv e-prints*, arXiv:2105.03440
- Carlsten, S. G., Greene, J. E., Greco, J. P., Beaton, R. L., & Kado-Fong, E. 2021b, *arXiv e-prints*, arXiv:2105.03435
- Carlsten, S. G., Greene, J. E., Peter, A. H. G., Beaton, R. L., & Greco, J. P. 2021c, *ApJ*, 908, 109
- Carlsten, S. G., Greene, J. E., Peter, A. H. G., Greco, J. P., & Beaton, R. L. 2020b, *ApJ*, 902, 124
- Carlsten, S. G., Strauss, M. A., Lupton, R. H., Meyers, J. E., & Miyazaki, S. 2018, *MNRAS*, 479, 1491
- Chambers, K. C., Magnier, E. A., Metcalfe, N., et al. 2016, *ArXiv e-prints*, arXiv:1612.05560
- Chiboucas, K., Jacobs, B. A., Tully, R. B., & Karachentsev, I. D. 2013, *AJ*, 146, 126
- Chiboucas, K., Karachentsev, I. D., & Tully, R. B. 2009, *AJ*, 137, 3009
- Choi, J., Dotter, A., Conroy, C., et al. 2016, *ApJ*, 823, 102
- Cohen, Y., van Dokkum, P., Danieli, S., et al. 2018, *ApJ*, 868, 96
- Cook, D. O., Dale, D. A., Johnson, B. D., et al. 2014a, *MNRAS*, 445, 881
- . 2014b, *MNRAS*, 445, 899
- Correa, C. A., Schaye, J., Wyithe, J. S. B., et al. 2018, *MNRAS*, 473, 538
- Crnojević, D., Sand, D. J., Caldwell, N., et al. 2014, *ApJ*, 795, L35
- Crnojević, D., Sand, D. J., Spekkens, K., et al. 2016, *ApJ*, 823, 19
- Crnojević, D., Sand, D. J., Bennet, P., et al. 2019, *ApJ*, 872, 80
- Dalcanton, J. J., Spergel, D. N., Gunn, J. E., Schmidt, M., & Schneider, D. P. 1997, *AJ*, 114, 635
- Dalcanton, J. J., Williams, B. F., Seth, A. C., et al. 2009, *ApJS*, 183, 67
- Danieli, S., & van Dokkum, P. 2019, *ApJ*, 875, 155
- Danieli, S., van Dokkum, P., & Conroy, C. 2018, *ApJ*, 856, 69
- Danieli, S., van Dokkum, P., Merritt, A., et al. 2017, *ApJ*, 837, 136
- Danieli, S., Lokhorst, D., Zhang, J., et al. 2020, *ApJ*, 894, 119
- Davis, A. B., Nierenberg, A. M., Peter, A. H. G., et al. 2021, *MNRAS*, 500, 3854
- de Vaucouleurs, G., de Vaucouleurs, A., Corwin, Herold G., J., et al. 1991, *Third Reference Catalogue of Bright Galaxies*
- Dey, A., Schlegel, D. J., Lang, D., et al. 2019, *AJ*, 157, 168
- Drlica-Wagner, A., Bechtol, K., Mau, S., et al. 2020, *ApJ*, 893, 47
- Drlica-Wagner, A., Carlin, J. L., Nidever, D. L., et al. 2021, *ApJS*, 256, 2
- Egenthaler, P., Puzia, T. H., Taylor, M. A., et al. 2018, *ApJ*, 855, 142
- Engler, C., Pillepich, A., Pasquali, A., et al. 2021, *arXiv e-prints*, arXiv:2101.12215
- Erwin, P. 2015, *ApJ*, 799, 226
- Ferrarese, L., Côté, P., Cuilland re, J.-C., et al. 2012, *ApJS*, 200, 4

- Ferrarese, L., Côté, P., Sánchez-Janssen, R., et al. 2016, *ApJ*, 824, 10
- Ferrarese, L., Côté, P., MacArthur, L. A., et al. 2020, *ApJ*, 890, 128
- Fillingham, S. P., Cooper, M. C., Wheeler, C., et al. 2015, *MNRAS*, 454, 2039
- Flewelling, H. A., Magnier, E. A., Chambers, K. C., et al. 2016, arXiv e-prints, arXiv:1612.05243
- Font, A. S., McCarthy, I. G., & Belokurov, V. 2021a, *MNRAS*, 505, 783
- Font, A. S., McCarthy, I. G., Belokurov, V., Brown, S. T., & Stafford, S. G. 2021b, arXiv e-prints, arXiv:2109.06215
- Font, A. S., McCarthy, I. G., Poole-Mckenzie, R., et al. 2020, *MNRAS*, 498, 1765
- Gaia Collaboration, Brown, A. G. A., Vallenari, A., et al. 2018, *A&A*, 616, A1
- Garling, C. T., Peter, A. H. G., Kochanek, C. S., Sand, D. J., & Crnojević, D. 2020, *MNRAS*, 492, 1713
- . 2021, arXiv e-prints, arXiv:2105.01082
- Garrison-Kimmel, S., Boylan-Kolchin, M., Bullock, J. S., & Lee, K. 2014, *MNRAS*, 438, 2578
- Garrison-Kimmel, S., Bullock, J. S., Boylan-Kolchin, M., & Bardwell, E. 2017, *MNRAS*, 464, 3108
- Garrison-Kimmel, S., Hopkins, P. F., Wetzel, A., et al. 2019a, *MNRAS*, 487, 1380
- Garrison-Kimmel, S., Wetzel, A., Hopkins, P. F., et al. 2019b, *MNRAS*, 489, 4574
- Gatto, A., Fraternali, F., Read, J. I., et al. 2013, *MNRAS*, 433, 2749
- Geha, M., Wechsler, R. H., Mao, Y.-Y., et al. 2017, *ApJ*, 847, 4
- Gil de Paz, A., Boissier, S., Madore, B. F., et al. 2007, *ApJS*, 173, 185
- Grcevich, J., & Putman, M. E. 2009, *ApJ*, 696, 385
- Grebel, E. K., Gallagher, John S., I., & Harbeck, D. 2003, *AJ*, 125, 1926
- Greco, J. P., Goulding, A. D., Greene, J. E., et al. 2018a, *ApJ*, 866, 112
- Greco, J. P., van Dokkum, P., Danieli, S., Carlsten, S. G., & Conroy, C. 2020, arXiv e-prints, arXiv:2004.07273
- Greco, J. P., Greene, J. E., Strauss, M. A., et al. 2018b, *ApJ*, 857, 104
- Gunn, J. E., & Gott, J. Richard, I. 1972, *ApJ*, 176, 1
- Habas, R., Marleau, F. R., Duc, P.-A., et al. 2020, *MNRAS*, 491, 1901
- Haigh, C., Chamba, N., Venhola, A., et al. 2021, *A&A*, 645, A107
- Hausammann, L., Revaz, Y., & Jablonka, P. 2019, *A&A*, 624, A11
- Haynes, M. P., Giovanelli, R., Kent, B. R., et al. 2018, *ApJ*, 861, 49
- Henden, A., & Munari, U. 2014, *Contributions of the Astronomical Observatory Skalnaté Pleso*, 43, 518
- Hernández-Toledo, H. M., Méndez-Hernández, H., Aceves, H., & Olguín, L. 2011, *AJ*, 141, 74
- Huchra, J. P., Macri, L. M., Masters, K. L., et al. 2012, *ApJS*, 199, 26
- Humphreys, E. M. L., Reid, M. J., Moran, J. M., Greenhill, L. J., & Argon, A. L. 2013, *ApJ*, 775, 13
- Ibata, R. A., Lewis, G. F., Conn, A. R., et al. 2013, *Nature*, 493, 62
- Into, T., & Portinari, L. 2013, *MNRAS*, 430, 2715
- Irwin, J. A., Hoffman, G. L., Spekkens, K., et al. 2009, *ApJ*, 692, 1447
- Jacobs, B. A., Rizzi, L., Tully, R. B., et al. 2009, *AJ*, 138, 332
- Javanmardi, B., Martinez-Delgado, D., Kroupa, P., et al. 2016, *A&A*, 588, A89
- Jennings, Z. G., Romanowsky, A. J., Brodie, J. P., et al. 2015, *ApJL*, 812, L10
- Jensen, J. B., Tonry, J. L., Barris, B. J., et al. 2003, *ApJ*, 583, 712
- Jerjen, H., Rekola, R., Takalo, L., Coleman, M., & Valtonen, M. 2001, *A&A*, 380, 90
- Jiang, F., Dekel, A., Freundlich, J., et al. 2020, arXiv e-prints, arXiv:2005.05974
- Kado-Fong, E., Greene, J. E., Huang, S., et al. 2020, *ApJ*, 900, 163
- Karachentsev, I. D., & Kaisina, E. I. 2013, *AJ*, 146, 46
- Karachentsev, I. D., Karachentseva, V. E., Huchtmeier, W. K., & Makarov, D. I. 2004, *AJ*, 127, 2031
- Karachentsev, I. D., & Kudrya, Y. N. 2014, *AJ*, 148, 50
- Karachentsev, I. D., Makarov, D. I., & Kaisina, E. I. 2013, *AJ*, 145, 101
- Karachentsev, I. D., Makarova, L. N., Brent Tully, R., et al. 2020, *A&A*, 643, A124
- Karachentsev, I. D., Tully, R. B., Makarova, L. N., Makarov, D. I., & Rizzi, L. 2015a, *ApJ*, 805, 144
- Karachentsev, I. D., Tully, R. B., Wu, P.-F., Shaya, E. J., & Dolphin, A. E. 2014, *ApJ*, 782, 4
- Karachentsev, I. D., Dolphin, A., Tully, R. B., et al. 2006, *AJ*, 131, 1361
- Karachentsev, I. D., Tully, R. B., Dolphin, A., et al. 2007, *AJ*, 133, 504
- Karachentsev, I. D., Riepe, P., Zilch, T., et al. 2015b, *Astrophysical Bulletin*, 70, 379
- Karachentseva, V. E. 1968, *Communications of the Byurakan Astrophysical Observatory*, 39, 61

- Karunakaran, A., Spekkens, K., Bennet, P., et al. 2020a, *AJ*, 159, 37
- Karunakaran, A., Spekkens, K., Zaritsky, D., et al. 2020b, arXiv e-prints, arXiv:2005.14202
- Karunakaran, A., Spekkens, K., Oman, K. A., et al. 2021, arXiv e-prints, arXiv:2105.09321
- Kazantzidis, S., Lokas, E. L., Callegari, S., Mayer, L., & Moustakas, L. A. 2011, *ApJ*, 726, 98
- Kazantzidis, S., Lokas, E. L., & Mayer, L. 2013, *ApJL*, 764, L29
- Kennicutt, Robert C., J., Lee, J. C., Funes, J. G., et al. 2008, *ApJS*, 178, 247
- Kereš, D., Katz, N., Fardal, M., Davé, R., & Weinberg, D. H. 2009, *MNRAS*, 395, 160
- Kim, E., Kim, M., Hwang, N., et al. 2011, *MNRAS*, 412, 1881
- Kim, S. Y., Peter, A. H. G., & Hargis, J. R. 2018, *PhRvL*, 121, 211302
- Kim, Y. J., & Lee, M. G. 2021, arXiv e-prints, arXiv:2110.02522
- Klypin, A., Kravtsov, A. V., Valenzuela, O., & Prada, F. 1999, *ApJ*, 522, 82
- Kondapally, R., Russell, G. A., Conselice, C. J., & Penny, S. J. 2018, *MNRAS*, 481, 1759
- Koposov, S., Belokurov, V., Evans, N. W., et al. 2008, *ApJ*, 686, 279
- Kormendy, J., Fisher, D. B., Cornell, M. E., & Bender, R. 2009, *ApJS*, 182, 216
- Kourkchi, E., & Tully, R. B. 2017, *ApJ*, 843, 16
- La Marca, A., Peletier, R., Iodice, E., et al. 2021, arXiv e-prints, arXiv:2112.00711
- Lang, D., Hogg, D. W., Mierle, K., Blanton, M., & Roweis, S. 2010, *AJ*, 139, 1782
- Lang, D., Hogg, D. W., & Mykytyn, D. 2016, *The Tractor: Probabilistic astronomical source detection and measurement*, , ascl:1604.008
- Laureijs, R., Amiaux, J., Arduini, S., et al. 2011, arXiv e-prints, arXiv:1110.3193
- Lee, J. C., Gil de Paz, A., Tremonti, C., et al. 2009, *ApJ*, 706, 599
- Lee, J. C., Gil de Paz, A., Kennicutt, Robert C., J., et al. 2011, *ApJS*, 192, 6
- Lee, M. G., & Jang, I. S. 2013, *ApJ*, 773, 13
- Leroy, A. K., Sandstrom, K. M., Lang, D., et al. 2019, *ApJS*, 244, 24
- Libeskind, N. I., Carlesi, E., Grand, R. J. J., et al. 2020, *MNRAS*, 498, 2968
- Licquia, T. C., Newman, J. A., & Brinchmann, J. 2015, *ApJ*, 809, 96
- Lim, S. H., Mo, H. J., Lu, Y., Wang, H., & Yang, X. 2017, *MNRAS*, 470, 2982
- Mao, Y.-Y., Geha, M., Wechsler, R. H., et al. 2021, *ApJ*, 907, 85
- Martin, D. C., Fanson, J., Schiminovich, D., et al. 2005, *ApJL*, 619, L1
- Mateo, M. L. 1998, *ARA&A*, 36, 435
- Mayer, L., Mastropietro, C., Wadsley, J., Stadel, J., & Moore, B. 2006, *MNRAS*, 369, 1021
- McConnachie, A. W. 2012, *AJ*, 144, 4
- McGaugh, S. S., & Schombert, J. M. 2014, *AJ*, 148, 77
- McQuinn, K. B. W., Skillman, E. D., Dolphin, A. E., Berg, D., & Kennicutt, R. 2016a, *ApJ*, 826, 21
- . 2016b, *AJ*, 152, 144
- . 2017, *AJ*, 154, 51
- Melchior, P., Moolekamp, F., Jerdee, M., et al. 2018, *Astronomy and Computing*, 24, 129
- Merritt, A., van Dokkum, P., & Abraham, R. 2014, *ApJL*, 787, L37
- Meyer, M. J., Zwaan, M. A., Webster, R. L., et al. 2004, *MNRAS*, 350, 1195
- Moore, B., Ghigna, S., Governato, F., et al. 1999, *ApJ*, 524, L19
- Morrissey, P., Conrow, T., Barlow, T. A., et al. 2007, *ApJS*, 173, 682
- Muñoz, R. P., Eigenthaler, P., Puzia, T. H., et al. 2015, *ApJL*, 813, L15
- Müller, O., Ibata, R., Rejkuba, M., & Posti, L. 2019a, *A&A*, 629, L2
- Müller, O., & Jerjen, H. 2020, *A&A*, 644, A91
- Müller, O., Jerjen, H., & Binggeli, B. 2015, *A&A*, 583, A79
- . 2017a, *A&A*, 597, A7
- . 2018a, *A&A*, 615, A105
- Müller, O., Pawlowski, M. S., Jerjen, H., & Lelli, F. 2018b, *Science*, 359, 534
- Müller, O., Rejkuba, M., & Jerjen, H. 2018c, *A&A*, 615, A96
- Müller, O., Rejkuba, M., Pawlowski, M. S., et al. 2019b, *A&A*, 629, A18
- Müller, O., Scalera, R., Binggeli, B., & Jerjen, H. 2017b, *A&A*, 602, A119
- Müller, O., Fahrion, K., Rejkuba, M., et al. 2021, *A&A*, 645, A92
- Munshi, F., Brooks, A., Applebaum, E., et al. 2021, arXiv e-prints, arXiv:2101.05822
- Mutlu-Pakdil, B., Sand, D. J., Crnojević, D., et al. 2021a, arXiv e-prints, arXiv:2108.09312
- . 2021b, *ApJ*, 918, 88
- Nadler, E. O., Mao, Y.-Y., Green, G. M., & Wechsler, R. H. 2019, *ApJ*, 873, 34

- Nadler, E. O., Wechsler, R. H., Bechtol, K., et al. 2020, *ApJ*, 893, 48
- Nelson, D., Springel, V., Pillepich, A., et al. 2019, *Computational Astrophysics and Cosmology*, 6, 2
- Neumayer, N., Seth, A., & Böker, T. 2020, *A&A Rv*, 28, 4
- Neuzil, M. K., Mansfield, P., & Kravtsov, A. V. 2020, *MNRAS*, 494, 2600
- Nierenberg, A. M., Treu, T., Menci, N., et al. 2016, *MNRAS*, 462, 4473
- Park, H. S., Moon, D.-S., Zaritsky, D., et al. 2019, *ApJ*, 885, 88
- . 2017, *ApJ*, 848, 19
- Pawlowski, M. S. 2018, *Modern Physics Letters A*, 33, 1830004
- Pawlowski, M. S., & Kroupa, P. 2020, *MNRAS*, 491, 3042
- Pawlowski, M. S., Pflamm-Altenburg, J., & Kroupa, P. 2012, *MNRAS*, 423, 1109
- Peacock, M. B., Strader, J., Romanowsky, A. J., & Brodie, J. P. 2015, *ApJ*, 800, 13
- Peng, E. W., Jordán, A., Côté, P., et al. 2008, *ApJ*, 681, 197
- Pillepich, A., Nelson, D., Hernquist, L., et al. 2018, *MNRAS*, 475, 648
- Prole, D. J., van der Burg, R. F. J., Hilker, M., & Spitler, L. R. 2021, *MNRAS*, 500, 2049
- Putman, M. E., Zheng, Y., Price-Whelan, A. M., et al. 2021, *ApJ*, 913, 53
- Radburn-Smith, D. J., de Jong, R. S., Seth, A. C., et al. 2011, *ApJS*, 195, 18
- Radburn-Smith, D. J., de Jong, R. S., Streich, D., et al. 2014, *ApJ*, 780, 105
- Rekola, R., Jerjen, H., & Flynn, C. 2005, *A&A*, 437, 823
- Rines, K., Geller, M. J., Kurtz, M. J., & Diaferio, A. 2003, *AJ*, 126, 2152
- Roberts, D. M., Nierenberg, A. M., & Peter, A. H. G. 2021, *MNRAS*, 502, 1205
- Robotham, A. S. G., Davies, L. J. M., Driver, S. P., et al. 2018, *MNRAS*, 476, 3137
- Sabbi, E., Calzetti, D., Ubeda, L., et al. 2018, *ApJS*, 235, 23
- Sales, L. V., Wang, W., White, S. D. M., & Navarro, J. F. 2013, *MNRAS*, 428, 573
- Samuel, J., Wetzel, A., Tollerud, E., et al. 2020, *MNRAS*, 491, 1471
- Sand, D. J., Crnojević, D., Strader, J., et al. 2014, *ApJ*, 793, L7
- Sawala, T., Frenk, C. S., Fattahi, A., et al. 2016, *MNRAS*, 457, 1931
- Schlafly, E. F., & Finkbeiner, D. P. 2011, *ApJ*, 737, 103
- Schlegel, D. J., Finkbeiner, D. P., & Davis, M. 1998, *ApJ*, 500, 525
- Sick, J., Courteau, S., Cuillard re, J.-C., et al. 2015, in *IAU Symposium*, Vol. 311, *Galaxy Masses as Constraints of Formation Models*, ed. M. Cappellari & S. Courteau, 82–85
- Simon, J. D. 2019, *ARA&A*, 57, 375
- Simpson, C. M., Grand, R. J. J., Gómez, F. A., et al. 2018, *MNRAS*, 478, 548
- Skrutskie, M. F., Cutri, R. M., Stiening, R., et al. 2006, *AJ*, 131, 1163
- Smercina, A., Bell, E. F., Price, P. A., et al. 2018, *ApJ*, 863, 152
- Smercina, A., Bell, E. F., Samuel, J., & D'Souza, R. 2021, *arXiv e-prints*, arXiv:2107.04591
- Smercina, A., Bell, E. F., Slater, C. T., et al. 2017, *ApJL*, 843, L6
- Spekkens, K., Urbancic, N., Mason, B. S., Willman, B., & Aguirre, J. E. 2014, *ApJL*, 795, L5
- Spencer, M., Loebman, S., & Yoachim, P. 2014, *ApJ*, 788, 146
- Spergel, D., Gehrels, N., Baltay, C., et al. 2015, *arXiv e-prints*, arXiv:1503.03757
- Stierwalt, S., Haynes, M. P., Giovanelli, R., et al. 2009, *AJ*, 138, 338
- Su, A. H., Salo, H., Janz, J., et al. 2021, *A&A*, 647, A100
- Tanaka, M., Chiba, M., Hayashi, K., et al. 2018, *ApJ*, 865, 125
- Tanaka, M., Chiba, M., & Komiyama, Y. 2017, *ApJ*, 842, 127
- Tanoglidis, D., Drlica-Wagner, A., Wei, K., et al. 2021, *ApJS*, 252, 18
- Tikhonov, N. A., Lebedev, V. S., & Galazutdinova, O. A. 2015, *Astronomy Letters*, 41, 239
- Toloba, E., Sand, D. J., Spekkens, K., et al. 2016, *ApJL*, 816, L5
- Tonry, J., & Schneider, D. P. 1988, *AJ*, 96, 807
- Tonry, J. L., Dressler, A., Blakeslee, J. P., et al. 2001, *ApJ*, 546, 681
- Trentham, N., & Tully, R. B. 2009, *MNRAS*, 398, 722
- Tully, R. B., Courtois, H. M., & Sorce, J. G. 2016, *AJ*, 152, 50
- Tully, R. B., Karachentsev, I. D., Rizzi, L., & Shaya, E. J. 2019, *Every Known Nearby Galaxy, HST Proposal*, ,
- van den Bosch, F. C., Ogiya, G., Hahn, O., & Burkert, A. 2018, *MNRAS*, 474, 3043
- Venhola, A., Peletier, R., Laurikainen, E., et al. 2018, *A&A*, 620, A165
- Venhola, A., Peletier, R. F., Salo, H., et al. 2021, *arXiv e-prints*, arXiv:2111.01855
- Wang, W., Sales, L. V., Henriques, B. M. B., & White, S. D. M. 2014, *MNRAS*, 442, 1363

- Wang, W., & White, S. D. M. 2012, MNRAS, 424, 2574
- Wang, W., Takada, M., Li, X., et al. 2021, MNRAS, 500, 3776
- Wenger, M., Ochsenein, F., Egret, D., et al. 2000, A&AS, 143, 9
- Wetzel, A. R., Hopkins, P. F., Kim, J.-h., et al. 2016, ApJL, 827, L23
- Wetzel, A. R., Tinker, J. L., Conroy, C., & van den Bosch, F. C. 2013, MNRAS, 432, 336
- Wetzel, A. R., Tollerud, E. J., & Weisz, D. R. 2015, ApJL, 808, L27
- Willmer, C. N. A. 2018, ApJS, 236, 47
- Wu, J. F., Peek, J. E. G., Tollerud, E. J., et al. 2021, arXiv e-prints, arXiv:2112.01542
- Wyder, T. K., Martin, D. C., Schiminovich, D., et al. 2007, ApJS, 173, 293
- Xi, C., Taylor, J. E., Massey, R. J., et al. 2018, MNRAS, 478, 5336
- Zaritsky, D., Donnerstein, R., Dey, A., et al. 2019, ApJS, 240, 1
- Zou, H., Zhou, X., Fan, X., et al. 2017, PASP, 129, 064101
- Zou, H., Zhang, T., Zhou, Z., et al. 2018, ApJS, 237, 37

**Table 4.** LV Galaxies not Included in Host List.

Name	Reason
M82	member in M81 group
NGC3184	Mean NED SN1a distance > 12 Mpc
NGC3351	member in Leo I group
NGC3368	member in Leo I group
NGC3377	member in Leo I group
NGC3384	member in Leo I group
NGC3412	member in Leo I group
NGC3489	member in Leo I group
NGC3593	member in Leo Triplet
NGC3628	member in Leo Triplet
NGC4490	TRGB distance of <a href="#">Sabbi et al. (2018)</a> yields $M_K > -22.1$
NGC4559	KT17 lists $M_K > -22.1$
NGC2835	KT17 lists $M_K > -22.1$
NGC5195	member of NGC5194 group
NGC1792	member of NGC1808 group
NGC4818	Mean NED distance > 12 Mpc
NGC6684	SBF distance of <a href="#">Tonry et al. (2001)</a> has distance > 12 Mpc

## APPENDIX

## A. GALAXIES NOT INCLUDED IN HOST LIST

Table 4 lists the massive LV galaxies that passed the initial cuts but were removed from the master host list either due to being secondaries in a group or a more precise distance estimate placing them outside the LV or below the  $M_K$  cut.

## B. INDIVIDUAL HOST AREA COVERAGE

Figure 13 shows the survey footprints and locations of candidate satellites for each individual host. The different sources of data used for candidate detection are shown. The candidate satellites are plotted in different styles depending on whether they are confirmed as satellites via distance measurement, rejected as background contaminants, or whether no distance constraint was possible. Only candidates with  $M_V < -9$  mag are shown and that fall within the coverage radii given in Table 1. The figure shows which hosts use the BASS part of DECaLS, as well as the two hosts (NGC 4258 and NGC 4631) that use DECaLS to extend the radial coverage of the CFHT/MegaCam survey.

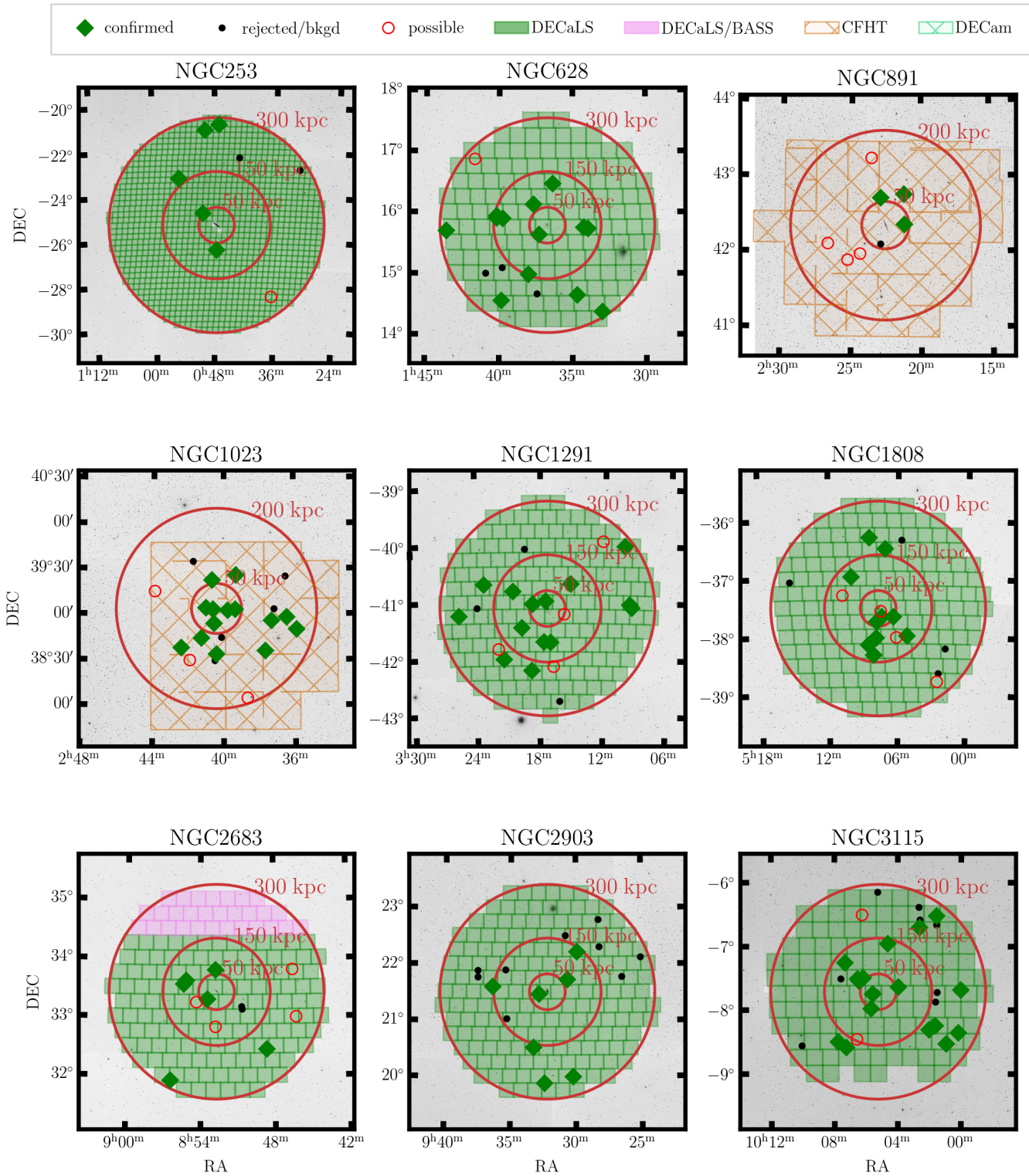
## C. INDIVIDUAL HOST COMPLETENESS RESULTS

Figure 14 shows the individual recovery fractions for all 25 hosts for which we do our own candidate satellite detection. The source of the imaging data is denoted in the upper left corner. The recovery fractions do not vary much between the hosts, with two main exceptions. First is that the DECaLS hosts that use the BASS portion of DECaLS have generally  $\sim 0.5$  mag worse surface brightness completeness. Second is NGC 891 which uses quite shallow CFHT/MegaCam imaging.

## D. COMPARISON TO PREVIOUS LV SATELLITE SEARCHES

In this section, we compare the ELVES satellite searches with previous searches of the same host in the literature. We only focus on the hosts new in this work here. [Carlsten et al. \(2020a\)](#) provided an exhaus-

tive comparison with previous searches for the hosts included there (NGC 1023, NGC 4258, NGC 4631, NGC4565, NGC 5194, M104), and we refer the reader to that discussion for comparison of those satellite surveys.



**Figure 13.** The individual survey footprints for the hosts surveyed in this work. Candidate satellites with  $M_V < -9$  mag are plotted in different ways to indicate whether they are confirmed as satellites via distance measurement, rejected as background contaminants, or whether no distance constraint is possible.

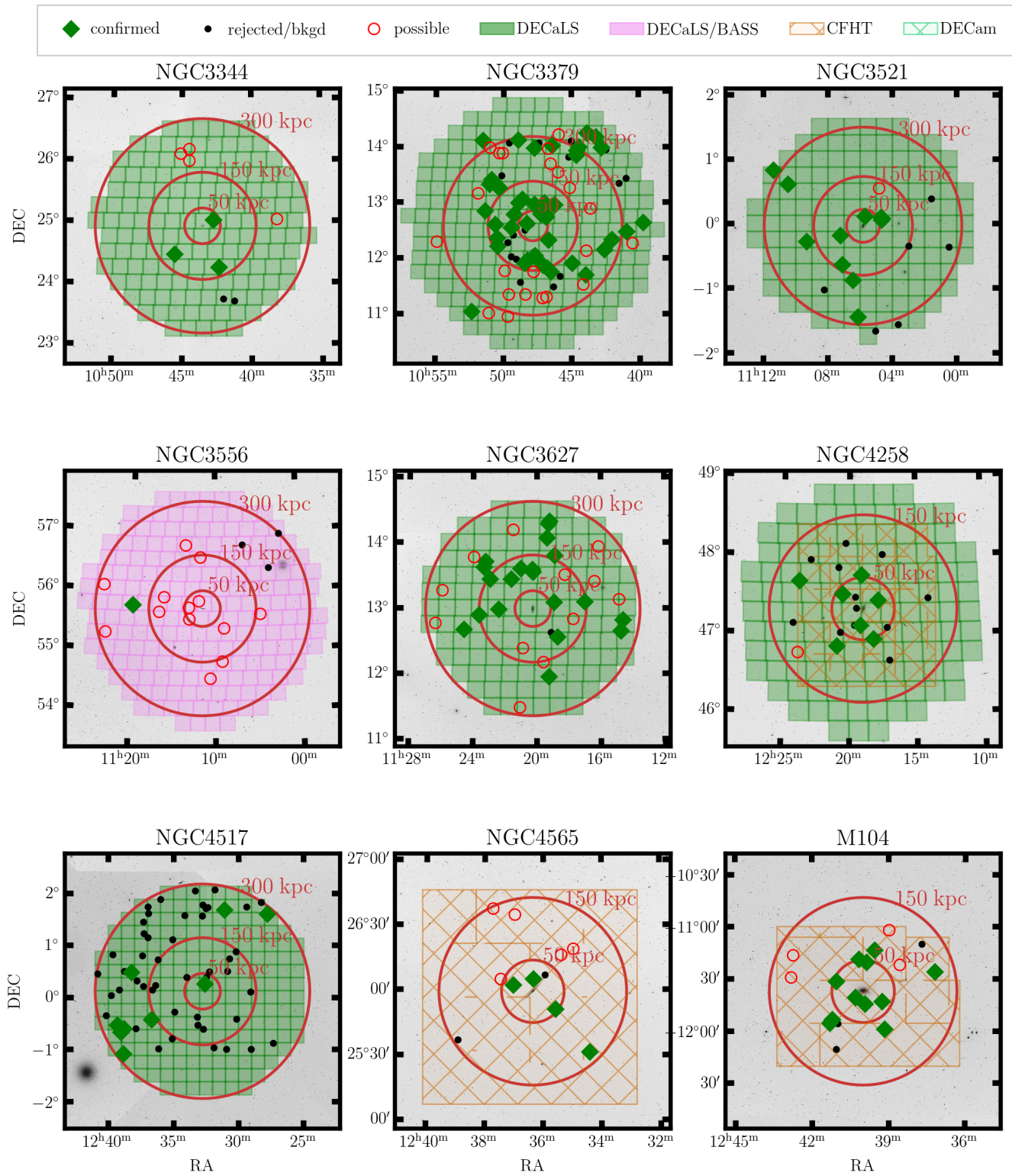


Figure 13.

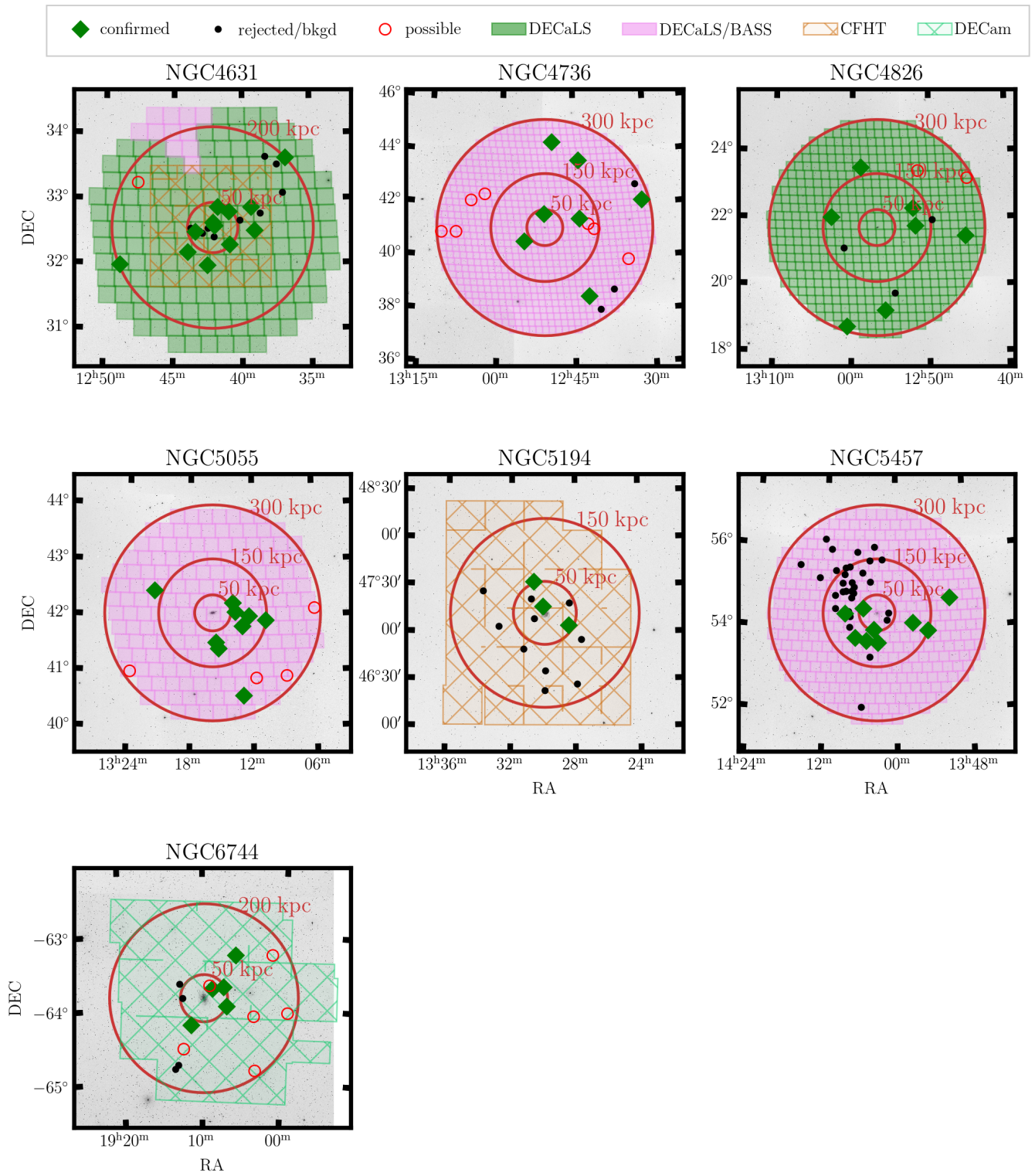
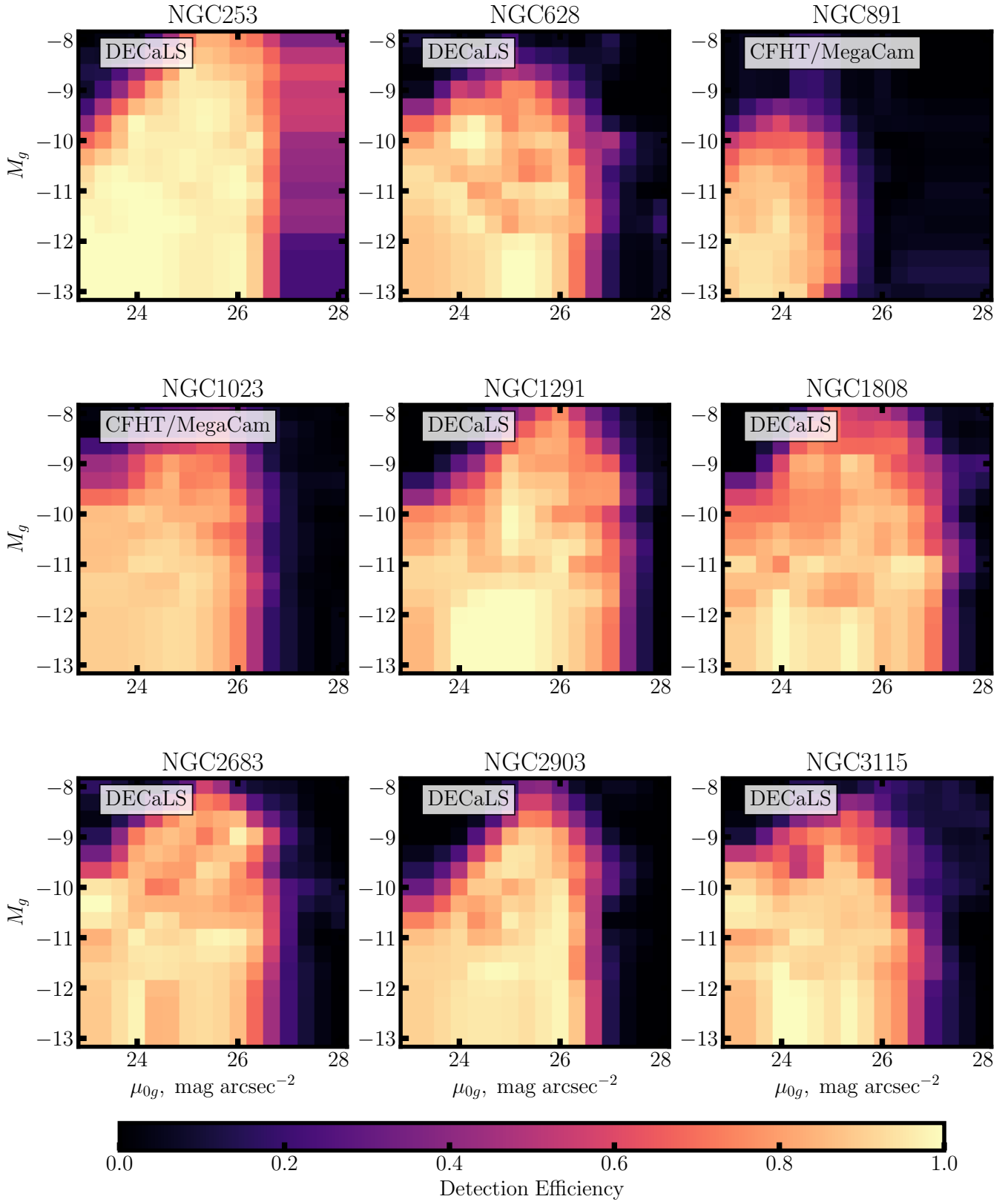


Figure 13.



**Figure 14.** Results of completeness tests for individual hosts. Artificial galaxies are injected into the images, and the recovery efficiency is measured as a function of total magnitude and central surface brightness.

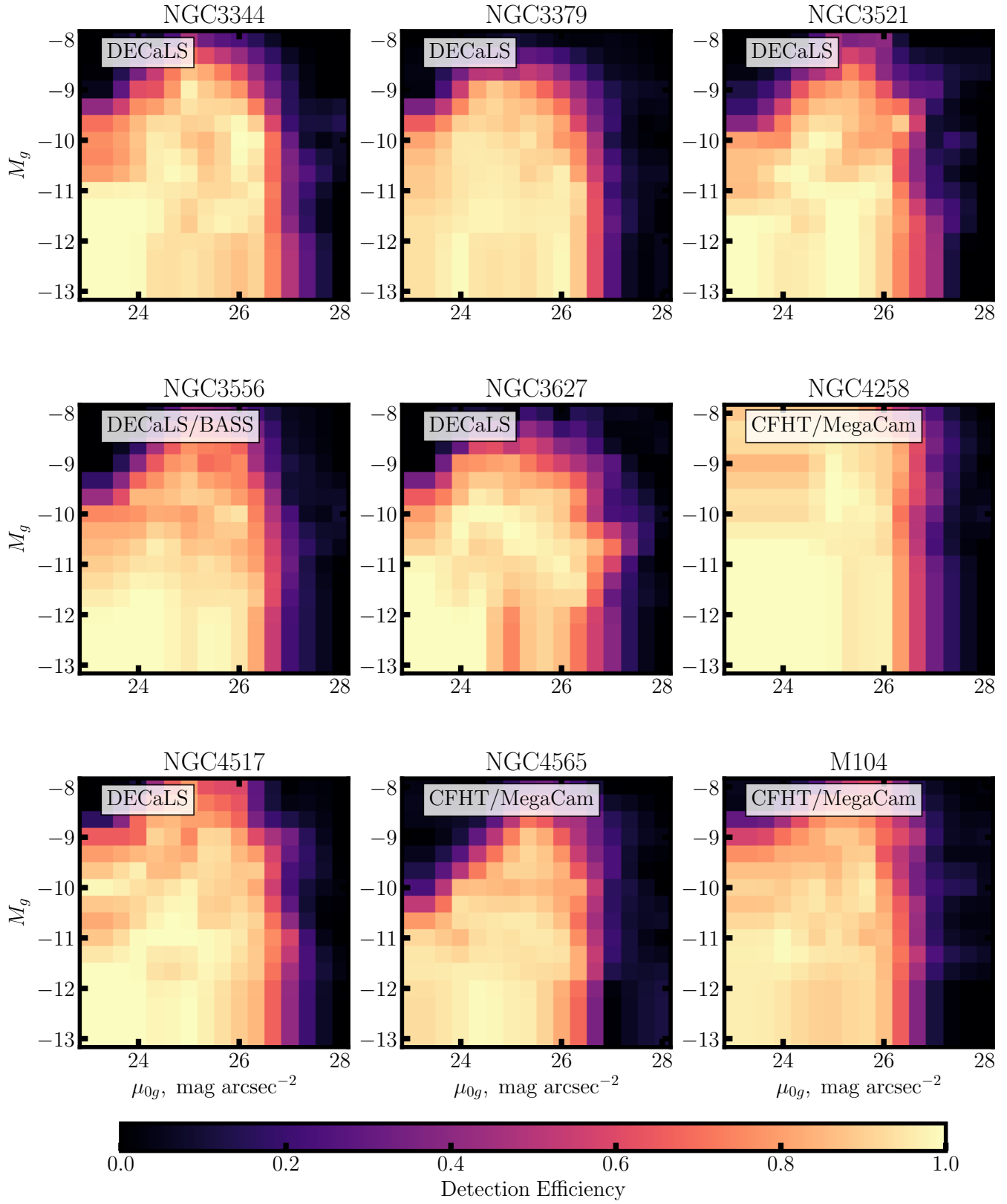


Figure 14.

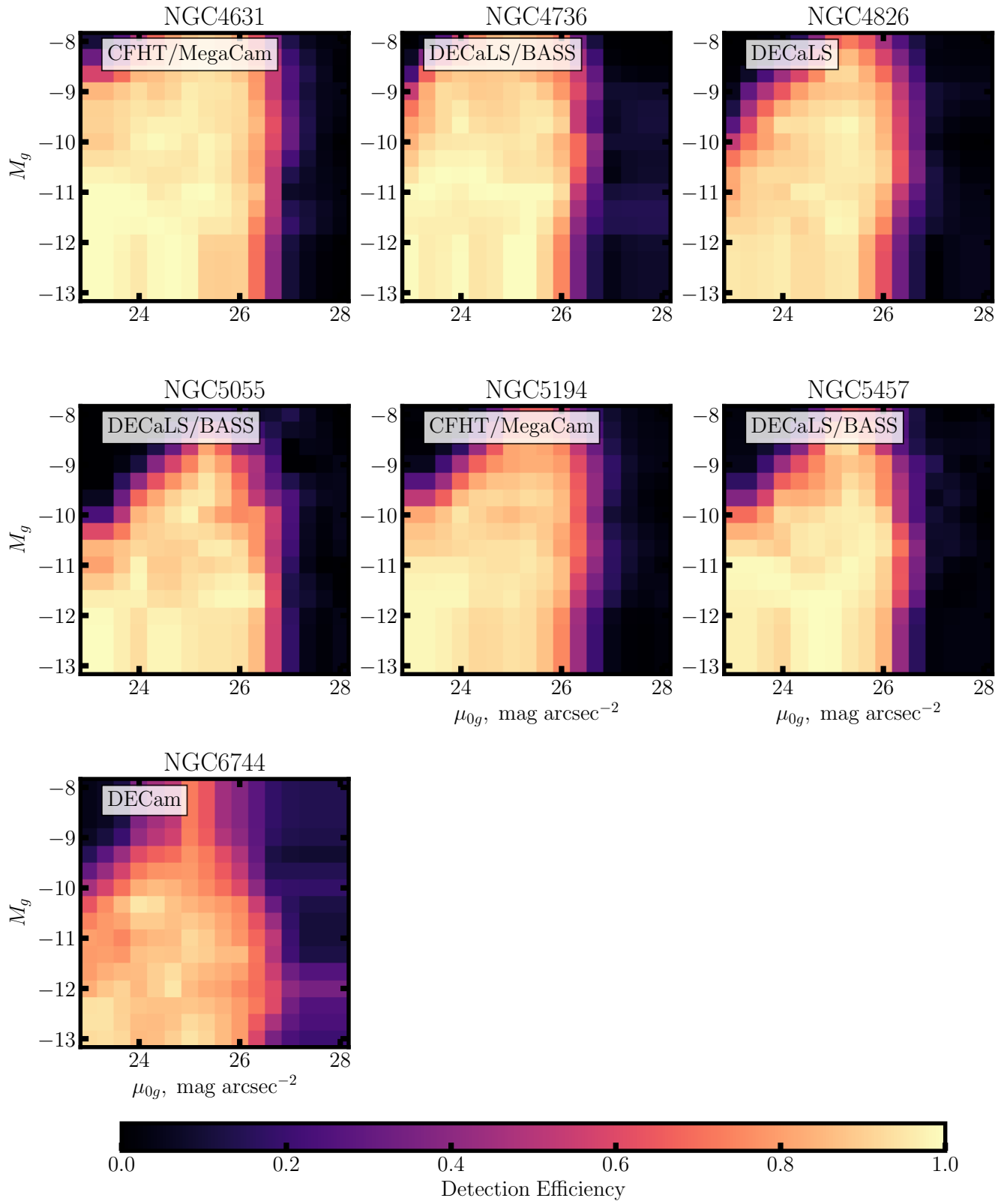


Figure 14.

**Table 5.** Comparison with the UNGC.

Name	Host	RA (deg)	DEC (deg)	Reason
ScuSR	NGC253	8.4658	-27.84	viz reject; tidal stream of a bkgd. gal
NGC628dwTBG	NGC628	23.2783	16.2514	viz reject; cirrus
NGC628dwB	NGC628	24.0967	15.9647	below ELVES luminosity limit
N1291-DW11	NGC1291	48.1842	-42.7983	not in DECaLS tract footprints
N1291-DW15	NGC1291	49.9071	-40.4214	not detected but bkgd. galaxy from bulge+disk morph.
N1291-DW14	NGC1291	51.2617	-40.3589	viz reject; bkgd. galaxy with spiral arms
dw1044+11	NGC3379	161.1362	11.2694	viz reject; tidal stream of a bkgd. gal
BST1047+1156	NGC3379	161.9325	11.9336	Below ELVES SB completeness
NGC3521dwTBG	NGC3521	166.8046	0.1875	Does not appear to be real; nothing seen in deep HSC imaging
LVJ1215+4732	NGC4258	183.9629	47.5489	In chip gap of CFHT/Megacam survey and known bkgd
M106edgeN4217	NGC4258	184.0521	47.1344	Tidal stream/fluff of bkgd. galaxy
NGC4288	NGC4258	185.1588	46.2917	Outside of CFHT/Megacam footprint; clear bkgd. morphology
CVnHI	NGC4258	185.1808	46.2092	Not seen in deep optical images
SUCD1	M104	190.0129	-11.6678	ELVES is not sensitive to UCDs
KKSG33	M104	190.0371	-12.3647	Outside of CFHT/Megacam footprint
NGC4656UV	NGC4631	191.0654	32.2833	TDG; not a distinct galaxy
NGC4485	NGC4736	187.63	41.7	rejected because TRGB
NGC4490	NGC4736	187.6517	41.6436	rejected because TRGB
UGC07678	NGC4736	188.0017	39.8319	rejected because redshift
PGC041749	NGC4736	188.4696	39.6258	rejected because redshift
UGC7719	NGC4736	188.5025	39.0194	rejected because redshift
UGC7751	NGC4736	188.7992	41.0608	rejected because redshift
NGC4618	NGC4736	190.3867	41.1508	rejected because TRGB
NGC4625	NGC4736	190.4696	41.2739	rejected because TRGB
dw1305+41	NGC4736	196.3708	41.89	Falls in star-mask but clear bkgd. morphology
dw1305+41	NGC5055	196.3708	41.89	Falls in star-mask but clear bkgd. morphology
NGC5055dwTBG2	NGC5055	198.7129	41.725	Viz reject; tidal stream of a bkgd. gal
GBT1355+5439	NGC5457	208.7108	54.6472	Nothing seen in deep optical images
PGC2448110	NGC5457	211.2408	53.6914	Just an HII region
PGC725719	NGC5236	200.7367	-29.7386	Distant edge-on disk galaxy?
dw1326-29	NGC5236	201.5167	-29.4044	SBF reject
dw1328-29	NGC5236	202.05	-29.4792	SBF reject
dw1329-32	NGC5236	202.4917	-32.4961	SBF reject
dw1330-32	NGC5236	202.725	-32.3058	SBF reject
dw1336-32	NGC5236	204.1375	-32.3014	Cirrus
dw1337-26	NGC5236	204.3042	-26.8028	Deep imaging shows just scattered light
NGC5253	NGC5236	204.9825	-31.64	TRGB indicates foreground

NOTE—Reasons why the UNGC entries that fall within the coverage radii of the ELVES hosts but are not in the ELVES catalogs are missed. The only cases where legitimate, likely satellite candidates are missed is where they fell just outside the survey tracts (while still being within the coverage radius). In many cases ELVES uses deeper imaging for targeting which revealed previously noted candidates to be clear background galaxies.

**UNGC (Karachentsev et al. 2013):** By far the current best reference for LV dwarfs is the Updated Nearby Galaxy Catalog of Karachentsev et al. (2013). This catalog is kept up-to-date with new dwarf searches and, thus, includes the objects from many of the individual host surveys we discuss below. We use a version of the UNGC from March, 2021. For each of the 25 hosts surveyed in ELVES, we go through the UNGC and find all objects that fall within the survey coverage radius of the host ( $r_{\text{cover}}$  from Table 1). All UNGC entries that fall within the covered radius are matched with ELVES candidate satellites, and those that do not have a match are listed in Table 5. Overall there are 245 UNGC objects that fall within the ELVES surveyed regions, with 37 not having a matching ELVES candidate<sup>22</sup>. For each of these, we provide a brief reason as to why it is not included in the ELVES satellite catalogs. These reasons are listed in Table 5. About  $\sim 1/2$  of the missing UNGC galaxies were detected in ELVES but rejected based on their morphology (none of these UNGC entries have an actual distance measurement). ELVES uses deeper targeting imaging than what was likely available in the original detection of these objects and reveals clear indicators of being in the background. These include bulge+disk morphology, spiral arms present in a small ( $r_e < 5''$ ) galaxy, or a tidal bridge connecting it to a nearby massive background galaxy. The only cases where a legitimate candidate satellite is missed is where the candidate is below the completeness limits of ELVES or it falls outside of the survey footprint (while still being within the coverage radius given in Table 1).

**NASA-Sloan Atlas (NSA; Blanton et al. 2011):** We additionally look for any galaxies with known redshifts in the NSA in the regions surrounding the ELVES hosts. No additional valid candidates are found that are not already included in the ELVES satellite lists.

**NGC 1291 (Byun et al. 2020):** We recover all the satellite candidates reported by Byun et al. (2020) that fall within 300 kpc projected of NGC 1291 except for three: Dw11, Dw15, and Dw14. The first falls just outside the footprints of the DECaLS tracts used in our search. The latter two had morphologies strongly indicating they are background. One is a distant edge-on disk galaxy with a clear bulge, and the other has a bar and spiral arms yet is quite small ( $r_e < 5''$ ). We note that our DECaLS/DES search recovers 6 candidates not included by Byun et al. (2020), including two we have rejected as background contaminants, one we have con-

firmed via SBF, and three that remain without distance confirmation.

**NGC 5457 (Javanmardi et al. 2016; Müller et al. 2017b; Bennet et al. 2017):** We recover all candidates detected around NGC 5457 by Javanmardi et al. (2016), Müller et al. (2017b), and Bennet et al. (2017) that are  $M_V < -9$  mag (i.e. within the ELVES completeness limit) except for three: dwC, dw26, and dw31. The first was detected by our algorithm but rejected in the visual inspection stage. Bennet et al. (2019) showed this galaxy is, indeed, a background contaminant. Dw26 was not detected by our algorithm as it is a relatively high-surface brightness background spiral (Bennet et al. 2017; Carlsten et al. 2019a). Dw31 was covered by a star-mask in our DECaLS search but was shown by Carlsten et al. (2019a) to be a background contaminant. Our DECaLS search produced many additional candidates not noted by these previous works. Admittedly, most are dwarfs in the background NGC 5485 group, but two have been confirmed as NGC 5457 satellites via SBF (one is  $M_V > -9$  mag and thus not in the ELVES list).

Finally, we mention that our DECaLS searches of NGC 4631 and NGC 4258 recover all confirmed satellites of those hosts found in the deeper CFHT/Megacam surveys of Carlsten et al. (2020a) with the single exception of dw1242p3237 around NGC 4631. However, this satellite is below the typical  $\mu_{0,V} \sim 26.5$  mag arcsec<sup>-2</sup> sensitivity of the DECaLS searches.

## E. CANDIDATE SATELLITE DISTANCE CONSTRAINTS

In Table 6, we present the distance constraints for the confirmed satellites. Candidate name, coordinates, host, and host distance are given along with the distance information used in the confirmation. SBF distance is given along with  $\pm 1, 2\sigma$  distance uncertainties, the S/N of the measurement, and the source of the data used (e.g. CFHT/MegaCam, HSC, etc.). Known redshifts or TRGB distances for dwarfs that have them are also listed, along with their source. Redshifts without a reference come from SIMBAD. Dwarfs marked by a <sup>†</sup> had some problem with the SBF measurement and are explained in more detail below.

Table 7 similarly presents the distance constraints for the rejected candidates. In this case, only the  $2\sigma$  lower bound to the SBF distance is given.

Table 8 lists the candidates who did not have a conclusive distance constraint. The source, if any, of an attempted SBF measurement is listed.

In the remaining part of this section, we discuss the few cases that are exceptions to the usual criteria for

<sup>22</sup> One UNGC galaxy appears twice, once as a “candidate satellite” of NGC 4736 and once of NGC 5055

confirming or rejecting candidate satellites. Some of these had problematic SBF measurements while some have distance information coming from sources other than the most common three methods used (redshift, TRGB, and SBF).

- dw1242p3231 from the NGC 4631 system has archival HST imaging in which it is unresolved, indicating that it is not at  $D = 7.4$  Mpc.
- dw1330p4708 from the NGC 5194 system similarly has archival HST coverage showing it is unresolved and, hence, background.
- dw1908m6343 from the NGC 6744 system had a high S/N SBF measurement but yielded far too small of a distance. This is a blue, very irregular dwarf which can bias the fluctuation too high since a Sérsic model is assumed in the SBF measurement. Considering the fact that the SBF amount is visually about the same as other, more regular blue satellites in this system and dw1908m6343 is quite near NGC 6744 in projection, this is very likely a satellite.
- dw0031m2246 from the NGC 253 system barely makes the  $\Delta cz < 275$  km/s cut but has a Tully-Fisher distance in NED indicating it is background.
- dw0933p2030 from the NGC 2903 system has an SDSS redshift with  $\Delta cz > 275$  km/s which appears to be extremely low S/N and erroneous upon visual inspection, and thus we trust the SBF distance result.
- dw1240p3800 and UGC7690 from the NGC 4736 system make the  $\Delta cz < 275$  km/s cut but both have Tully-Fisher distances in NED indicating background.
- dw1300p1843 from the NGC 4826 system has a SBF distance consistent with that of the host but only with  $S/N \sim 3$ . However, it has visually noticeable SBF that appears to be the same level as other satellites in this system. Additionally, its large  $r_e \sim 30''$  size indicates it is unlikely to be background (it is already an outlier to the mass-size relation). Thus, we consider it confirmed.
- dw1046p1259 from the NGC 3379 system has a very strong SBF signal but yields a slightly lower distance than its host. This dwarf is in a halo of scattered light from a nearby star which often biases the fluctuation measurement high (and thus

distance low) (Carlsten et al. 2021c). We consider this a confirmed satellite.

- dw1119p1404 from the NGC 3627 system has an SDSS redshift with  $\Delta cz = -303$  km/s which appears to be extremely low S/N and just noise upon visual inspection, and thus we trust the SBF distance result.
- dw1120p1337 from the NGC 3627 system is an actively disrupting nucleated dwarf (see, e.g., Jennings et al. 2015) and no distance measurement is required to confirm its satellite status.
- dw0316m4244 and dw0323m4105 from the NGC 1291 system were imaged with deeper Magellan imaging in order to measure SBF. However, the deeper imaging clearly revealed them to be tidal features of massive background galaxies, and we reject them without an SBF measurement.
- dw0852p3347 from the NGC 2683 system is tidally distorted by NGC 2683 and thus is a confirmed satellite without need for a distance measurement.
- dw1105p0006 from the NGC 3521 system is also tidally distorted by its host, removing any need for a distance measurement.
- UGCA337 (dw1312p4147) from the NGC 5055 system has an extremely strong SBF signal but the  $2\sigma$  distance upper bound is slightly closer than NGC 5055. It is slightly irregular which is biasing the SBF a little high. It has a redshift that makes the  $\Delta cz < 275$  km/s cut, and is almost certainly a satellite.
- dw1240m1140 from the M104 system shows a strong SBF signal that puts it in the foreground. However, this dwarf is located very close to M104 in projection, and the halo of M104 appears to be adding fluctuation power to the SBF measurement. Considering its dSph morphology, proximity to M104, and SBF, we include it in the ‘confirmed’ category.
- dw1241p3251 from the NGC 4631 system appears slightly foreground from the SBF measurement. However, this galaxy is not well fit by a Sérsic profile, and thus the distance is likely underestimated. This galaxy has a redshift consistent with NGC 4631 ( $\Delta cz \sim 60$  km/s) and is considered ‘confirmed’.
- dw1106p5644 from the NGC 3556 is not seen in deeper CFHT imaging, indicating it was just an

artifact in DECaLS. It is included in the ‘rejected’ category.

- dw1235p2606 from the NGC 4565 system is located directly in the middle of an HI warp on the northwest edge of the disk. [Radburn-Smith et al.](#)

(2014) used HST observations to show that this candidate consists of young ( $\sim 600$  Myr) stars that likely formed in-situ in the warp. Thus, this is not a dwarf satellite and is ‘rejected’.

**Table 6.** Confirmed dwarf satellite distance results

Name	RA (deg)	DEC (deg)	Host	$D_{\text{host}}$ (Mpc)	SBF Distance (Mpc)	SBF S/N	SBF Source	$v_{\text{rec}}$ (km/s)	$v_{\text{rec}}$ Source	$D_{\text{TRGB}}$ (Mpc)	$D_{\text{TRGB}}$ Source
NGC247	11.783	-20.757	NGC253	3.56	—	—	—	159	—	3.72	a
dw0047m2623	11.894	-26.390	NGC253	3.56	—	—	—	—	—	3.90	b
dw0049m2100	12.454	-21.017	NGC253	3.56	—	—	—	295	—	3.44	a
dw0050m2444	12.575	-24.737	NGC253	3.56	—	—	—	—	—	3.12	c
dw0055m2309	13.754	-23.169	NGC253	3.56	—	—	—	250	a	—	—
dw0132p1422	23.249	14.374	NGC628	9.77	—	—	—	669	—	—	—
dw0133p1543	23.484	15.731	NGC628	9.77	$9.18^{+0.98,2.04}_{-0.94,1.9}$	8.29	GEMINI	—	—	—	—
dw0134p1544	23.554	15.746	NGC628	9.77	$10.5^{+0.92,1.86}_{-0.86,1.74}$	9.63	GEMINI	—	—	—	—
dw0134p1438	23.674	14.644	NGC628	9.77	—	—	—	731	—	—	—
dw0136p1628	24.084	16.470	NGC628	9.77	$9.45^{+0.72,1.42}_{-0.74,1.57}$	22.76	GEMINI	—	—	—	—
dw0137p1537	24.324	15.633	NGC628	9.77	$10.12^{+1.87,3.97}_{-1.67,3.08}$	8.05	CFHT	—	—	—	—
dw0137p1607	24.416	16.132	NGC628	9.77	$9.05^{+1.26,2.79}_{-1.14,2.22}$	5.90	GEMINI	—	—	—	—
dw0138p1458	24.502	14.982	NGC628	9.77	$8.61^{+0.87,1.91}_{-0.74,1.36}$	6.34	GEMINI	738	—	—	—
UGC1171	24.937	15.899	NGC628	9.77	$10.13^{+1.28,2.92}_{-0.96,1.7}$	5.41	GEMINI	696	—	—	—
dw0139p1433	24.961	14.556	NGC628	9.77	$10.82^{+0.96,2.05}_{-0.8,1.5}$	8.04	GEMINI	—	—	—	—
dw0140p1556	25.040	15.939	NGC628	9.77	$11.78^{+1.49,3.31}_{-1.18,2.11}$	6.10	GEMINI	—	—	—	—
UGC1176	25.043	15.905	NGC628	9.77	—	—	—	632	—	—	—
dw0143p1541	25.901	15.694	NGC628	9.77	$8.64^{+0.71,1.48}_{-0.61,1.22}$	8.57	GEMINI	789	—	—	—
dw0221p4221	35.301	42.364	NGC891	9.12	$10.48^{+1.46,3.01}_{-1.38,2.67}$	10.57	CFHT	—	—	10.28	d
UGC1807	35.306	42.763	NGC891	9.12	—	—	—	630	—	—	—
dw0222p4242	35.730	42.712	NGC891	9.12	$10.28^{+1.57,3.46}_{-1.38,2.6}$	6.29	CFHT	—	—	—	—

NOTE—The names, coordinates, hosts, and distance results for the confirmed satellites. Dwarfs marked with a <sup>†</sup> are exceptions to the usual confirmation criteria. The full version of the table will be published in the online journal or will be provided upon request to the authors. SIMBAD is the source for  $v_{\text{rec}}$  unless otherwise noted. Other sources listed are: (a) Karachentsev et al. (2013)(b) Sand et al. (2014), (c) Toloba et al. (2016), (d) Müller et al. (2019a), (e) Meyer et al. (2004), (f) Irwin et al. (2009), (g) Cohen et al. (2018), (h) Sabbi et al. (2018), (i) Tully et al. (2016), (j) Haynes et al. (2018), (k) Karunakaran et al. (2020b), (l) Rines et al. (2003), (m) Smcercina et al. (2018), (n) Tikhonov et al. (2015), (o) Danieli et al. (2017), (p) Bennet et al. (2019), .

Table 7. Rejected background contaminants distance results

Name	RA (deg)	DEC (deg)	Host	$D_{\text{host}}$ (Mpc)	SBF Distance lower bound (Mpc)	SBF Source	$v_{\text{rec}}$ (km/s)	$v_{\text{rec}}$ Source	$D_{\text{TRGB}}$ (Mpc)	$D_{\text{TRGB}}$ Source
dw0031m2246	7.843	-22.766	NGC253	3.56	-	-	530	-	-	-
IC1574	10.766	-22.247	NGC253	3.56	-	-	360	-	4.92	a
dw0137p1439	24.355	14.661	NGC628	9.77	10.97	GEMINI	-	-	-	-
dw0139p1505	24.943	15.086	NGC628	9.77	10.32	GEMINI	-	-	-	-
dw0140p1459	25.221	14.999	NGC628	9.77	22.45	GEMINI	-	-	-	-
dw0222p4206	35.728	42.104	NGC891	9.12	9.4	CFHT	-	-	-	-
dw0236p3925	39.129	39.422	NGC1023	10.40	14.05	CFHT	-	-	-	-
dw0237p3903	39.289	39.061	NGC1023	10.40	13.14	CFHT	-	-	-	-
dw0240p3844	40.031	38.749	NGC1023	10.40	16.66	CFHT	-	-	-	-
dw0240p3829	40.123	38.493	NGC1023	10.40	21.61	CFHT	-	-	-	-
dw0241p3934	40.435	39.582	NGC1023	10.40	13.46	CFHT	-	-	-	-
dw0316m4244	49.032	-42.738	NGC1291	9.08	-	-	-	-	-	-
dw0319m4003	49.858	-40.063	NGC1291	9.08	9.67	MAGELLAN	-	-	-	-
dw0323m4105	50.977	-41.093	NGC1291	9.08	-	-	-	-	-	-
dw0501m3811	75.468	-38.196	NGC1808	9.29	20.67	GEMINI	-	-	-	-
dw0502m3837	75.611	-38.625	NGC1808	9.29	24.67	GEMINI	-	-	-	-
dw0505m3620	76.422	-36.335	NGC1808	9.29	13.13	MAGELLAN	-	-	-	-
dw0515m3703	78.846	-37.059	NGC1808	9.29	15.81	MAGELLAN	-	-	-	-
dw0850p3307	132.651	33.130	NGC2683	9.40	10.64	HSC	-	-	-	-
dw0850p3310	132.662	33.168	NGC2683	9.40	15.04	HSC	-	-	-	-
dw0925p2207	141.258	22.122	NGC2903	9.00	17.16	GEMINI	-	-	-	-

NOTE—The names, coordinates, hosts, and distance results for the rejected background contaminants. Objects marked with a † are exceptions to the usual rejection criteria. The full version of the table will be published in the online journal or will be provided upon request to the authors. SIMBAD is the source for  $v_{\text{rec}}$  unless otherwise noted. Other sources listed are: (a) Karachentsev et al. (2013), (b) Cohen et al. (2018), (c) Dalcanton et al. (2009), (d) Dalcanton et al. (1997).

## F. SBF IMAGE SIMULATIONS

In this section, we describe simple image simulations with SBF that we performed to investigate the confirmation and rejection criteria outlined in §5.3. For these simulations, we take tracts of very deep imaging data from two hosts:  $g/r$  CFHT/Megacam imaging for NGC 4258 and  $g/i$  Subaru/HSC imaging for NGC 3379. For each host, we simulate dwarfs both with and without SBF, representing actual satellites and background contaminants, respectively. We then attempt an SBF measurement and quantify how successful the measurement is in confirming or rejecting candidate satellites as a function of dwarf luminosity and surface brightness.

In particular, we simulate dwarfs with exponential profiles and colors of  $g - r = 0.45$  and  $g - i = 0.7$ . For dwarfs that are simulated with SBF, we give them the appropriate level of SBF given their color and host distance. Once the simulated dwarfs are injected into the imaging frames, we perform an SBF measurement in the usual way starting with fitting the dwarf with a Sérsic profile. We then record if the SBF measurement successfully produced a distance constraint for that dwarf. For dwarfs with SBF, this means an SBF measurement with  $S/N > 5$  and distance consistent with that of the host. For dwarfs without SBF, this means having a  $2\sigma$  distance lower bound beyond the host’s distance.

Figure 15 shows the results of these simulations. Both sides show the success rate of the SBF measurement as a function of luminosity (assuming the host’s distance) and surface brightness. The right panels are for the

dwarfs simulated with SBF and shows the fraction of them at each luminosity and surface brightness which yield SBF measurements with  $S/N > 5$  and distances consistent with the host. The left panels are for the dwarfs without SBF and show the fraction that are successfully constrained to be in the background. Note that in both cases the dwarfs with ‘unsuccessful’ SBF measurements are just those with too low  $S/N$ , and the dwarf would remain in the ‘unconfirmed/candidate’ category. The few cases where an artificial galaxy with SBF gets erroneously rejected to be background or vice versa are due to problems in the Sérsic fitting and/or masking that would be caught in the SBF process on real dwarfs.

Both confirming or rejected a dwarf via SBF are more successful at higher luminosity and surface brightness. Following the mass-size relation of Carlsten et al. (2021b), both measurements start to fail fainter than  $M_g \sim -9$  mag and  $\mu_{0,g} \sim 26$  mag arcsec<sup>-2</sup>. It appears that a background dwarf in this borderline parameter region is more likely to be successfully rejected than a real dwarf is to be confirmed. In other words, with imaging data to apply SBF of a given depth, it is possible to reject background contaminants using our criterion for dwarfs that are  $\sim 0.5 - 1$  mag fainter than what is possible for confirming a dwarf satellite. This difference stems from the specific threshold ( $S/N > 5$ ) we require in the SBF measurement. A lower threshold would make it easier to confirm a satellite while a higher threshold would exacerbate this difference. We discussed the rationale for this threshold in §5.3 and Carlsten et al. (2021c).

**Table 8.** Unconfirmed/possible candidate satellites.

Name	RA	DEC	Host	$D_{\text{host}}$	SBF attempt
	(deg)	(deg)		(Mpc)	
dw0036m2828	9.127	-28.470	NGC253	3.56	NONE
dw0141p1651	25.417	16.872	NGC628	9.77	GEMINI
dw0223p4314	35.892	43.240	NGC891	9.12	NONE
dw0224p4158	36.097	41.975	NGC891	9.12	NONE
dw0225p4153	36.319	41.892	NGC891	9.12	CFHT
dw0226p4206	36.669	42.111	NGC891	9.12	NONE
dw0238p3805	39.670	38.085	NGC1023	10.40	NONE
dw0241p3829	40.476	38.498	NGC1023	10.40	CFHT
dw0243p3915	40.979	39.256	NGC1023	10.40	CFHT
dw0312m3955	48.038	-39.918	NGC1291	9.08	MAGELLAN
dw0315m4112	48.942	-41.202	NGC1291	9.08	MAGELLAN
dw0316m4207	49.182	-42.128	NGC1291	9.08	MAGELLAN
dw0321m4149	50.485	-41.818	NGC1291	9.08	MAGELLAN
dw0502m3845	75.639	-38.765	NGC1808	9.29	GEMINI
dw0506m3800	76.535	-38.010	NGC1808	9.29	GEMINI
dw0507m3733	76.872	-37.554	NGC1808	9.29	NONE
dw0510m3717	77.710	-37.286	NGC1808	9.29	GEMINI
dw0846p3300	131.559	32.997	NGC2683	9.40	NONE
dw0846p3348	131.630	33.811	NGC2683	9.40	NONE
dw0852p3249	133.199	32.829	NGC2683	9.40	NONE
dw0854p3314	133.585	33.249	NGC2683	9.40	NONE

NOTE—The names, coordinates, hosts, and source for attempted SBF measurement for the unconfirmed/possible dwarf satellites. The full version of the table will be published in the online journal or will be provided upon request to the authors.

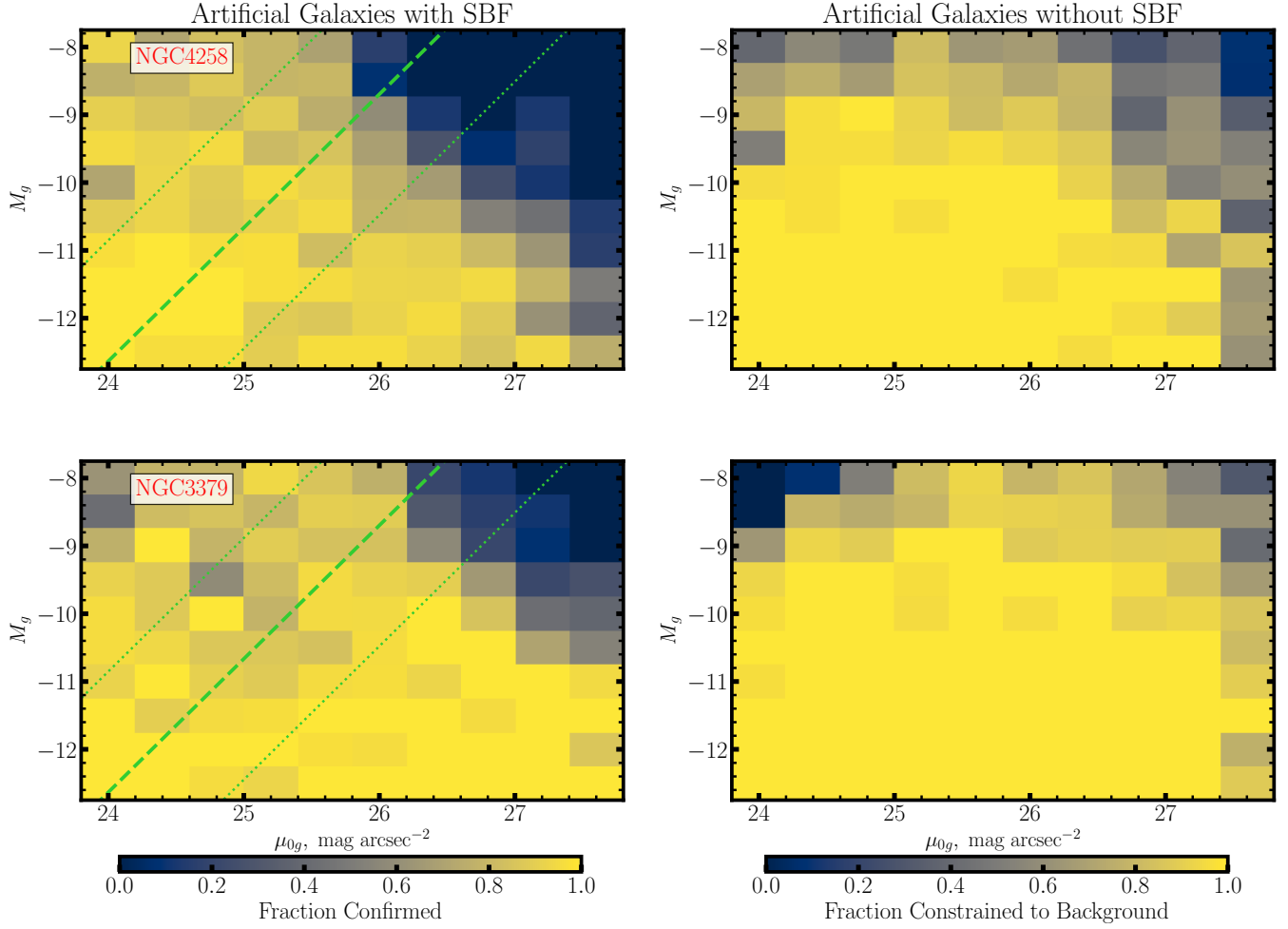


**Figure 15.** Results of performing the SBF measurement on suites of simulated dwarfs around two example hosts (top and bottom). *Right:* Dwarfs are simulated with SBF at the level appropriate to being real satellites of their host. The plot shows the fraction of simulated dwarfs that are successfully confirmed as satellites at different luminosities and surface brightness. The dwarfs that are not confirmed have too low S/N in the SBF measurement and stay as ‘unconfirmed/candidate’ satellites. The green dashed line shows the mass-size relation of [Carlsten et al. \(2021b\)](#). *Left:* Dwarfs are simulated without SBF, as if they are in the distant background. The plot shows the fraction of simulated dwarfs that are successfully rejected as background contaminants due to their lack of SBF. Again, the dwarfs that are not rejected have too low S/N in the SBF measurement and stay as ‘unconfirmed/candidate’ satellites.

Table 9. Satellite Photometry

Name	R.A (deg)	DEC (deg)	Host	$m_g$ (mag)	$m_{r/i}$ (mag)	$M_V$ (mag)	$M_*$	$\mu_{0,V}$ (mag arcsec $^{-2}$ )	$r_e$ (pc)	ETG	Conf.	$P_{\text{sat}}$	Filt.
NGC247	11.7834	-20.7570	NGC253	9.44 ± 0.08	8.96 ± 0.09	-18.60 ± 0.09	9.41 ± 0.13	21.27 ± 0.11	4278.3 ± 199.3	False	True	-	gr
dw0047m2623	11.8939	-26.3898	NGC253	18.89 ± 0.11	18.33 ± 0.11	-9.19 ± 0.11	5.77 ± 0.14	26.59 ± 0.15	453.9 ± 39.8	True	True	-	gr
dw0049m2100	12.4537	-21.0167	NGC253	15.07 ± 0.09	14.89 ± 0.09	-12.79 ± 0.09	6.62 ± 0.13	23.20 ± 0.11	627.1 ± 31.8	False	True	-	gr
dw0050m2444	12.5749	-24.7367	NGC253	18.22 ± 0.10	17.95 ± 0.10	-9.70 ± 0.10	5.53 ± 0.13	27.91 ± 0.13	1539.2 ± 115.0	True	True	-	gr
dw0055m2309	13.7538	-23.1688	NGC253	17.49 ± 0.09	17.14 ± 0.10	-10.47 ± 0.10	5.96 ± 0.13	23.75 ± 0.12	279.1 ± 18.1	False	True	-	gr
dw0036m2828	9.1273	-28.4701	NGC253	18.67 ± 0.11	18.47 ± 0.11	-9.21 ± 0.11	5.23 ± 0.14	24.39 ± 0.14	311.7 ± 25.8	False	False	0.05	gr
dw0132p1422	23.2486	14.3736	NGC628	16.05 ± 0.09	15.85 ± 0.09	-14.02 ± 0.09	7.14 ± 0.13	22.02 ± 0.11	715.4 ± 38.7	False	True	-	gr
dw0133p1543	23.4842	15.7314	NGC628	19.94 ± 0.14	19.38 ± 0.13	-10.34 ± 0.14	6.22 ± 0.15	23.93 ± 0.20	214.4 ± 25.6	True	True	-	gr
dw0134p1544	23.5537	15.7463	NGC628	17.57 ± 0.10	17.07 ± 0.10	-12.68 ± 0.10	7.07 ± 0.13	24.00 ± 0.12	1078.1 ± 65.9	True	True	-	gr
dw0134p1438	23.6741	14.6444	NGC628	17.06 ± 0.09	16.86 ± 0.10	-13.01 ± 0.09	6.74 ± 0.13	21.73 ± 0.12	497.9 ± 30.2	False	True	-	gr
dw0136p1628	24.0842	16.4701	NGC628	17.75 ± 0.10	17.19 ± 0.10	-12.52 ± 0.10	7.10 ± 0.13	22.50 ± 0.13	336.7 ± 22.6	True	True	-	gr
dw0137p1537	24.3236	15.6329	NGC628	17.86 ± 0.10	17.24 ± 0.10	-12.45 ± 0.10	7.17 ± 0.13	22.59 ± 0.13	380.2 ± 26.4	True	True	-	gr
dw0137p1607	24.4156	16.1320	NGC628	20.20 ± 0.14	19.57 ± 0.13	-10.12 ± 0.15	6.24 ± 0.17	25.96 ± 0.21	489.2 ± 64.2	True	True	-	gr
dw0138p1458	24.5024	14.9825	NGC628	16.98 ± 0.09	16.61 ± 0.09	-13.19 ± 0.09	7.07 ± 0.13	22.42 ± 0.12	349.5 ± 21.0	False	True	-	gr
UGC1171	24.9366	15.8993	NGC628	15.71 ± 0.09	15.45 ± 0.09	-14.40 ± 0.09	7.38 ± 0.13	22.36 ± 0.11	840.5 ± 44.3	False	True	-	gr
dw0139p1433	24.9611	14.5563	NGC628	17.89 ± 0.10	17.59 ± 0.10	-12.24 ± 0.10	6.59 ± 0.13	22.25 ± 0.13	258.9 ± 18.1	False	True	-	gr
dw0140p1556	25.0395	15.9394	NGC628	18.64 ± 0.11	18.47 ± 0.11	-11.41 ± 0.11	6.05 ± 0.13	24.03 ± 0.14	449.5 ± 36.9	False	True	-	gr
UGC1176	25.0430	15.9054	NGC628	14.24 ± 0.09	13.86 ± 0.09	-15.93 ± 0.09	8.19 ± 0.13	23.44 ± 0.11	2350.7 ± 115.3	False	True	-	gr
dw0143p1541	25.9012	15.6937	NGC628	15.75 ± 0.09	15.35 ± 0.09	-14.44 ± 0.09	7.63 ± 0.13	24.46 ± 0.11	1437.6 ± 76.0	False	True	-	gr
dw0141p1651	25.4173	16.8721	NGC628	18.14 ± 0.10	17.68 ± 0.10	-12.08 ± 0.10	6.78 ± 0.13	23.06 ± 0.13	473.4 ± 34.7	False	False	0.30	gr
dw0221p4221	35.3010	42.3640	NGC891	17.28 ± 0.09	16.79 ± 0.10	-12.80 ± 0.10	7.10 ± 0.13	22.58 ± 0.12	513.0 ± 31.9	True	True	-	gr

NOTE—The main photometric results for the ELVES Survey. Includes both satellites with conclusive distance confirmation and those without distinguished by the Confirmed column.  $P_{\text{sat}}$  estimates the likelihood of the unconfirmed satellites being real based on the candidates luminosity and surface brightness, see §5.6. Photometry references are the same as given in Table 1. Dwarfs marked with a † had some issue with the photometry and the results might be biased. The full table will be published online or will be provided upon request from the authors.

## G. SATELLITE SYSTEM RESULTS

In Table 9, we present the main optical photometry for the confirmed and possible satellites. Note that only satellites and candidates with  $M_V < -9$  mag are included.

Note that these lists are slightly different than the dwarf lists in the ELVES paper on dwarf structure (Carlsten et al. 2021b) and the ELVES paper on globular clusters and nuclear star clusters (Carlsten et al. 2021a). The former was restricted to small survey coverage radii, a sub-sample of the full ELVES host sample, and only dwarfs in the mass range  $10^{5.5} < M_\star < 10^{8.5} M_\odot$ . The photometry given here is essentially identical to that given there with a few exceptions where different imaging data or slightly different Sérsic fits were used. The photometry is also often slightly different than that given in Carlsten et al. (2021c) for overlapping dwarfs since in that work we were not using an iterative masking process in the Sérsic fitting (see Carlsten et al. 2021b, for an in-depth description of this).

On the other hand, Carlsten et al. (2021a) considered confirmed early-type satellites at all radii (even as far out as 500 kpc projected) and, thus, included some satellites not included in the current catalogs.

Finally, we note that three candidate satellites (dw1305p4206, dw1308p4054, and dw1311p4051) are repeated twice each in the list, once as satellite candidates of NGC 5055 and once as candidates of NGC 4736 (NGC 5055 and NGC 4736 have overlapping projected virial regions on the sky). The distance independent quantities for the copies are essentially the same (even though the Sérsic fits are independent), but the luminosities assume the host’s distance which will be different.

Table 10 presents the GALEX photometry for the confirmed satellites which have archival coverage. In addition to the satellites without archival coverage, this list does not include several of the most massive ( $M_\star > 10^9 M_\odot$ ) satellites for which we did not trust the effective radii from the optical photometry.

**Table 10.** GALEX Photometry for confirmed satellites.

Name	RA	DEC	Host	$m_{\text{NUV}}$	$m_{\text{FUV}}$	GALEX Frame
	(deg)	(deg)		(mag)	(mag)	
dw0047m2623	NGC253	11.8939	-26.3898	> 22.08	> 21.15	MIS2DFSGP_30532.0143
dw0049m2100	NGC253	12.4537	-21.0167	$16.74 \pm 0.05$	$16.97 \pm 0.05$	GI1_009002_UGCA015
dw0055m2309	NGC253	13.7538	-23.1688	$18.93 \pm 0.07$	$19.17 \pm 0.11$	AIS_276_1_59
dw0133p1543	NGC628	23.4842	15.7314	> 22.45	> 22.38	AIS_183_1_66
dw0134p1544	NGC628	23.5537	15.7463	$20.65 \pm 0.16$	> 22.37	GI3_050001_NGC628
dw0136p1628	NGC628	24.0842	16.4701	$21.00 \pm 0.55$	> 21.68	AIS_183_1_65
dw0137p1537	NGC628	24.3236	15.6329	$21.50 \pm 0.17$	> 22.97	NGA_NGC0628
dw0137p1607	NGC628	24.4156	16.1320	> 22.58	> 22.84	NGA_NGC0628
UGC1171	NGC628	24.9366	15.8993	$17.94 \pm 0.05$	$18.39 \pm 0.05$	GI1_047008_UGC01176
dw0139p1433	NGC628	24.9611	14.5563	$19.35 \pm 0.05$	$19.47 \pm 0.05$	MISDR2_17173_0426
dw0140p1556	NGC628	25.0395	15.9394	$20.44 \pm 0.11$	$20.49 \pm 0.11$	GI1_047008_UGC01176
UGC1176	NGC628	25.0430	15.9054	$15.78 \pm 0.05$	$16.07 \pm 0.05$	GI1_047008_UGC01176
dw0143p1541	NGC628	25.9012	15.6937	$17.73 \pm 0.11$	$17.87 \pm 0.13$	AIS_183_1_83
dw0221p4221	NGC891	35.3010	42.3640	$20.71 \pm 0.08$	$22.34 \pm 0.42$	GI2_019004_3C66B
UGC1807	NGC891	35.3058	42.7629	$15.93 \pm 0.05$	$16.17 \pm 0.05$	GI2_019004_3C66B
dw0222p4242	NGC891	35.7298	42.7123	$19.78 \pm 0.09$	> 22.04	GI2_019004_3C66B
dw0239p3926	NGC1023	39.8325	39.4339	> 20.05	> 19.98	AIS_59_1_64
dw0239p3903	NGC1023	39.8432	39.0554	> 21.43	> 21.03	AIS_59_1_64
dw0239p3902	NGC1023	39.9460	39.0473	> 23.24	> 22.78	NGA_NGC1023
UGC2157	NGC1023	40.1044	38.5630	$17.13 \pm 0.05$	$17.72 \pm 0.09$	AIS_59_1_74
dw0240p3854	NGC1023	40.1374	38.9004	$18.82 \pm 0.05$	$19.18 \pm 0.05$	NGA_NGC1023

NOTE—The GALEX photometry for the distance-confirmed satellite that have archival coverage. For dwarfs with a detection with  $S/N < 2$ , a  $2\sigma$  lower limit to the UV magnitude is given. The full version of the table will be published in the online journal or will be provided upon request to the authors.